TECHNISCHE UNIVERSITÄT MÜNCHEN

Lehrstuhl für Humanbiologie

Molecular Carcinogenesis, Development of New Therapeutic Strategies and Multimodal Imaging in Murine Endogenous Pancreatic Cancer

Irina Heid

Vollständiger Abdruck der von der Fakultät Wissenschaftszentrum Weihenstephan für Ernährung, Landnutzung und Umwelt der Technischen Universität München zur Erlangung des akademischen Grades eines

Doktors der Naturwissenschaften

genehmigten Dissertation.

Vorsitzender:	Univ.-Prof. Dr. B. Küster
Prüfer der Dissertation:	1. Univ.-Prof. Dr. M. Schemann
	2. Priv.-Doz. Dr. J. T. Siveke

Die Dissertation wurde am 13.12.2012 bei der Technischen Universität München eingereicht und durch die Fakultät Wissenschaftszentrum Weihenstephan für Ernährung, Landnutzung und Umwelt am 10.04.2013 angenommen.

Summary

Pancreatic cancer and its most frequent form pancreatic ductal adenocarcinoma (PDAC) is a lethal, highly heterogeneous disease lacking effective therapeutic approaches. Thus, intensive research in all fields of pancreatic cancer including molecular pathway analysis of PDAC onset and progression, accurate diagnosis as well as development of new therapeutic regiments is of utmost importance in order to improve pancreatic cancer patient's care. In this work a comprehensive approach is presented that combines basic and preclinical research platforms based on genetically engineered mouse models (GEMM).

First, the role of RAS-related C3 botulinum substrate 1 (Rac1), a downstream target of Ras, was investigated in *Kras*^{G12D}-induced murine pancreatic carcinogenesis and acute pancreatitis. Elevated Rac1 expression was noted in both mouse and human pancreatic tumors, particularly in the stroma. Pancreas specific deletion of Rac1 in *Kras*^{G12D}-driven murine PDAC models led to an impaired formation of preneoplastic lesions due to incorrect actin reorganization. Moreover, *Kras*^{G12D} - bearing animals missing Rac1 in the pancreas revealed impaired tumor development and significantly prolonged survival. In addition, Rac1 was proven to be an important modulator of acinar cell integrity and inflammatory changes accompanying neoplastic process as well as occurring in experimental acute pancreatitis.

Secondly, a comprehensive non-invasive imaging approach using various *Kras*^{G12D} – driven GEMM was applied with the aim to identify markers that allow prediction of tumor type and response to therapy. Five GEMM with different PDAC characteristics were analyzed for tumor heterogeneity and growth kinetics, metabolic status, tissue composition and perfusion using multiparametric magnetic resonance imaging (MRI) and positron emission tomography (PET). Thereby a wide histological spectrum of murine pancreatic cancer was observed including G1-G3 mPDAC with different stroma content, anaplastic and acinus cell carcinomas as well as metastases to the lung and liver in some models. T2-weighted imaging allowed reasonable delineation of the tumor rim and differentiated hypointense mIPMNs and acinus cell carcinomas from hyperintense solid ductal PDACs. Diffusion weighted MRI (DWI) and thereof calculated apparent diffusion coefficients (ADC) revealed good correlation with tissue cellularity and collagen content and could be used as a reliable parameter for differentiation of tissue composition. Dynamic contrast enhanced MRI data revealed a highly heterogeneous inter- and intra-individual perfusion pattern. [^{18}F]-FDG tracer enriched in 100% of mPDACs. [^{18}F]-FDG uptake tumor-to-muscle ratios (T/M) enabled differentiation of preneoplastic lesions and mPDAC, independent of the underlying genotype. Therapy response monitoring was tested in a cohort of subcutaneously transplanted mPDAC, revealing feasibility of tumor volume and [^{18}F]-FDG tracer uptake as reliable read out parameters.

Finally, two commercially available inhibitors of Rac1 activity EHT1864 and NSC23766 were tested *in vitro* on primary pancreatic cancer cells. Combination therapy of Gemcitabine with EHT1864 was found as the most effective anti-cancer treatment *in vitro*. A small pilot *in vivo study* using characterized *CKP*$^{fl/fl}$ model indicates feasibility and possible antitumor efficiency of EHT1864 resulting in moderate necrosis of the tumors identified by DWI.

In conclusion, multiparametric imaging of murine pancreatic cancer using MRI and PET is feasible and useful for characterization of mPDAC models. Tumor response monitoring could be evaluated using anatomical and diffusion weighted MRI as well as PET imaging. Thereby, a chemical inhibition of Rac1 activity may be a new promising therapeutic target for pancreatic cancer.

Zusammenfassung

Pankreaskrebs und dessen häufigste Form, das duktale Adenokarzinom (PDAC), ist eine letale, heterogene Erkrankung für die derzeit keine effektiven therapeutischen Strategien existieren. Deshalb sind intensive Studien in den Bereichen der Aufklärung von PDAC-induzierenden molekularen Signalwegen, der Diagnostik und der Entwicklung neuer therapeutischer Leitlinien für Pankreaskrebspatienten von größter Bedeutung. Diese Arbeit stellt einen neuen Ansatz dar, in dem Grundlagenforschung und präklinische Studien kombiniert werden, um PDAC mit Hilfe genetisch veränderter Mausmodelle (GEMM) umfassend zu untersuchen.

Zunächst wurde die Rolle des RAS-verwandten C3 botulinium Substrates 1 (Rac1) im *Kras*^{G12D}-induzierten murinen (m)PDAC und experimenteller akuter Pankreatitis untersucht. Rac1 ist ein wichtiges Effektormolekül des Kras-Signalweges. Erhöhte Expression von Rac1 wurde sowohl in humanen als auch in murinen Tumoren, jedoch überwiegend im Stroma gefunden. Pankreas-spezifische Deletion von Rac1 in verschiedenen *Kras*^{G12D}-induzierten mPDAC Modellen führte zu einer deutlichen Verminderung der Entstehung transformations-sensitiver metaplastischer Gangstrukturen aufgrund inkorrekter Aktinreorganisation. Außerdem entwickelten Tiere, die onkogenes Kras und deletiertes Rac1 im Pankreas aufweisen, deutlich weniger Karzinome und überlebten länger. Zusätzlich wurde beobachtet, dass Rac1 ein wichtiges Modulatormolekül für die Integrität der Azinuszellen und für die, das mPDAC, beziehungsweise experimentelle akute Pankreatitis begleitende Entzündungsreaktion darstellt.

Desweiteren wurde eine umfassende nicht invasive Untersuchung verschiedener *Kras*^{G12D}-induzierter GEMMs durchgeführt, mit dem Ziel Parameter zu identifizieren, die eine Aussage über Tumor-Typ oder -Veränderungen während einer therapeutischen Behandlung erlauben. Hierzu wurden fünf GEMs bezüglich ihrer Tumorheterogenität, Wachstumskinetik, metabolischen Status, Gewebebeschaffenheit und Perfusion mittels Magnetresonanztomographie (MRT) und Positronemissionstomographie (PET) charakterisiert. Es wurde ein breites histologisches Spektrum des Pankreaskarzinoms in den untersuchten Modellen beobachtet: neben G1 bis G3 diefferenzierten mPDAC mit unterschiedlichem Stromagehalt, entwickelten manche Modelle anaplastische oder Azinuszell-Karzinome, sowie Lungen- und Lebermetastasen. T2-gewichtete MRT Bilder erlaubten eine gute Umrandung der Tumore und ermöglichten eine Unterscheidung zwischen hyperintensen, soliden mPDAC und hypointensen mIPMN. Die Diffusionsbildgebung und der davon berechnete effektive Diffusionskoeffizient (ADC) zeigten eine gute Korrelation mit Zellularität und Kollagengehalt des Gewebes und erlaubte deshalb eine zuverlässige Unterscheidung der verschiedenen histologischen Tumortypen. Dynamische kontrastmittel-verstärkte Perfusionsuntersuchungen mittels MRT (DCE-MRI) zeigten eine starke inter- und intraindividuelle Heterogenität. Eine erhöhte [^{18}F]-FDG Tracer Aufnahme wurde in 100% der mPDAC beobachtet. Durch die Bildung eines Tumor-zu-Muskel Quotienten (T/M) konnten Vorläuferläsionen von den Karzinomen unterschieden werden. Das verfolgen der Therapie-induzierten Änderungen im Tumor wurden in einer Gruppe von Mäusen untersucht denen subkutan mPDAC transplantierten wurde. Dabei konnten Volumen und [^{18}F]-FDG Anreicherung als effektive Monitoring-Parameter bestätigt werden.

Zusätzlich wurden zwei im Handel erhältliche Inhibitoren der Rac1 Aktivität EHT1864 und NSC23766 an primären murinen Zellen des Pankreaskarzinoms *in vitro* getestet. Die Kombination von EHT1864 und Gemcitabine erwies sich als die effektivste anti-tumorale Therapie *in vitro*. Eine kleine Pilotstudie in dem charakterisiertem *CKP*$^{fl/fl}$ Model wies darauf hin, dass EHT1864 gut verträglich und möglicherweise wirksam gegen mPDAC ist. Der

therapeutische Erfolg zeigte sich durch moderate Nekroseentwicklung im Pankreas der behandelten Mäuse, die mittels DWI detektiert wurde.

Zusammenfassend, wurde in dieser Arbeit die multimodale Bildgebung der murinen Pankreaskarzinome mittels MRT und PET etabliert und für die Charakterisierung der GEMM verwendet. Eine mögliche Reaktion des Tumorgewebes auf die Standardtherapie Gemcitabine wurde evaluiert, wobei Tumorvolumen und PET T/M Quotient als mögliche Parameter für Monitoring validiert wurden. Eine chemische Inhibition der Rac1 Aktivität könnte einen neuen aussichtsreichen Therapieansatz darstellen.

Table of contents

1. Introduction

Given the enhanced live expectancy of the population in Europe, North America and Japan, cancer has become one of the major public health problems. Currently, every 4th death in western countries is cancer-related [1-3]. Pancreatic cancer is the most lethal epithelial malignance placed on the 4th position in the estimated deaths statistics of the United States independent of the sex. Moreover, while incidence and mortality rates for most cancers (including lung, colorectal, female breast, and prostate) are decreasing, the prognosis for pancreatic cancer patients remains dismal [3]. Thus, more knowledge about pancreatic cancer biology is urgently needed in order to develop new detection tools and successful treatments for this lethal disease. The aim of this chapter is to give an overview for the state-of-the-art in pancreatic cancer research, established imaging modalities and therapy development.

1.1 Pancreas

1.1.1 Pancreatic anatomy and physiology

The pancreas is a gland organ in the digestive and endocrine system of vertebrates. It is located in the epigastrium and left hypochondrium areas of the abdomen and divided into three main parts: the head, situated within the concavity of the duodenum; the body, which lies behind the stomach and the tail as left end of the pancreas (Fig. 1A).

The exocrine compartment of the pancreas consists of acinar and ductal cells (Fig. 1B, C) accounting for greater than 90% of the organ tissue. The acinar cells are organized in grape-like clusters surrounding termini of the highly branched duct system. Acini produce precursors of digestive enzymes (zymogens) and secrete them into the intralobular ducts, which transport secretes and bicarbonate ions into the duodenum. The main zymogens/enzymes produced in the pancreas are trypsinogen, chymotrypsinogen, lipase and amylase.

The endocrine function of the pancreas is assured by compact structures embedded within acinar parenchyma, so called islands of Langerhans (Fig. 1D). The islands comprise four cell types: insulin-producing β-cells, glucagon-producing α-cells, somatostatin-producing δ-cells and pancreatic polypeptide-producing PP-cells. Fine tuned communication between this compartment and other organs via surrounding blood vessels allows the body to regulate glucose metabolism and therefore energetic balance.

1.1.2 Morphogenesis of the pancreas

In vertebrates, the pancreas originates from the gut endoderm, one of the three germ layers developed after the gastrulation process [4]. In the mouse, the dorsal bud of the gut tube first emerges at embryonic day E9.5 due to the inhibition of the hedgehog signaling by the notochord secreted factors [5] (Fig. 1E,F). Simultaneously, the ventral protrusion appears close to the hepatic and bile duct endoderm. As the stomach and duodenum rotate, the ventral and dorsal buds proliferate, branch and move around until they fuse into an epithelial tubular complex containing all precursor cell lines at day E12.5 [6]. Between the days E13.5 and E17.5 the multipotent pancreatic progenitors differentiate into islets, acinar and ductal lineage compartments of the mature organ under the influence of multiple transcription factors (Fig. 1G). Both ventral and dorsal buds contribute to the development of the pancreas head, whereas the body and the tail of the organ are derived from dorsal bud alone [4] (Fig 1E,F).

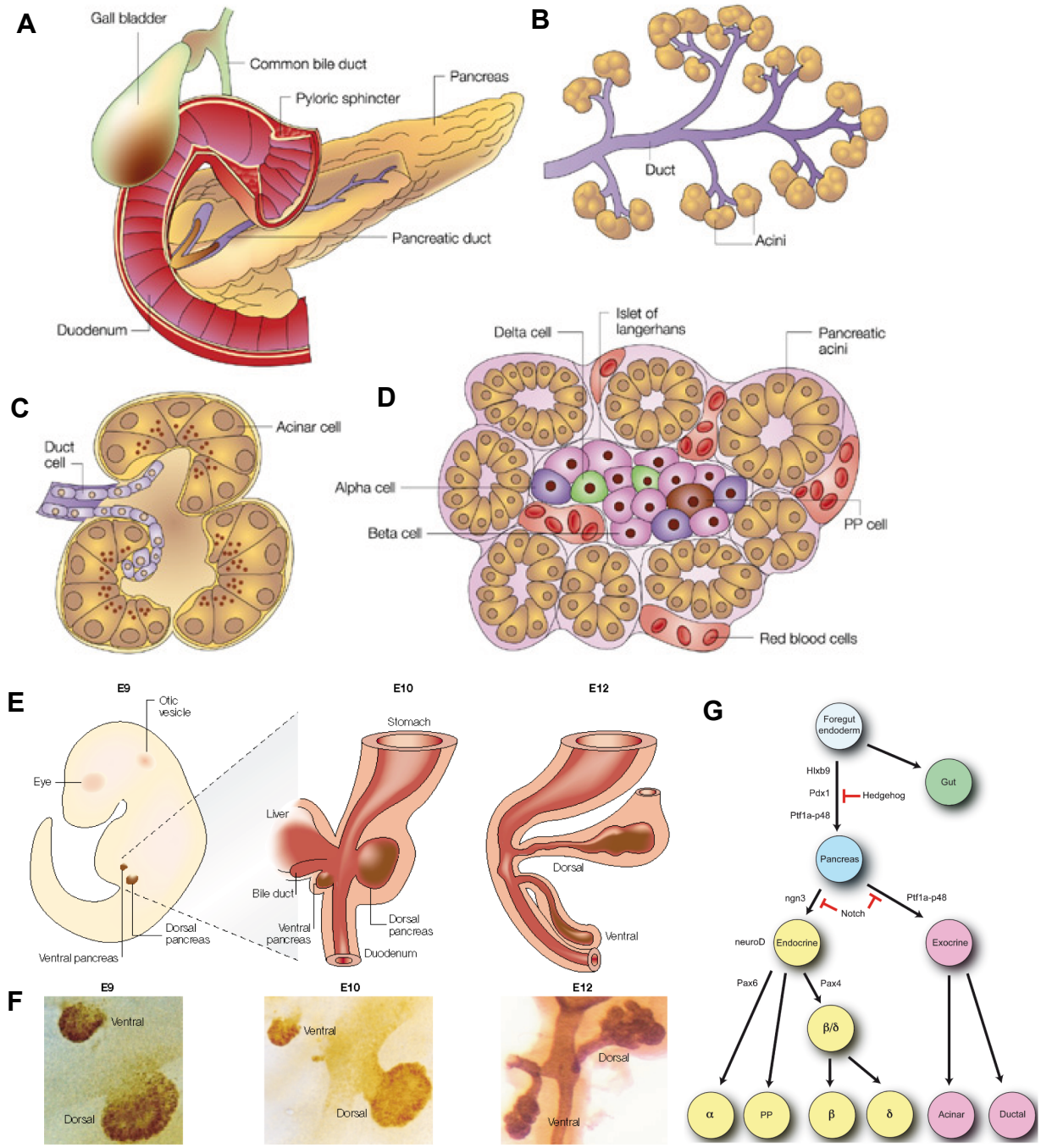

Figure 1: Anatomy, development and pattern of transcriptional activation of the murine pancreas. Anatomical composition of the pancreas: gross anatomy (A), acini and ducts (B, C), island of Langerhans (D) [7]. E-G: Schematic representation (E), Pdx1-staining (F) and relevant genes expression pattern (G) of murine embryonic pancreas at indicated time points [8, 9].

Several transcription factors (TF) that influence pancreatic cell faith and differentiation were identified in the last decade [10] (Fig. 1G). The main two TFs in developing pancreas are pancreatic duodenum homeobox 1 (Pdx1, mouse analog to human Ipf1) and pancreas transcription factor 1 subunit alpha (Ptf1a). Both factors are crucial for pancreas development and expressed in the multipotent pancreatic progenitor cells from very early stage. However, during the fate specification phase endocrine cells loose Pdx1-expression, while endocrine progenitors stop expressing Ptf1a. Thus, in the adult pancreas, Pdx1 is mostly present in β- and δ-cells, whereas Ptf1a-expression is restricted to the exocrine and ductal compartment [6, 10]. This knowledge of the normal pancreas development was used to generate the genetically engineered mouse models (GEMM) for pancreatic cancer as described below.

1.2 Pancreatic cancer

Invasive pancreatic ductal adenocarcimoma (PDAC) is the most frequent and highly lethal type of pancreatic cancer. The overall 5-year survival rate for all stages of this disease is less than 1- 4% and median survival amount only 6 months [1-3]. One of the reasons for dismal prognosis of patients diagnosed with PDAC is the enormous difficulty of the tumor detection in early stages due to indistinct symptoms, trouble to biopsy and absence of early biomarkers for this malignance. Thus, more than 80% of the patients present with locally advanced, metastatic and mostly inoperable disease.

The estimated lifetime risk of developing PDAC is 1%, which rises dramatically after the age of 50 years. The few known factors contributing to the development of the disease are cigarette smoking (relative risk = 2), obesity, long-standing diabetes mellitus and chronic pancreatitis [11]. In addition, patients with family history of PDAC as well as other cancer family syndromes like BRCA2 mutations and multiple mole melanoma have a significantly increased possibility of developing pancreatic cancer. However, despite enormous effort of the research community and the extensive use of GEMM closely recapitulating human pancreatic neoplasia, the precise mechanism of PDAC-development is still unknown. The content of this chapter is a summary of current knowledge about pancreatic cancer progression, pathology and for this project relevant mouse models.

1.2.1 Pancreatic preneoplastic lesions: onset, subtypes, frequent genetic alterations

Pancreatic epithelial neoplasm and their precursors exhibit a wide range of pathologic features [12]. To date, three main forms of precursor lesions are believed to be the initiators for PDAC: pancreatic intraepithelial neoplasia (PanIN), intraductal papillary mucinous neoplasm (IPMN) and mucinous cystic neoplasm (MCN) [13, 14]. PanINs are the most common and more aggressive lesions, albeit IPMNs and MCNs became more important recently, because they are better detectable with improoving radiological methods [12, 15, 16]. Moreover, due to the macroscopic appearance and more distinct symptomatic presentation, patients presented with both IPMN and MCN-derived tumors are often diagnosed earlier and have significantly better survival chances (Table 1).

Over the last decades, a detailed model of m**PanIN** progression to the fully developed PDAC was established and evolved through the elaboration of histological analysis of patient samples and GEMM [7, 9, 14, 17]. PanINs and PanIN-derived carcinomas are known to develop in the pancreas head and heck (Fig. 1A, Table 1). With increasing age, microscopic, asymptomatic hyperplastic lesions of the terminal pancreatic ducts (PanIN-1) undergo morphological changes such as increasing cellular and architectural atypia, mucin production, nuclear abnormalities (PanIN1B and PanIN2) and finally develop to a carcinoma in situ (PanIN3), which culminates in an invasive malignant neoplasia (Fig. 2A). These histological transformations of each PanIN stage are accompanied by distinct genetic and in some cases epigenetic alterations. The earliest events are telomere shortening, aberrant activation of EGF/Her2Neu receptors and point mutation in the Kras proto-oncogene (90-100%) followed by loss of the p16INK4a (90-95%) tumor -suppressor. In addition, further mutations in tumor suppressor genes like TP53 (50-85%) and DPC4/Smad4 (50%) as well as p15 (27-48%) and BRCA2 (7%) are frequently found as later incidents [7, 18]. The results of this process, like deregulation of cell cycle, apoptosis and cellular differentiation together with chromosomal instability and combination of mutations lead to highly malignant pancreatic cancer. However, despite the profound knowledge about mutations occurring during

the PanIN progression, the initiation process as well as the interplay of the different genetic alterations is still not fully understood.

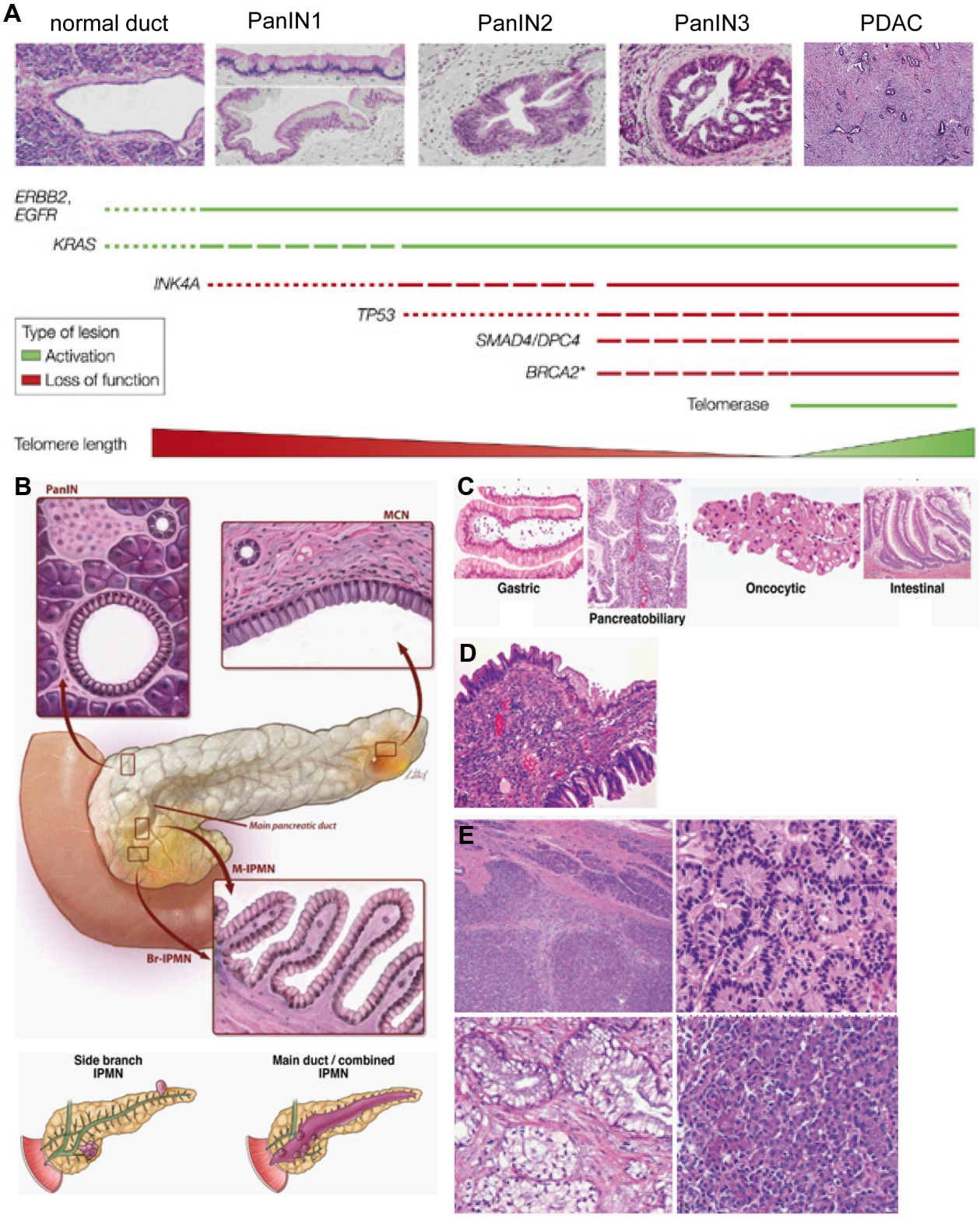

Figure 2: Schematic and histological appearance of main pancreatic preneoplastic lesions and resulting cancers. A: Model of PanIN progression. Top to bottom: Schematic representation of epithelial changes, histological appearance and frequent genetic alteration during PDAC development [7, 12, 18]. B: Location of pancreatic precursor lesions within the human pancreas [13, 15]. C: IPMN classification [15]. D: Example for human MCN [12]. E: Histology of other pancreatic cancer subtypes (top right: poorly differentiated PDAC, top left: endocrine neoplasm, bottom right: glandular PDAC, bottom right: acinar cell carcinoma) [12].

IPMNs are macroscopic mucinous epithelial neoplasms, which arise within the main pancreatic duct or one of its side branches and have often a papillary architecture [12, 19] (Figure 2B, C, Table1). Based on morphology and characteristic mucin expression pattern IPMNs are classified into gastric, intestinal, pancreatobiliary and oncocytic types. Although in variable frequency, most IPMN-lesions (especially of pancreatobiliary type) finally develop into invasive PDAC. Due to the resent discovery of this neoplasm; the mechanisms leading to the IPMN-development are far less understood than those of PanIN progression. It seems, that the pattern of genetic alterations, detected in IPMNs is very similar to the PanIN-associated mutations described above [15]. However, some additional frequent alterations like e.g. in the *PI3KCA* (11%) and *LKB1/STK11* (30%) genes predominantly were detected only in IPMNs and others like in the *SMAD4* gene are absent [20]. The true incidence of IPMN is unknown, but is assumed to be 1/13th of that of PDAC [15] and predominantly occur in man in their 70-ties or 80-ties. The 5-year overall survival for patients with invasive IPMN is ~40%, whereas complete resection of IPMN leads to survival rates up to 90% [13, 15].

MCNs are large mucin-producing epithelial cystic lesions with a variable degree of epithelial dysplasia and focal regions of invasion. The ductal origin of MCNs and their progression to PDAC remains controversial, because MCN appear to be not connected to the ductal system of the pancreas. This type of lesions is characterized by prominent subepithelial ovarian-like stroma expressing progesterone and/or estrogen receptors and affects mostly the pancreas-tail of the middle-aged woman (Fig. 2D; Table 1).

Table 1: Summary of the main PDAC precursor lesions and resembling relevant mouse models.

precursor	size	primary location in pancreas	ratio male/ female	5 years survival after resection	genetically engineered mouse models
PanIN	micro-scopic	head/neck	1.3:1	15-20%	- *Pdx1-Cre;Kras$^{LSL-G12D}$ Ref.[21]* - *Ptf1a^{Cre};Kras$^{LSL-G12D}$ Ref.[21, 22]* - *Ptf1a^{Cre};Kras$^{LSL-G12D}$;Ela-Tgfa Ref.[22]* - *Ptf1a^{Cre};Kras$^{LSL-G12D}$;Notch2$^{lox/lox}$ Ref.[23]* - *Pdx1-Cre;Kras$^{LSL-G12D}$;Notch2$^{lox/lox}$ Ref.[23]* - *Pdx1-Cre;Kras$^{LSL-G12D}$;p53$^{R172H/wt}$ Ref.[24]* - *Pdx1-Cre;Kras$^{LSL-G12D}$;p16/p19$^{lox/lox}$ Ref.[25]* * only GEMMs relevant for this thesis
MCN	macro-scopic	body/tail	1:20	40-60%	- *Ptf1a^{Cre};Kras$^{LSL-G12D}$;Notch2$^{lox/lox}$ Ref.[23]* - *Pdx1-Cre;Kras$^{LSL-G12D}$;Notch2$^{lox/lox}$ Ref. [23]* - *Ptf1a^{Cre};Kras$^{LSL-G12D}$;Smad4$^{lox/lox}$ Ref.[26]*
IPMN - main duct - branch duct	macro-scopic	head head/neck	1,5:1	60-90%	- *Ptf1a^{Cre};Kras$^{LSL-G12D}$;Ela-Tgfa Ref.[22]* - *Pdx1-Cre;Kras$^{LSL-G12D}$;Smad4$^{lox/lox}$ Ref.[27, 28]* - *Ptf1a^{Cre};Kras$^{LSL-G12D}$;Smad4$^{lox/lox}$ Ref.[28]*

* summarized from references [13, 15, 29].

1.2.2 Pathology of pancreatic cancer

Based on the line of cellular differentiation pancreatic cancer can be divided into ductal, exocrine and endocrine malignances. The current classification of the pathology of pancreatic epithelia neoplasms is highly diverse [12]. However, taking into account that some of the entities are very rare conditions and others are very similar in terms of treatment and prognosis, Klimstra and colleagues proposed 2009 eight main subtypes for pancreatic cancer, listed in Table 2. The most common subtypes of pancreatic cancer pathology will be briefly discussed below.

Pancreatic ductal adenocarcinoma (PDAC) is the most common (85%) differentiation type of pancreatic cancer. PDAC is defined by the recapitulation of normal ductal characteristics like gland or tubuli formation, mucin production and expression of cytokeratine 19 (CK19) [12] (Fig. 2A, E). The ductal adenocarcinoma usually forms solid masses containing dense desmoplastic stroma with ubiquitous fibrosis and abundant inflammatory infiltrates (Fig. 2E). Whereas most infiltrating PDAC have a well-differentiated tubular (also called glandular) growth pattern, there are subtypes (2-5%) of these tumors representing other characteristics. Moreover, the undifferentiated PDACs show a higher proliferation rate, reduced non-neoplastic stroma formation and more aggressive behavior. Undifferentiated PDACs include sarcomatoid carcinomas with spindle-like cells, anaplastic (Fig. 2E) carcinomas and carcinosarcomas [12, 18].

Table 2: Classification of Pancreatic Epithelial Neoplasms [12].

Pancreatic Neoplasms	%
Ductal adenocarcinoma	**85**
Serous cystadenoma	**1-2**
Mucinous cystic neoplasm	**1-2**
Intraductal papillary mucinous neoplasm	**3-5**
Acinar cell carcinoma	**1-2**
Pancreatoblastoma	**<1**
Pancreatic endocrine neoplasm	**3-4**
Solid-pseudopapillary neoplasm	**1-2**

Carcinomas derived from acinar cells of the pancreas are usually acinar cell carcinomas (ACC) or pancreatoblastomas [12]. These tumors are usually homogenous, showing highly cellularity with abundant cytoplasm and absence of desmoplastic reaction (Fig. 2E). Both subtypes can be identified by immunohistochemical stainings for pancreatic enzymes like, trypsin (100%), chymotrypsisn (100%) and lipase (60-70%). The differential diagnosis of ACC and pancreatoblastoma should include age (ACC predominantly affects adults, whereas pancreatoblastoma young children) and presence of the squamoid nests characteristic for pancreatoblastoma (Fig. 2E). In opposite to ductal carcinomas Kras gene mutations are usually absent in these cancers [20].

Endocrine cancers are mostly well differentiated, nonagressive neoplasms of the endocrine lineage (Fig. 2E), defined by the production of peptide hormones or bio-amines by the neoplastic cells [12, 18]. Endocrine differentiation can be easily diagnosed by the growth pattern of these solid, circumscribed tumors, with uniform, round cells and nuclei having visible characteristics of salt-and-pepper chromatin structure [12]. A great amount of endocrine cancers show functional activity, giving clinical symptoms of inappropriate production of endocrine hormones [12, 18].

1.2.3 Mouse models of PDAC

The use of animal models is of great importance to experimental researchers. Today, GEMM are widely employed in all fields of pancreatic cancer research: e.g. for rigorous tracing of the “tumor cell of origin” [30-37], for characterization of signaling pathways and spontaneous course of tumor progression [21-28, 38-41] as well as for the development and testing of new therapeutic regiments [42-44]. Moreover, using GEMM it is possible to study malignant development in a biological context with all the complexity of the tumor-host interactions (stromal signals, angiogenesis, inflammation and immunity) [43, 45].

Modern investigators use GEMM based on a *Cre/loxP* technology, where the gene of interest is altered due to the homologous recombination of the loxP sides in the endogenous locus of a

distinct organ (Fig. 3A) [46]. Therefore the endogenous biological expression pattern of the gene is retained. However, the employment of tissue specific promoters in *Cre/lox* system is often combined with unrelated expression of the gene of interest, due to the necessity of the promoter in other organs. For example, cre-mediated gene modification using the two main pancreas specific promoters *Pdx1* and *Ptf1a* results in several side effects. During development, *Pdx1* expression is spread to the distal stomach, common bile duct, the duodenum and the pancreas, leading to cancer onset in all those regions in some models [21, 24]. In contrast, Ptf1a is also expressed in cerebellum, retina and developing mouse spinal cord [47] occasionally leading to hind limbs paralysis in combination with $p53^{R172H/wt}$ mutation (personal observation). In addition, several older transgenic models are also available and still widely used in different research projects (e.g. *Ela-Cre-Tgfa* model) [48, 49].

Today a high variety of GEMM harboring several genetic alterations identified in PDAC were generated and characterized [reviewed in 9, 14, 29]. It is astonishing how closely the conditional endogenous mouse models of pancreatic cancer mimic the human disease. GEMMs based on the introduction of the pancreas-specifically activated proto-oncogen $Kras^{G12D}$ not only recapitulate the full panel of PanIN progression to an invasive PDAC with the human relevant metastatic pattern, but also develop an extensive stromal desmoplasia together with relatively low vascular density [22, 43]. Moreover, progression of preneoplastic lesions, tumor latency and metastatic pattern are differently modulated in these models depending on which pathway is changed in addition to $Kras^{G12D}$. Thus, *Pdx1-Cre;*$Kras^{wt/LSL\text{-}G12D}$ [21] and $Ptf1a^{Cre}$;$Kras^{wt/LSL\text{-}G12D}$ [21, 22] mice develop only PanINs, whereas $Ptf1a^{Cre}$;$Kras^{wt/LSL\text{-}G12D}$;*Ela-Tgfa* [22] animals develop IPMNs and *Pdx1-Cre/* $Ptf1a^{Cre}$;$Kras^{wt/LSL\text{-}G12D}$;$Notch2^{lox/lox}$ [23] MCNs in addition to PanINs (Table 1, Fig. 3B-D).

The cancers developed in $Kras^{G12D}$-induced mouse models cover a wide spectrum of tumor biology ranging from acinar cell carcinoma through undifferentiated sarcomatoid carcinoma (e.g. inactivation of *p16Ink4a* [25] or *Notch2* [23]) to well differentiated PDAC developed in animals leaking the *Tp53* gene in the pancreas [50]. Furthermore, murine pancreatic tumors show similar genetic aberrations crucial for the development of human pancreatic cancer, like loss of p16INK4a and TP53 tumor suppressors [21-24].

1.2.4 How pancreatic preneoplastic lesions form? The questions of the "cell of origin", acinar plasticity and inflammation.

Despite intensive research using specific lineage tracing of distinct pancreatic cells, the exact mechanism of how and where pancreatic cancer begins remains unresolved. It is a common believe, which is supported by many data, that activation of the proto-oncogene Kras is one of the first and necessary events for lesion formation. However, there are still unanswered questions like: Which cell exactly contributes to the preneoplatic and neoplastic process? Is the time-point of Kras-activation crucial? What other factors are involved? This chapter presents a summary of the main current hypotheses extensively analyzed in Kras-driven models and patient samples of pancreatic cancer.

Several recent lineage tracing studies suggest that premalignant PanIN lesions may arise from differentiated acinar cells and /or centroacinar cells in part through a reprogramming mechanism named acino-ductal metaplasia (ADM) [33-38, 51, 52]. Along this process acinar cells react to various stimuli thereby reducing expression of exocrine markers and developing into tubular structures with ductal properties. Thus, centroacinar and/or mature acinar cell may harbor unique properties, leading to pancreatic precursor lesion formation.

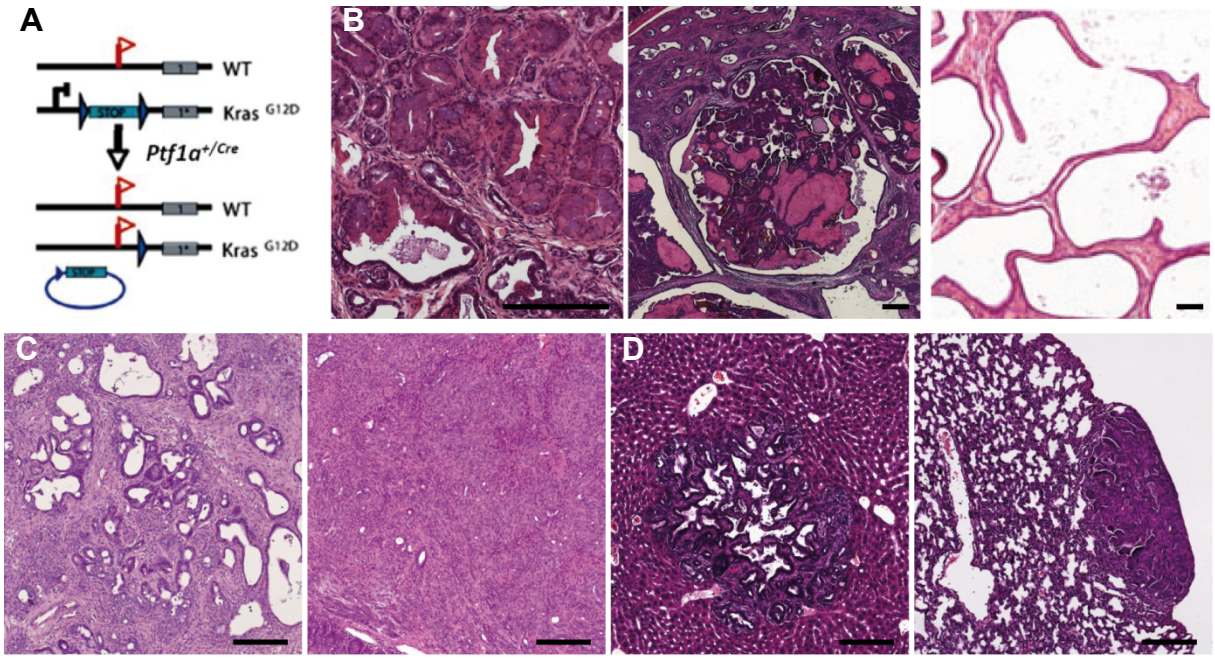

Figure 3: Schema of cre/loxP mediated recombination and histological appearance of main murine pancreatic lesions and PDAC. A: Schematic representation of *Cre/loxP* target gene recombination. B: Examples of murine pancreatic precursor lesions developed in *Ptf1a-Cre;LSL-Kras^{G12D};El-Tgfa* [22] *and Ptf1a-Cre;LSL-Kras^{G12D};Notch2$^{lox/lox}$* [23] models (right mPanINs, middle mIPMN, left mMCN). C: Examples of murine well differentiated (left) and poorly differentiated (right) PDAC. D: Murine PDAC derived liver (left) and lung (right) metastasis. Scale bare = 50 µm.

Another reason for precursor occurrence may be strong variances in the cellular plasticity present in a distinct precursor cell at a certain developmental stage necessary for lesion formation. Thus, expression of a constitutively active Kras oncogene in any particular type of adult pancreatic cells (acinar, ductal or endocrine) in the mouse shows, that neither of them alone led to an invasive carcinoma even in the context of tumor suppressor gene mutation [31, 32, 53]. However, activation of Kras oncogene during embryonic development led to carcinomas derived from embryonic pancreatic precursors and acinar cells [21-26, 28, 32, 48, 50, 54].

Moreover, there is a hypothesis that distinct progenitor cells within the pancreatic compartments exhibit intrinsic differences affecting PDAC development. The particular site of the lesions may reflect diversity in the embryonic development in a pancreatic region. Indeed, aggressive infiltrating carcinomas derived from PanINs and IPMNs arise predominantly in the head of the pancreas, whereas less malignant MCNs are mostly located in the body and the tail of the organ [12]. During development both ventral and a portion of the dorsal pancreatic buds contribute to formation of the head of the organ, while the body and the tail of pancreas derive from the dorsal bud [4]. This hypothesis is underlined through several mouse models developed to study PDAC: Although the gene of interest is usually altered in the whole pancreas during embryonic development, some models recapitulate exactly the pattern of preneoplastic lesions formation seen in patients, as discussed in chapter 1.2.1.

In addition the development of preneoplastic lesions and PDAC is strongly influenced by the interplay between the “cell of origin” itself and the particular microenvironment surrounding it. Thus, chronic and acute pancreatitis are well known risk factors contributing to PDAC-genesis and progression in human as well as in murine studies[30, 31, 55-57]. Several scientific reports reveal that PanIN initiation and development is associated with prominent leucocytic infiltration and may require stimuli secreted by inflammatory infiltration for progression to invasive PDAC [30, 31, 40, 45]. Furthermore, Erez N. and colleagues identified recently a pro-inflammatory gene signature

responsible for tumor-promoting behavior of cancer associated activated fibroblasts (CAFs) isolated from pancreatic, skin, breast and cervical cancers [58]. The expression of signature genes was noted already at the very early stage of hyperplasia in murine squamous cell carcinoma model and was proven to be the cause of tumor infiltrating macrophages.

In summary, understanding cancer development becomes a very multifaceted issue and cannot be answered completely using only patients' samples and human cell lines. The development and the employment of complex genetically-engineered mouse models is becoming more and more important fort the elucidation of open questions as described below.

1.3 The role of Rac1 in cancer development.

Despite enormous effort, new techniques and several newly developed mouse models, the question of how exactly Kras leads to precursor lesions and eventually to PDAC remains unanswered. Moreover, given the fact that there is no PanIN formation in the mouse models lacking the aberrant Kras activation, understanding of effector pathways downstream of oncogenic Ras may be the key answer to therapy development for pancreatic cancer. One promising candidate for this investigation is RAS-related C3 botulinum substrate 1 (Rac1) presented in this chapter.

1.3.1 The Rac1 GTPase.

The RAS-related C3 botulinum substrate 1 (Rac1) is a 21 kDa protein encoded by the *RAC1* gene and belongs to the Rho family of small guanosine triphosphatases (GTPases) [59]. Rho family proteins act as molecular switches between an active (Rac1-GTP) and inactive (Rac1-GDP) state [60]. Thereby, the guanine nucleotide exchange factors (GEFs) facilitate the conformational change of Rac to the GTP-bound active form while GTPase-activating proteins (GAPs) enhance the intrinsic GTPase activity of Rac leading to GTP hydrolysis and Rac inactivation (Rac1-GDP) (Fig. 4A). In addition, guanine nucleotide dissociation inhibitors (GDIs) obstruct the GDP-dissociation from Rac1-GDP looking the protein in the inactive state as well as inhibiting its reassociation with the cell membrane (Fig. 4A). There are three Rac proteins, which are highly homologous but differ in their expression pattern: Rac1 is ubiquitously expressed in both embryonic and adult tissue, Rac2 is specific for hematopoietic cells and Rac3 is highly active in the brain as well as present at low level in other tissues [61]. Receiving extracellular signals from G-coupled protein receptors (GPCR), growth factor receptors, cytokine receptors or integrins, Rac1 transduces them to the intracellular targets (Fig. 4) activating thereby multiple signaling pathways described below.

1.3.2 The role of Rac1 GTPase in secretion, cellular motility and cancer.

The best described function of Rac1 is the engagement in actin cytoskeleton rearrangements and cellular motility [62]. Specifically, activated Rac1 translocates to the cell membrane, causes the uncapping of the fast growing end of actin filaments and induces rapid actin polymerization. Thereby the membrane-associated actin cytoskeleton changes and induces broad sheet-like plasma membrane protrusions that are known as lamellipodia and found at the front of migrating cells [61]. In addition, both Rac1 and Rac2 are crucial for coordination of adhesion, migration, cytoskeleton rearrangements and survival of hematopoietic cells [63, 64]. Moreover, Rac1 is also involved in membrane ruffle formation, vesicle trafficking [65] and in cell secretion [66].

In the pancreas, the digestive enzyme secretion, performed by acinar cells is Rac1 dependent and was intensively investigated. Thus, studies on pancreatic acinar cell explants show increased

localization of Rac1 on the apical pole of the cell and strongly punctuate Rac1 staining in the zymogene concentrated area in response to Cholecytokinin (CCK) in a model of chemically induced pancreatitis. An inhibition of Rac1 by dominant negative mutant RacN17 in this setting blocked acinar morphological changes and F-actin redistribution as well as partially reduced CCK induced amylase release [67]. Another study reports that Rac1 is crucial for pancreatic island morphogenesis, specifically their normal shape formation and migration from the ductal epithelium *in vivo* [68]. Thereby, blocking Rac1 increased E-cadherin mediated cell-cell adhesion and inhibited actin remodeling in response to EGFR ligand betacellulin stimulation.

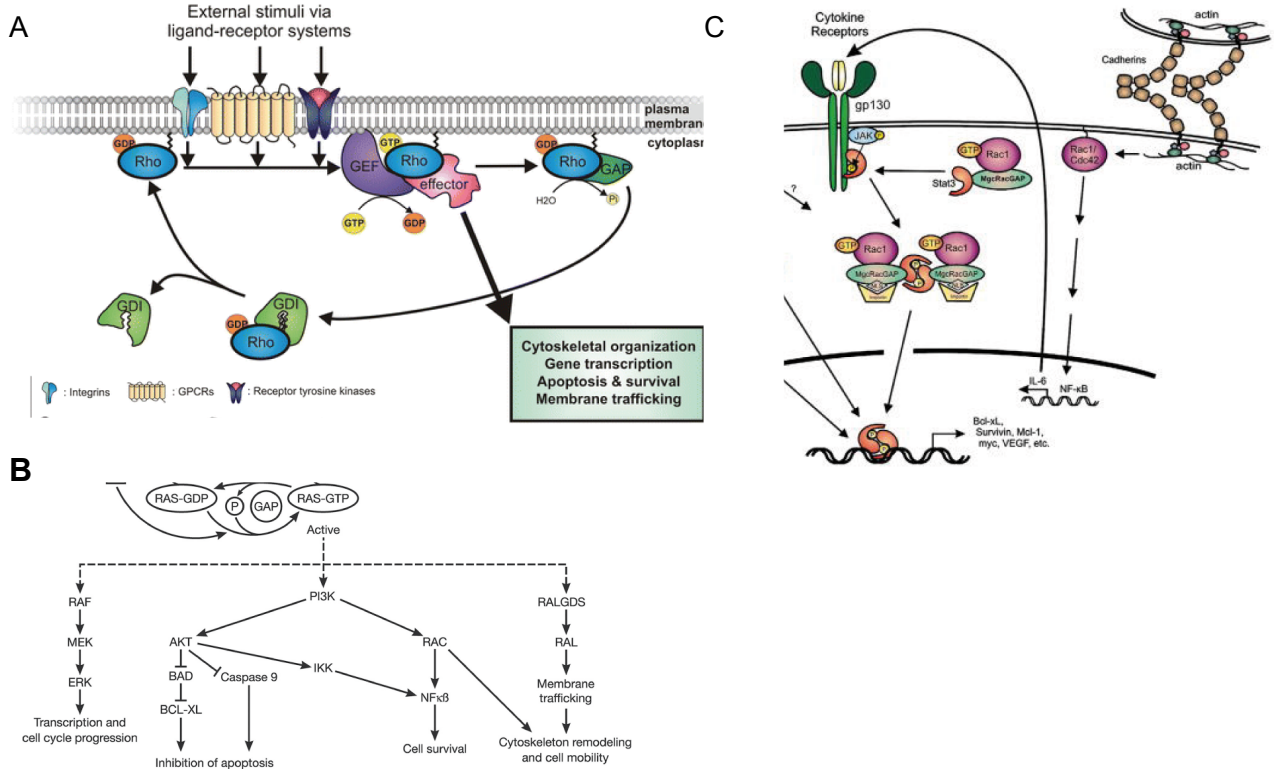

Figure 4: Rac1 GTPase, protein and implicated pathways. A: Schematic representation of Rho-GTPase activation and inhibition [69]. B: The major Ras- and Rac-effector pathways [70]. C: Implementation of Rac1 in E-cadherin, STAT-3 and Nf-kB signaling [71].

Deregulation of Rac1 expression and signaling in human cancers is well established. An overexpression of Rac1 was detected in human patient samples of breast, gastric, testicular, oral squamous cell, upper urinary tract, lung and pancreatic cancer (70%) [69, 72-75]. Also, several studies of altered Rac1 expression in genetically engineered and transplanted mouse models underline importance of this protein for cancer development and maintenance. Thus, the crucial role of Rac1 in the tumor initiation process was proven in an orthotropic mouse model of colorectal carcinoma, where an overexpression of Rac1 promoted and an ablation of Rac1 decreased the tumor progression [76]. Furthermore, the expression of a constitutively active Rac1 isoform in a mouse model of Kamposi's sarcoma (KS) was sufficient to induce KS-like tumors through a mechanism involving reactive oxygen species and hypoxia [77]. Additionally, removal of the Rac1 regulator Tiam1 led to a reduced tumor development in Hras and DMBA induced mouse model of skin cancer [78]. Another study confirmed this finding, since mice bearing kratinocyte-restricted deletion of Rac1 failed to develop chemically induced skin tumors [79]. Moreover, in a $Kras^{G12D}$-driven mouse model of lung cancer deletion of Rac1 completely abrogated tumor development [80]. Recent findings also show that Rac1 plays a crucial role in development of resistances to chemotherapy in breast cancer [81].

It is well established that the migratory ability of a cancer cell directly correlates with the development of metastases. Rac1 is known to support invasive phenotype and metastases development in several cancers. Thus, increased Rac1 activity was detected in breast cancer tissue and metastatic lymph nodes [82]. Another study showed that cell migration of the mammary epithelial tumor cell line MTLn3 was inhibited by dominant negative N17-Rac1 *in vitro* and *in vivo*. Moreover, the authors observed inhibition of intravasation into peripheral blood and abrogation of lung metastases development in a xenograft mouse model [83]. More importantly, a large study of Japanese patients with upper urinary tract cancers revealed increased Rac1 activity and strong Pak1 upregulation, the main known Rac1 effector protein, in primary tumors and lymph node metastases [74]. The changed Rac1 and Pak1 activation pattern was strongly associated with poor differentiation of the main tumors, muscle invasion and shorter disease free survival time of the patients. Taken together, understanding the role of Rac1 in $Kras^{G12D}$-mediated pancreatic carcinogenesis may give important insides of the malignant development and metastatic spread.

1.3.3 Rac1 and cancer related signaling pathways

However the mechanisms of Rac1 involvement in cancer development and progression are still under intensive investigation. Several studies on human cancer cell lines revealed that Rac1 is implicated control of cell cycle, tumor growth, survival [84, 85] and Ras-induced transformation [86, 87]. The most explored signaling pathways involved in cancer and related to Rac1 activation are driven by Epidermal Growth Factor Receptor (EGFR) activation. Oncogenic Kras is a very important transducer of EGFR signaling, leading to activation of Phosphoinositide 3-kinase (PI3K) and Raf/Map Kinase (Raf/MEKK/Erk) cascade and other effectors (Fig. 4B) suggested to be crucial for survival and proliferation in tumor cells. For a long time, PI3K was thought to be the major modulator of Rac activity (reviewed in [88]). Another important inducer of Rac/Pak1 signaling implicated in carcinogenesis is Ras-mediated GEF Tiam1, which can also operate PI3K-independently [89]. In addition, both pathways converge to the MEK/ERK signaling pathway necessary for Rac driven cancer induction [79, 90]. Taken together, Rac1 is involved in at least two major Ras-effector pathways implicated into pancreatic carcinogenesis, making this molecule a good target for selective inhibition of Ras signaling.

Moreover, resent data underline the importance of Rac1 in cancer associated processes such as apoptosis and inflammatory reaction and their main regulators such as Nuclear factor-kappaB (Nf-kB) and interleukin-6 (IL-6) (Fig 4C) [71]. Thus, activation of an active splice variant Rac1b in colorectal cancer cells stimulates NF-κB-mediated G1/S progression, cyclin D1 expression, cell survival and anti-apoptotic reaction [91, 92]. In addition, Fernandez-Zapico and colleagues linked expression of GEF VAV-1 in human pancreatic cancer cell lines to increased survival via Nf-kB activation and Cyclin D1 expression directed through Rac1 activation [93]. Moreover, persistent Rac1 activity leads to overproduction of IL-6 causing activation of Transducer and Activator of Transcription-3 (STAT3) signaling and connecting STAT3 and NF-kB pathways [94]. Both IL-6 expression and STAT3 activation were recently proven to be crucial for mPanIN and mPDAC development in murine models of $Kras^{G12D}$-mediated pancreatic carcinogenesis [95, 96]. Thus, these results implicate that there might be an important link between Nf-kB, STAT3 and Rac1 activation as well as IL-6 secretion in PDAC development, especially because elevated serum levels of IL-6 were found in patients suffering from pancreatic cancer [94, 97].

Loss or deregulation of E-cadherin mediated cell adhesion leads to epithelial to mesenchymal transition (EMT), a starting process for metastatic spread [98]. In addition, invasive tumor cells have to alter the extracellular matrix through matrix metalloproteases (MMPs) and acquire migratory capacities in order to cross tissue boundaries and migrate towards distal parts of the body.

Several publications suggest strong involvement of Rac1 mediated signaling in these processes. For example, *in vitro* finding revealed that enhanced cell-cell contacts and E-cadherin engagement with or without cell contact increases Rac1 activity and triggers STAT3 phosphorylation and IL-6 secretion thereby influencing cell motility through gp130/STAT3 axis [99, 100] (Fig. 4C). Moreover Teng and co-workers report that STAT3 can directly modulate Rac1 activity to regulate actin cytoskeleton reorganization and directional migration [101]. In addition, overexpression of Rac1b mutant in mouse fibroblasts lead to loss of anchorage dependent growth [102] suggesting Rac1 involvement in epithelial to mesenchymal transition (EMT) and may be explaining the Rac1 association with metastatic spread as described above. Furthermore, the EGF-mediated invasive phenotype of the pancreatic tumor cell line PANC-1 was shown to develop through lamellipodia formation and matrix metalloproteinase-2 (MMP-2) secretion mediated by Rac1 [103].

In summary, understanding Rac1 pathways involved in in $Kras^{G12D}$-mediated pancreatic cancer initiation and progression may provide further biological as well as diagnostic and therapeutic clues in pancreatic cancer.

1.3.4 Chemical inhibition of Rac1 activity *in vitro* and *in vivo*

In recent years two chemical inhibitors of Rac1 activity were successfully developed and used in several studies.

The **NSC23766** small molecule specifically targets Rac1 GEF-recognition groove thereby inhibiting Rac1 activation by Tiam1 and TrioN without affecting the activation of closely related small GTPases like Cdc42 or RhoA [104]. In the prostate cancer cell line PC-3 NSC23766 was shown to inhibit normal and anchorage independent cell growth [104]. Inhibition of breast cancer lines with NSC23766 led to cell cycle arrest in retinoblastoma (Rb) expressing cells and apoptosis in cells leaking Rb [105]. Dokmanovic *at al.* showed that NSC23766 restored trastuzumab-induced down-regulation of ErbB2 and cell growth inhibition in the trastuzumab-resistant breast cancer cell line SKBR3 [81]. Furthermore, in the pancreatic cancer cell line PANC-1 NSC23766 blocks EGF-triggered Rac1 activation and impairs MMP-2 secretion as well as ROS production [103]. In addition, NSC23766 was proven to be effective on Rac1 inhibition in pancreatic acinar explants and acute pancreatitis *in vivo*, thereby reducing the severity of pancreatic and lung injury in a cerulein induced model of acute pancreatitis [106]. Moreover, this inhibitor was proposed twice as a potent therapeutic anticancer agent in transplanted mouse models of BCR-ABL-induced chronic myelogenous leukemia (CML) and acute myeloid leukemia (AML), where it inhibited Rac1 activation and engrafting of CML-transplants as well as significantly prolonged the survival of stably transplanted NOD/SCID mice [107, 108]. Interestingly, another study reports that NSC23766 inhibited maintenance and expansion of both normal as well as leukemic stem/progenitor cells by mediating their interaction with stromal cells [109].

The second small molecule Rac1 inhibitor **EHT1864** was developed more recently and until now only applied in *in vitro* studies. This agent interferes directly with the Rac1 nucleotid exchange process, specifically by releasing of Rac1-bound nucleotide into the cell plasma [110]. Therefore EHT1864 should be effective in Rac1 activity inhibition independently of initiative Rac1GEF. Moreover, this inhibitor and not NSC23766, has already been proven to block cell transformation induced by constitutively active $Rac1^{61L}$ mutant [110]. Finally, most studies report a 10 times lover IC50 for inhibition of cell migration and/or cell growth by EHT1864 compared with NSC23766 [110-112].

Taken together, there is strong evidence that inhibition of Rac1 by either of two agents alone or

in combination with standard anti-cancer drugs may represent a new effective therapeutic application for PDAC treatment.

1.4 PDAC diagnosis, monitoring and therapy

Summarizing all risk factors, the lifetime expectancy of developing PDAC is 1%. In addition, more than 80% of the patients present with irresectable disease, which is considered being incurable and is treated with palliative regiments. However, reasonable survival rates can be achieved in the patient group (10%), whose cancers was detected early and treated with resection and adjuvant therapy [113]. Thus, two major goals were addressed by several research groups at the moment: The establishment of robust diagnostic tools for early detection of PDAC (1) and the development of new aggressive therapies for treatment of late stage irresectable pancreatic cancer (2). This chapter summarizes the main diagnostic modalities available for PDAC identification as well as latest advances in clinical and preclinical therapy development studies.

1.4.1 Multimodal imaging and pancreatic cancer

There are several modalities available for the diagnosis of a patient with symptoms suggesting pancreatic cancer: Ultrasound (US) and Endoscopic Ultrasound (EUS), Endoscopic Retrograde Cholangio-Pancreatography (ERCP), multidetector computed Tomography (CT), Magnetic resonance Imaging (MRI), Magnetic Resonance Cholangio-Pancreatography (MRCP) and Postiton Emission Tomography (PET). Among them, multidetector CT and MRI/MRCP are the most sensitive methods [114]. Moreover, CT, EUS and MRI are the best established and in clinical routine mostly used combined methods for diagnosis of PDAC.

Computed Tomography (CT) is the clinically most widely used and relevant technique in pancreatic imaging (Fig. 5A). It is especially widely used in preoperative imaging to obtain high spatial resolution images of local tumor spread and evaluate the resectability of the tumor. The modality allows thin collimation and multiphase detection including scanning at different axis necessary for evaluation of surrounding vessels [115]. Moreover multi-detector CT-combined biopsy and PET/CT (described below) represent the best staging tools along with EUS [116].

Magnetic Resonance Imaging (MRI) is a very attractive technique due to the high spatial resolution and very good anatomically detailed pictures (Fig. 5C-D). In addition MRI is relatively economically priced, widely available and has no need for radioactive contrast agents. Most commonly used 1,5T and 3T MRI-scanners generate T_1- or T_2-weighted (T_2w) images and allow noninvasive evaluation of the common bile and pancreatic ducts, pancreatic parenchyma, adjacent soft tissues, and vascular network. Therefore it is often used additionally to the CT or EUS in difficult cases with small, organ deforming PDAC, islet cell tumors or autoimmune pancreatitis [117, 118].

Besides the anatomical information two further noninvasive MRI-based techniques were established in order to obtain more functional information of the pancreatic tumor and metastases. **Dynamic Contrast Enhanced MRI** (DCE-MRI), a high-resolution, axial or coronal gadolinium-enhanced - T_1 sequences combined with dynamic phase MR angiography allow the best assessment of possible vascular involvement [117]. In addition, **Diffusion-Weighted-Imaging** (DW-MRI) can be helpful as a complementary imaging method in assessment of lesion tissue composition (Fig. 5D, E). The **apparent diffusion coefficient** (ADC) values derived from DWI can help to distinguish between simple pancreatic cysts, inflammatory cysts, and cystic neoplasms of the pancreas, as well as between mass-forming focal pancreatitis and pancreatic adenocarcinoma [119].

Endoscopic Ultrasound (EUS) is the most sensitive technique for the detection of especially small pancreatic lesions. Moreover it allows morphologic imaging and simultaneous biopsy of analyzed region through fine needle aspiration (FNA). However EUS has limited ability to characterize pancreatic masses and is an invasive method, which needs to be performed by an experienced investigator. Therefore new EUS systems like contrast-enhanced power Doppler US and contrast-enhanced harmonic EUS were developed to observe microcirculation and parenchymal perfusion as well as better discriminate pancreatic carcinomas from other neoplasms [120].

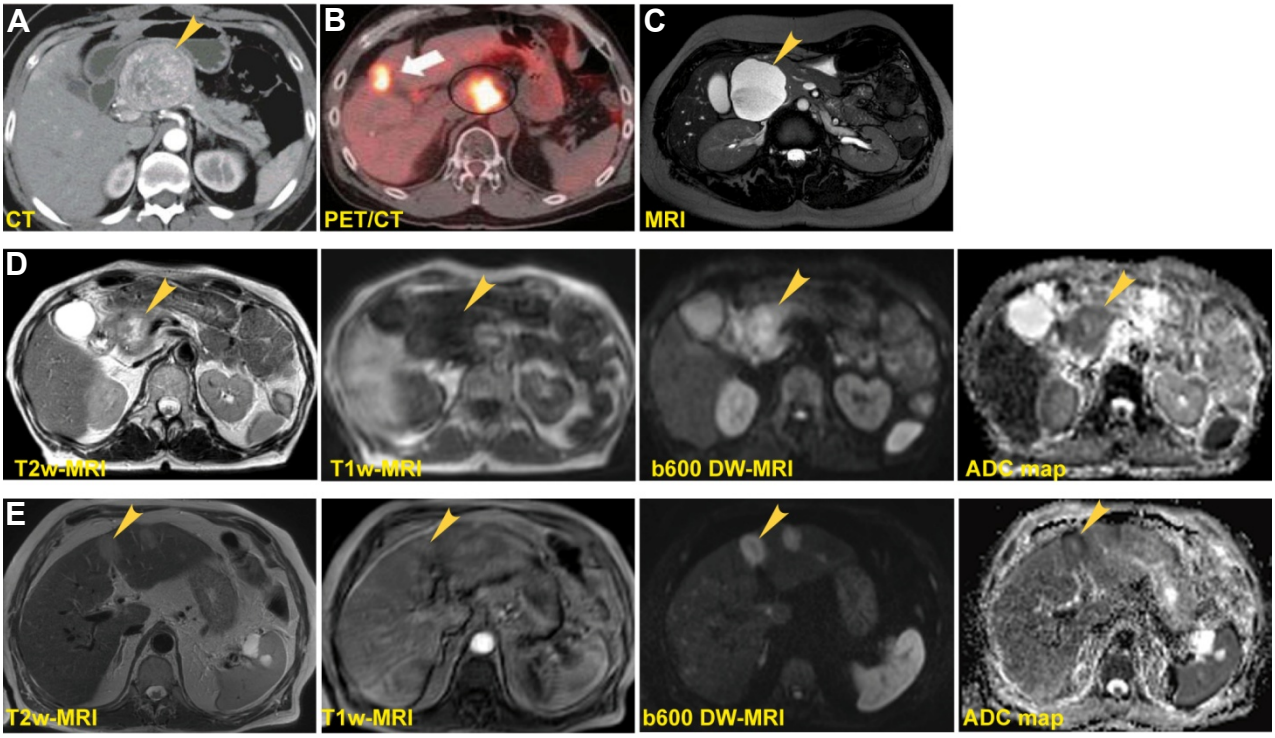

Figure 5: Multimodal imaging examples of human PDAC. A: Pancreatic adenocarcinoma in the pancreas head (arrow head) on a CT [12]. B: Fused axial ^{18}F-FDG PET/CT image showing hypermetabolic lesion of the pancreas head (circle) and liver metastasis (arrow) [121]. C: MRI image of a malignant IPMN in the head of the pancreas [122]. D, E: Example of multimodal MRI-based imaging of PDAC in the pancreas head (D) and liver metastases (E). The lesion edge is clearly more distinguishable on the b600 and ADC map images.

Positron Emission Tomography (PET) is a functional imaging technique using 2-[^{18}F]-fluoro-2-deoxy-D-glucose (FDG) for metabolic assessment of the neoplasm and [^{18}F]-fluoro-3'-deoxy-3'-L-fluorothymidine (FLT) as a PET proliferation tracer [123-125]. Especially, [^{18}F]-FDG-PET complements diagnosis of PDAC and many other cancers. When combined with CT, [^{18}F]-FDG-PET increases the sensitivity, specificity, and accuracy for detecting a pancreatic malignancy and metastases [121, 124] (Fig. 5B). More importantly, this method can detect especially lesions, which CT alone failed to identify or which biopsy results are indeterminate. In addition, [^{18}F]-FDG-PET is often used for determination of tumor response to therapy in postoperative settings [124]. However, recently published report suggests that [^{18}F]-FDG-PET may only have a negative predictive value of 75% for pancreatic cancer [126].

Taken together, multiple imaging modalities are now available for pancreatic cancer diagnostic and therapy monitoring. As decided at the multidisciplinary panel of experts from different European institutions and collaborative groups involved in pancreatic cancer in August 2011 a special emphasis should be made on the standardized use of functional imaging such as PET/CT

and DCE-MRI for use in clinical trials and diagnostic centers [127].

1.4.2 Current treatment options and new developments for pancreatic cancer

Surgical resection is still the only potentially curative treatment of pancreatic cancer. However, this radical operation can only be performed in approximately 20% of newly diagnosed patients [128, 129]. Since local and distant failure rates are high even after complete resection standard adjuvant treatment is Gemcitabine monotherapy for 6 months. This treatment plan was set after the Charité Oncology trail, where Gemcitabine treatment demonstrated a recurrence-free survival benefit of 14 months and survival rate of 20% at 5 years compared to the placebo treated patients [130]. In addition, studies with adjuvant chemoradiation or chemotherapy followed by chemoradiation as well as neoadjuvant treatments showed promising results in numerous recent trials and new regiments can be suggested for selected subgroups of patients [131].

For **palliative treatment** of patients with unresectable metastatic PDAC Gemcitabine was the standard of care therapy for 15 years [132]. 1997 it was shown to induce clinical benefit compared to weekly bolus of 5-Fluorouracil resulting in a response rate of 12-27% of patients with median survival rate of 4-6 months [133, 134]. Despite great efforts and numerous recently found anti-cancer drugs, only one combination of Gemcitabine with a tyrosin-kinase inhibitor Erlotinib led 2005 to a significant increased median survival of only 2 weeks compared to Gemcitabine alone [135, 136]. Interestingly, a subpopulation of patients developing a skin rash while Erlotinib treatment had a significant survival advantage as reported in two large Phase III studies. In addition, enormous efforts and a large scale of preclinical and clinical studies were made, to test Gemcitabine and other known agents alone or in different combinations with new developed anti-cancer agents with no significant benefit [128, 131, 132]. However, for patients with good performance status, a new aggressive regiment named FOLFIRINOX (combination of oxaliplatin, irinotecan, leucovorin, and fluorouracil) was developed recently [137]. The treatment is associated with more toxicities and can be only given to a patient with performance status score 0 of 1, where it significantly increased median survival from 6.8 to 11.1 month compared with Gemcitabine.

1.4.3 GEM models in preclinical diagnosis and therapy monitoring

Despite great quantity of new very effective anti-cancer agents *in vitro*, most of these drugs fail to reduce the tumor burden in preclinical studies. Moreover, agents that successfully passed animal trials often do not demonstrate clinically relevant benefit in follow up clinical studies. Thus, there is an urgent need to improve preclinical testing using appropriate *in vivo* models with high predictive value.

Previously, most preclinical drug testing was performed using transplanted human cancer cell xenografts into immunodeficient animals. However, xenograft models do not recapitulate some of the most important aspects of human PDAC. For one, tumor cell lines do not properly reflect the intratumoral genetic heterogeneity, a hallmark of PDAC. Moreover, neither in cell culture conditions nor subcutaneously or orthotopically transplanted cell lines take into account the crosstalk of tumor cells with the abundant stromal compartment, always present in pancreatic cancer. In addition, highly important biological systems like inflammatory response at the tumor side and the vascular network of the tumor differ in these models compared to human situation. Thus, other preclinical models better mimicking PDAC are urgently needed to validate putative drug targets *in vivo*.

In order to overcome these pitfalls the group of M. Hidalgo developed a model of transplanted personalized tumorgrafts of patients's tumors in immunocompromised mice [138-140]. In this

preclinical method, a resected tumor of a particular patient was propagated in several passages in the mice, while searching for efficient personalized treatment combination out of certified cancer-drugs. Finally, 11 out of 14 patients received 17 prospective treatments based on the findings of the preclinical testing, 15 of which resulted in durable partial remissions [140]. Despite the success, the personalized tumorgraft model has certain limitations: It can only be performed in patients with resectable tumors (20%). Moreover until now, this treatment is limited to special established pancreas-centers with adjacent animal clinic and is still economically unreasonable. Furthermore, a possible drug-resistance of the often developing metastases in PDAC patients may not be detected in these studies. Therefore, testing new drugs in GEMMs described in chapter 1.2.3 may be the strategy of choice for large-scale studies of not approved agents and their combinations.

Several studies using endogenous mPDAC models were published, verifying high predictive value of preclinical GEMMs for diagnostic, chemoprevention and therapy studies [42-44, 141-146]. Since endogenous tumor volume cannot be detected by palpation as subcutaneous, clinically widely used macroscopic imaging systems described in chapter 1.4.1 strongly gained utilization in preclinical studies. Moreover, noninvasive dynamic tumor observation via functional imaging modalities such as [^{18}F]-FDG-PET, DCE-MRI, DW-MRI and contrast US also can provide essential biological tumorspecific information about efficacy of the treatment. For example, Olive at all used high-resolution ultrasound and MRI to underline the importance of stromal compartment in therapy delivery and therefore response to standard therapeutic agents [43]. Moreover they proposed a combination therapy of hedgehog inhibitors with Gemcitabine in order to overcome the stromal barrier and enlarge therapeutic effect measured by increased survival of the animals. In this publication they used high resolution US for tumor growth monitoring and contrast US and DCE-MRI for tumor vitality and perfusion assessment. In addition, the authors emphasized the differences in s.c. and endogenous model perfusion and therefore treatment outcome.

Another key study investigated the response compatibility of murine and human lung and pancreas carcinomas to the standard chemotherapeutics Gemcitabine, EGFR-inhibitor Erlotinib and VEGF-inhibitor CALGB 80303 [42]. Using X-ray micro-computed tomography and high-resolution micro-US to follow tumor progression as well as pharmacokinetic parameters and overall survival, the authors observed high correlation of tumor responses between the human and murine cancers, underling the importance of GEMMs as preclinical platform for therapy monitoring.

A third study performed by Morton J *et al*, evaluated the efficacy of a potential anti-invasive and antimetastatic agent, the Src kinase inhibitor dasatinib in the *Pdx1-Cre;Kras$^{LSL-G12D}$;p53$^{R172H/wt}$* model [44]. In vitro, dasatinib showed inhibited mPDAC cell migration, however did not affect proliferation of the tumor cells. Consequently, although dasatinib significantly reduced the development of lung and liver metastases in vivo, it did not influence the survival of the animals, due to the primary tumor burden. These results suggest that selective use of dasatinib as monotherapy after resection of localized invasive PDAC.

Highly sensitive small animal imaging modalities can also be used for early mPDAC detection and developing of PDAC diagnostic. Indeed, Eser *et al* used flexible confocal laser microscopy in combination with cathepsin-activable near infrared probe for successful *in vivo* detection of mPanIN lesions in a Kras-driven mouse model of PDAC [144]. Moreover, a recent study of Fendrich and colleagues evaluated the use of [^{18}F]-FDG-PET for detection of preneoplatic mPanIN lesions in two endogenous mPDAC models [143]. The authors observed a weak glucose uptake in the

lesions and very strong [^{18}F]-FDG-signal in the resulting mPDAC, correlating with clinical observations and supporting further exploration of PET imaging as diagnostic modality for pancreatic cancer.

In summary, these results suggest that GEMMs indeed possess a very high potential as predictive models for human tumor response to cancer treatments and its noninvasive monitoring via functional imaging.

1.5 Aims of the project

This project has three major objectives:

1) Analysis of the role of Rac1 in the development and progression of murine pancreatic cancer and acute pancreatitis using a genetic approach.

2) Testing of chemical inhibition of Rac1 activity via NSC23766 and EHT1864 in comparison to available chemotherapeutics and other relevant agents *in vitro* and *in vivo*.

3) Optimization and validation of clinically established MRI- and PET-based imaging methods for monitoring of PDAC in endogenous and s.c. transplanted models.

2. Material and methods

2.1 Disclosure of work contribution

All projects goals of this work were approached in a team in the group of PD Dr. J.T. Siveke as well as in cooperation with the group of Dr. R. Braren. None of the researchers have a conflict of interest concerning the data presented in this work.

Specifically:

To aim 1), the analysis of Rac1 in mPDAC models authors contributed as following:

All immunoflourescence staining as well as all experiments on acinar epithelial explants were performed by Dr. C. Lubeseder-Martelato, partially with help of I. Heid. P-MEK stainings were done by Dr. C. Lubeseder-Martelatto. Some of mADM/mPanIN quantifications were calculated twice, by I. Heid and Dr. C. Lubeseder-Martelato in order to ensure the quantification accuracy. Dr. P.K. Mazur has performed the phosphor-ERK ½ and Hes1 stainings. All animals used in the study as well as tissue samples were generated and provided by I. Heid. All further work, the mouse analysis, histological and molecular biological experiments with mouse tissue samples were performed by I. Heid. The Rac1-staining of human samples was generously provided by Prof. Dr. B. Sipos.

To aim 2), testing of possible synergistic therapeutic combinations:

This part of the project was performed by I. Heid, with the exception of the colony formation assay. The assay was performed by Dr. C. Lubeseder-Martelato using cell lines prepared by I. Heid. The *in vivo* study was performed exclusively by I. Heid. The volume calculations of non-treated and Gemcitabine treated animals were kindly provided by Dr. M. Trajkovic-Arsic.

To aim 3), establishing of multi modal imaging patform for preclinical studies:

The project was designed and performed in cooperation with the group of Dr. R. Braren. Therefore the MRI-based measurements as well as volume calculations, DCE and DWI analysis were performed by I. Heid, Dr. M. Trajkovic-Arsic and M.R. Gretzinger. The exact separation of this work is not possible. PET measurements were performed by the core facility of the Department of Nuclear Medicine Klinikum rechts der Isar, Technical University of Munich, supervised by I. Heid. PET data analyses were performed by M.R. Gretzinger and I. Heid. The Movat staining and nuclei quantification for ADC correlation was performed in the lab of Prof. Dr. I. Esposito. Importantly, I. Heid directly participated in the design, performance and analysis as well as establishing of analytic tools of all named imaging studies and obtained a wide solid knowledge of all used techniques.

2.2 Materials

2.2.1 Main equipment and devices

µPET	Inveon, SIEMENS Preclinical Solutions, Knoxville, TN
counter	Totalizer T 120, BaumerIVO
DCE, DWI analysis software	customized IDL
film developer	Amersham Hyperprocessor with X-ray film, Amersham Hyperfilm ECL, GE Healthcare
fluorescence microscope	Axiovert 200M, Zeiss
homogenizer	Heidolph Diax 900, Heidolph Instruments
imaging and quantification software	AxioVision Rel. 4.8 , Modul AutMess, Zeiss
light microscope	Axio Imager.A1, Zeiss
microtome	Microm International and Leica
Molecular Imager Gel Doc XR System	Bio-Rad
Mounting Glasses	Roth, # H877; 1871
MRI	Achieva 1,5 T, Philips Medical Systhems, The Netherlands, Best
MRI viewer and volume analysis software	Customized Image J (64 Bit) Osirix DICOM viewer, http://www.osirix.com Interactive Data Language, ITT VIS, Boulder, CO, USA
Normale PCR cycler	Eppendorf
Osmotic pumps	Alzet,, 1002, 0.25µl/h
Photometer (Protein)	Anthos reader 2001, Anthos
Photometer (RNA, DNA)	Nanodrop ND 1000, PEQLab
RT-PCR cycler	StepOnePlus™ Real-Time PCR System, Applied Biosysthems
RT-PCR plates	TaqMan® Arrays Fast 96 well Plates
RT-PCR software	StepOne Software v2.1
Transfer Membrane	Immobilon-P Transfer Membrane, Millipore, # IPVH 00010
Blood glucose measurement device	Roche
veterinary anesthesia System	Vetland Medical Sales and Services, Louisville, KY, USA
PET analysis software	IRW software package (Inveon Research Workplace, Siemens, Erlangen, Germany
small animal PET/CT system	Inveon, SIEMENS Preclinical Solutions, Knoxville, TN

2.2.2 Buffers and Solutions

All chemicals used in this project were standard products purchased from Roth, Fluka, Merck and Sigma, unless specifically indicated.

SDS page	Separating Gel Buffer: 1.5 M Tris-Base, pH 8,8 Assemble Gel Buffer: 0.5 M Tris-Base, pH 6,8 Running Buffer: 25 mM Tris base, 192 mM Glycine, 0.1 % w/v SDS Laemmli Loading Buffer 0.35 M Tris-Base pH 6.8, 36 % Glycerin, 10.28 % SDS, 0.6 M DTT, 0.012 % bromphenol blue
Western blotting	Transfer Buffer: 25 mM Tris-Base pH 8.3, 150 mM Glycin, 10 % Methanol Blocking Buffer: Skim milk 5 % w/v in TBS/T
tissue fixation buffer	4% PFA in 1x PBS
H&E staining	Histoclear Roti-Histol, Roth; Mayer´s Hemalaum, Merck 20% Eosin/ethanol solution, Croma
X-gal Staining	Fixation solution: 0.2% glutaraldehyde Washing solution: 0.1M PBS, 2mM MgCl2 Staining solution: 1 mg/ml X-gal, 5 mM K3Fe(CN)6, 5mM K4Fe(CN)6 dissolved in washing buffer
tail digestion buffer	Peqlab
proteinase K	Roche
RT-PCR	SYBR® Green PCR Master Mix
PCR mastermix	Red Taq ready mix, Sigma
unmasking solution	VECTOR® antigen unmasking solutions, low pH, high pH
Rac1 assay kit	Upstate (Millipore), Rac1/Cdc42 Activation Assay Kit
tissue lysis buffer	Mg^{2+} Lysis/Wash Buffer, 5X (MLB), Upstate RIPA full buffer: 20 mM Tris-HCl (pH 7.5), 150 mM NaCl, 1 mM Na_2EDTA, 1 mM EGTA, 1% NP-40, 1% sodium deoxycholate, 2.5 mM sodium pyrophosphate, 1 mM b-glycerophosphate, 1 mM Na_3VO_4, 1 µg/ml leupeptin.
TBST	10 mM Tris-Base, 150 mM NaCl, 0.1 % v/v Tween-20
PBS	10x PBS, Biochrom
fetal calf serum	Biochrom
Penicillin/Streptomycin	10% solution Invitrogen
Trypsin	0.05% Solution, Invitrogen
MTT Kit	Cell proliferation Kit I (MTT), Roche Applied Science, Germany

2.2.3 Animal treatment agents and drugs

BrdU Sigma-Aldrich	#B5202-5G, 20 mg/ml in 0.9 % NaCl stock solution
Cerulein	Sigma, # C9026, 1 mg/ml in H_2O stock solution
Isoflurane	Forene, Abbott GmbH Wiesbaden, Germany
NaCl	0,9% isotonic solution, Diaco
Magnograft	Gadopetetat-Dimeglumin, 0,5 mmol/ml, Bayer Shering Pharma AG
Rimadyl	Carprofen 50 mg/ml , Pfizer AG
Temgesic	0.324mg buprenorphine HCl in 1 ml solution, Reckitt Benckiser, UK
Gemcitabine	38 mg/ml GEMZAR® NaCl solution, Eli Lilly and Company

NSC 23766	100 mM H_2O solution, flow rate 0,25 µl/h
EHT 1864	100 mM H_2O solution, flow rate 0,25 µl/h
Glucose	20% injection solution, Diaco

2.3 Methods

2.3.1 Animal models

All experiments were performed according to the guidelines of the local Animal Use and Care Committees.

Endogenous mPDAC were generated using *Ptf1a$^{wt/Cre}$, Kras$^{wt/LSL-G12D}$, Ela-Tgfa-hGH, Trp53$^{wt/LSL-R172H}$, Rac1$^{fl/fl}$, Trp53$^{fl/fl}$ and Rosa$^{26wt/LSL-LacZ}$* mouse strains that were described before [21, 22, 24, 50, 147, 148] (also see Table 1). Animals were crossed according to the animal care guidelines and published crossing strategies. Tail genotyping was performed by polymerase chain reaction using described primers (Table 4). All mice were of mixed 129SV/C57BL/6 background. The genotypes are listed in Table 3. As control mice (*WT*) were used littermates, which do not express Cre-recombinase.

Table 3: Genotype abbreviations.

Ptf1a$^{wt/Cre}$ LSL-Kras$^{wt/LSL-G12D}$	*CK*
Ptf1a$^{wt/Cre}$ Kras$^{wt/LSL-G12D}$ Ela-Tgfa-hGH	*CKT*
Ptf1a$^{wt/Cre}$ Rac1$^{fl/wt}$	*CR$^{fl/wt}$*
Ptf1a$^{wt/Cre}$ Rac1$^{fl/fl}$	*CR$^{fl/fl}$*
Ptf1a$^{wt/Cre}$ Kras$^{wt/LSL-G12D}$ Rac1$^{fl/wt}$	*CKTP$^{mut/wt}$*
Ptf1a$^{wt/Cre}$ Kras$^{wt/LSL-G12D}$ Rac1$^{fl/fl}$	*CKR$^{fl/fl}$*
Ptf1a$^{wt/Cre}$ Kras$^{wt/LSL-G12D}$ Ela-Tgfa Rac1$^{fl/wt}$	*CKTR$^{fl/wt}$*
Ptf1a$^{wt/Cre}$ Kras$^{wt/LSL-G12D}$ Ela-Tgfa Rac1$^{fl/fl}$	*CKTR$^{fl/fl}$*
Ptf1a$^{wt/Cre}$ Kras$^{wt/LSL-G12D}$ Trp53$^{fl/wt}$	*CKP$^{fl/wt}$*
Ptf1a$^{wt/Cre}$ Kras$^{wt/LSL-G12D}$ Trp53$^{fl/fl}$	*CKP$^{fl/fl}$*
Ptf1a$^{wt/Cre}$ Kras$^{wt/LSL-G12D}$ Ela-Tgfa Trp53$^{fl/wt}$	*CKTP$^{fl/wt}$*
Ptf1a$^{wt/Cre}$Kras$^{wt/LSL-G12D}$Ela-Tgfa Trp53$^{R172H/wt}$	*CKTP$^{mut/wt}$*
Ptf1a$^{wt/Cre}$ Rac1$^{fl/fl}$ Rosa$^{26wt/LSL-LacZ}$	*CR$^{fl/fl}$Rosa*
Ptf1a$^{wt/Cre}$ Kras$^{wt/LSL-G12D}$ Trp53$^{fl/wt}$ Rac1$^{fl/wt}$	*CKP^{mut}R$^{fl/wt}$*
Ptf1a$^{wt/Cre}$ Kras$^{wt/LSL-G12D}$ Trp53$^{fl/wt}$ Rac1$^{fl/fl}$	*CKP^{mut}R$^{fl/fl}$*

Subcutaneous (s.c.) mPDAC tumors were generated by implantation of T510481 primary mPDAC cell line derived from a tumor of *Ptf1a$^{wt/Cre}$Kras$^{wt/LSL-G12D}$Tgfa* genotype into both flanks of male wild type C57/Bl6 mice ($5x10^5$ diluted in DMEM/flank).

Acute pancreatitis was induced by administration of 8 hourly intraperitoneal (i.p.) injections of cerulean (10 µg/kg body weight) over 2 consecutive days as described previously [41]. Pancreata were analyzed 0, 24 and 72 hours after the last injection.

2.3.2 Drug treatment protocols

Anesthesia protocol

During imaging and cell transplantation mice were anesthesized by continuous gaseous infusion of 1.8 - 2% isoflouran mixed with 1% O_2 for at least 10 min prior any procedure using veterinary anesthesia system. Animal temperature was maintained and continuously monitored and eyes were protected with an eye ointment.

Pain treatment protocol

Upon detection of signs of pain mice received s.c. injections of rimadyl (4 - 5 mg/kg) and/or temgesic (0.05 – 0.1 mg/kg).

Gemcitabine / NaCl treatment

S.c. implanted tumors were allowed to grow till they could be detected by palpation (7-10 days). Upon detection of solid tumor minimum size of 5 mm^3 mice were randomized in 2 groups of similar mean tumor volumes for the evaluation of therapy response monitoring. Therefore, animals were injected twice a week with 120 mg/kg body weight with Gemcitabine or 0.9% NaCl solution for the total duration of 2 weeks. Endogeneous tumors were treated twice a week with 120 mg/kg body weight with Gemcitabine after the tumor detection by MRI. The number of analyzed animals varied due to the difficulties of animal generation and animal health at the time point of the study.

Glucose Tolerance Test

Glucose tolerance test (GTT) was performed on mice after 12 hours overnight fasting. Glucose was injected i.p. (2 g/kg, using 20% glucose solution). Blood glucose levels were assessed by collecting tail blood, and glucose level data were recorded at indicated time points.

Animal euthanasia and BrdU treatment

Animals showing morbid symptoms such as weight loss (more than 15%), apathy, fur irregularities and ascites were sacrified immediately and considered as died of natural death. Animals were injected with BrdU (i.p. 50 mg/kg body weight) 2h prior of sacrifice.

Rac1 inhibitor administration

NSC23866 and EHT1864 are both water soluble to a maximum concentration of 100 mM. Alzet® osmotic pumps (model 1002, flow rate 0.25 µl/h) were filled with 100µl of 100 mM solution of each inhibitor according to manufactures instructions. Two pumps were placed s.c. in to the torso of a mouse as previously published [106] following general anesthesia and pain treatment with rimadyl and temgesic The pumps remained in the animal for a time period of 2 weeks.

Magnetic resonance imaging

Based on mean survival time (Fig. 27B) and observed approximate tumor onset time, regular anatomy screening was performed by T2w MRI. Thereby, mice were subjected to serial (weekly/every 2 weeks) T2w MRI scans from 4-6 weeks of age onwards using 1.5 T clinical scanner with a 47-mm microscopy surface coil. Particularly, after fixation of a tail vein catheter, animals were placed in prone position on top of a 47-mm microscopy surface coil in the MRI Scanner. An axial multi-slice T2-weighted (T2w) turbo spin-echo (TSE) sequence (resolution 0.3 x 0.2 x 0.7 mm^3, minimum 35 slices, TE = 90 ms, TR > 3 s, NSA = 8) covering the complete mouse abdomen and/or thorax was applied as anatomical reference and for tumor detection and tumor volume quantification. Upon detection of solid tumor with minimum size of 5 mm^3, DWI- and DCE-

MRI protocols were applied (described below). MRI data were correlated with survival analysis and histopathology of tumor specimens.

For therapy monitoring validation, animals bearing s.c. implanted tumors were subjected to T2w MRI from the time point, where the tumors could be detected by palpation (7-10 days). Control and treatment group received multimodal multiparametric imaging once before and, at weekly intervals, twice after intervention. T2w MRI, DCE-MRI and [^{18}F]-FDG-PET scans were performed within 24 hours.

Dynamic contrast enhanced and diffusion weighted MRI

DCE-MRI experiments were performed during free breathing using a previously described fast single-shot Look-Locker based radial T1 mapping technique using the golden cut principle (LLGC) [149, 150]. A bolus (≤ 1 s) of dose 0.04 mmol/kg of Gd-DTPA (Magnevist®) was administered after 60 s. Dynamic T1 mapping of one axial slice positioned over the tumor(s) and spinal muscles was performed every 6 s for 10 - 20 min. (resolution = 0.71 x 0.71 x 2 mm^3, TR/TE = 12.6/5.7 ms, radial profiles = 206, flip angle = 10°, T_{acq} = 2.6 s, T_{pause} = 3.4 s).

Following the DCE-MRI experiment, an axial multi-slice diffusion-weighted MRI (DWI) sequence covering the tumors was performed (resolution 0.38 x 0.71 x 1.5 mm^3, TSE factor = 43, TR/TE = 2500/58 ms, $b_{0\text{-}2}$ values = 20, 200, 600 s/mm^2, NSA = 10).

Positron emission tomography

Study inclusion criteria for PET imaging were solid lesions of minimal size of 5 mm^3 detected via T2w-MRI. Animals were fasted at least 4 h prior to imaging. Static image acquisition was performed 45 min after injection of 5–12 MBq [^{18}F]-FDG or [^{18}F]-FLT-PET via a tail vein catheter for 15 min using a dedicated small animal PET/CT system. Data was reconstructed with a filtered backprojection algorithm with a cut-off at the Nyquist frequency. Image data was corrected for normalization, dead time and decay. No corrections for scatter and attenuation were carried out. For therapy response monitoring, animals were subjected to [^{18}F]-FDG measurements once before and once after therapy treatment.

2.3.3 Imaging data analysis

Volume analysis was carried out using in-house adapted ImageJ software for semi-automatic segmentation of cystic, necrotic and solid compartments calculated from the T2w data sets exported by Osirix DICOM viewer. A growth curve fitting was performed using R and Graphpad Prism 4.0 software.

DCE-MRI and DWI data were analyzed using in-house software written in the Interactive Data Language software.

For DCE-MRI analyses the initial area under the vital tumor and spinal muscle Gadulinium-concentration curve until 90s, i.e. $iAUC90_{tumor}$ and $iAUC_{muscle}$ were computed using trapezoidal rule. In addition, the relative $iAUC90_{rel}$ = $iAUC90_{tumor}$/ $iAUC_{muscle}$ was calculated for statistical comparison.

ADC maps were generated using the equation: ADC = $\frac{\ln\left(\frac{S2}{S0}\right)}{b2-b0}$ with S0 = S(b0) and S2 = S(b2), Median ADC values were calculated for each tumor, excluding slices exhibiting distortion artifacts.

Color-coded PET and T2w gray scale image data were fused using the IRW software package. 3D volumes of interest (VOI) covering the entire tumor volume were drawn on the fused PET-MRI images. Thresholds were then defined to select the maximum 50% count rates within these VOIs

(isocontour50). Two 3D ROIs were placed in the spinal muscle at the level of the kidneys. Tumor-to-muscle uptake ratios, $mean_{isocontour50}/mean_{muscle}$, were calculated.

2.3.4 Cell culture and in vitro studies

Isolation and culturing of primary mouse tumor cell lines

Cells were isolated from mPDAC of endogenous mice according to a modified protocol described previously [151]. Briefly, three fragments from different tumor regions were minced and digested twice in 10 ml digestion buffer for 20 minutes at 37°C. Thereafter cells were resuspended in DMEM containing 10% of fetal calf serum and 1 % of Penicillin/Streptomycin and transferred into a standard plastic tissue culture dish. All cells were cultured under the standard conditions in a humidified incubator containing 5% CO_2 in air at 37°C. For any of experiments, cells were used in passage 3-15. For s.c. transplantation cells were expanded, trypsinized, washed once with PBS, resuspended in DMEM to an indicated concentration and transplanted into the animals.

Cell viability assays

Primary tumor cell lines were seeded on 96-well plates, allowed attaching over night and treated with tested drug or drug combinations for 72 hours. The tetrazolium salt, MTT was added for 4 hours to the cells following by lysisbuffer and incubated over night at 37°C according to kit instructions. MTT is cleaved only by living cells in the presence of an electron-coupling reagent thereby producing water-insoluble formazan salt. After solubilization, the formazan dye was quantitated using a scanning multi-well ELISA reader at OD600. The absorbance revealed directly correlates to the living cell number.

Preparation of Pancreatic Epithelial Explants Culture and Immunofluorescence of Acinar Epithelial Explants

All experiments with acinar epithelial explants were performed by Dr. C. Lubeseder-Martelato, partially with help of I. Heid and are described in Heid et al. [152]

2.3.5 Histological analysis

Immunohistochemistry and Immunofluorescence

Tissue was collected immediately after the eutanasation and fixed in 4% PFA/PBS solution for 24–48 h at 4°C, dehydrated under standard conditions, and embedded in paraffin. Serial 3 µm-thin sections were collected every 500 µm and subjected to histological analysis.

H&E staining was performed on deparafined in descending alcohol rehydrated sections with Eosin and Mayer's Haemalaun according to standard protocol. For Imaging analysis all tumors were correlated with the T2w scans to identify the region of interest and exact tumor location for further histological analyses.

Immunoperoxidase staining was performed on 4% PFA/PBS fixed paraffin-embedded tissue slides using the Vectastain ABC Elite kit (Vector Labs) following manufacturer's instructions. All antibodies used as well as unmasking and blocking conditions are listed in Table 5. All primary antibodies were incubated over night at 4°C and secondary 1h at room temperature. Sections were counterstained with Hematoxylin and mounted with Pertex.

For immunofluorescence staining, cryosections (6 µm) were fixed with PFA 2% for 20 min and permeabilized with Triton X-100 0.1 % for 5 minutes. The first antibodies were incubated overnight at 4°C, and secondary antibodies were incubated for 1 h (Alexa dyes, Invitrogen) at

room temperature. Sections were mounted with Vectashield hard mounting medium containing DAPI (Vector Laboratories).

ß-Galactosidase staining

The 6-12µm thick sections were fixed in 0.2% glutaraldehyde for 1h, washed 3 times with washing solution and incubated overnight in staining solution in the dark. Thereafter slides were washed again, counterstained with nuclear red (Vector Labs) and mounted with Pertex.

Quantification of IHC staining

For quantification analysis 3 paraffin sections per mouse from 3 animals per genotype were stained using respective antibodies. To assess the distribution of the antigen of interest, 3 optical fields per section (in total 18/genotype) were analyzed using AxioVision 4.8software and displayed as the percentage of positive cells per region. For mPanIN/ADM quantification, H&E or CK19 stainings were quantified using 1 representative slide per mouse. At least 10 pictures were taken from each slide, and the amount of lesions was calculated manually.

2.3.6 Western Blotting and Rac1 Activity Assay

A piece of pancreas was frozen in liquid nitrogen immediately after sacrifizing the mice. GTP-bound Rac1 was pulled down from whole pancreas tissue lysate in MLB-buffer containing complete protease and phosphatase inhibitors (Roche) according to the manufacture instruction (Upstate, Millipore). Briefly, pancreatic tissue/primary pancreatic tumor cells were lysed in 300-500µL MLB buffer and stored on ice. After adjusting of protein concentration with Bradford-assay kit (Bio Rad) 1000µg of each sample were incubated with 40 µl of Pac1-PBD-agarose for 1h at 4°C. Thereafter agarose was pulled down by short centrifugation at highest speed, samples were washed 3 times in MLB buffer and eluated with 2x WB sample buffer for 5 min at 95°C. The visualization of total and GTP-bound Rac was performed using standard Western-blot.

For whole-tissue pancreatic protein analysis lysates were prepared by homogenizing pancreatic tissue in RIPA buffer containing complete protease and phosphatase inhibitors (Roche) and separated on a 7.5-15% polyacrylamide- SDS gel, transferred to PVDF membranes and blocked in 5% BSA or skim milk followed by antibody incubation overnight at 4°C. All whashing steps were carried out using 1x TBST. Antibodies used are shown in table 5. Antibody binding was visualized using horseradish peroxidase-labeled secondary antibodies and ECL reagent (Amersham).

2.3.7 Genotyping PCR and RT-PCR analysis

For genotyping, isolated tail DNA was subject to PCR analysis for the genes of interest with the respective primer, using the “RedTaq ReadyMix PCR REACTION MIX” according to the manufacturer’s protocol. Primers were purchased from MWG Biotech AG. 40 PCR cycles were performed as following: denaturation 95°C 5 min; cycles 1 – 40: denaturation 94°C 30 sec, annealing 58°C 30 sec, elongation 72°C 90 sec; substrate clearance 72°C 10 min.

For RT-PCR experiments, total RNA was extracted from shock-frozen pancreatic tissues of at least three different regions with the RNeasy Kit (Qiagen). cDNA was synthesized with SuperScript II reverse transcriptase (Invitrogen). Real-time PCR analysis was performed on a Gene Amp 7700 sequence detection system from AppliedBiosystems using SYBR Green PCR mix. PCR reactions were performed as described previously[22, 23, 152] using the dCT method and listed primers (also see Table 4).

2.3.8 Statistical analysis

Kaplan–Meier curves were calculated using the survival time for each mouse from all littermate groups and log rank test for significance. For all other analyses, the unpaired two tailed Student's t-test or one way ANOVA were performed with $P < .05$ considered as significant.

Table 4: List of used PCR primers, 5' - 3'.

name	forward	reverse
Rac1_genotyp	TCC AAT CTG TGC TGC CCA TC	GAT GCT TCT AGG GGT GAG CC
Rac1_recomb	CAG AGC TCG AAT CCA GAA ACT AGT	GAT GCT TCT AGG GGT GAG CC
Cre_genotyp	ACC AGC CAG CTA TCA ACT CG	TTA CAT TGG TCC AGC CACC
Cre_genotyp	CTA GGC CAC AGA ATT GAA AGA TCT	GTA GGT GGA AAT TCT AGC ATC ATC C
p53R172H-genotyp	AGC CTT AGA CAT AAC ACA CGA ACT	CTT GGA GAC ATA GCC ACA CTG
p53R172H-genotyp	GCC ACC ATG GCT TGA GTA A	CTT GGA GAC ATA GCC ACA CTG
p53flfl_genotyp	CAC AAA AAC AGG TTA AAC CCA	AGC ACA TAG GAG GCA GAG AC
Kras_genotyp	AGC TAG CCA CCA TGG CTT GAG TAA GTC TGC A	CCT TTA CAA GCG CAC GCA GAC TGT AGA
TGFa_genotyp	TGA GAG GTC ATA GAC GTT GC	GGC TTT TTG ACA ACG CTA TG
Rosa_genotyp	GCG AAG AGT TTG TCC TCA ACC	AAA GTC GCT CTG AGT TGT TAT
Pdx1_qRT	TGCCACCATGAACAGTGAGG	GGAATGCGCACGGGTC
Notch2_qRT	CCCAGAACCAATCAGGTTAGC	GCCGAGACTCTAGCAATCACAA
Notch3_qRT	TGGCTCTACTGCACTGATCCTG	CAAGCTCATCCACTGCATTGAC
Hes1_qRT	AAAATTCCTCCTCCCCGGTG	TTTGGTTTGTCCGGTGTCG
Shh_qRT	CAAAGCTCACATCCACTGTTCTG	GAAACAGCCGCCGGATTT
Ptch_qRT	TTGTGGAAGCCACAGAAAACC	TGTCTGGAGTCCGGATGGA
Gli1_qRT	TGGACTCTCTTGACCTGGACAAC	GGCCCTGGGCCTCATC
Gli3_qRT	CCAGCCGAAAACGTACACTGT	GGGATGTTCTTATCATGGTCTGAA
Cxcl-2_qRT	AGT GAA CTG CGC TGT CAA TGC	AGG CAA ACT TTT TGA CCG CC
Cxcl-1_qRT	TGG GAT TCA CCT CAA GAA CA	TTT CTG AAC CAA GGG AGC TT
Cxcl-10_qRT	GAA TCC GGA ATC TAA GAC CAT CAA	GTG CGT GGC TTC ACT CCA GT
Ccl-3_qRT	CCA AGT CTT CTC AGC GCC AT	TCT TCC GGC TGT AGG AGA AGC
Tnf-α_qRT	ATG AGA AGT TCC CAA ATG GCC	TCC ACT TGG TGG TTT GCT ACG

IL-1β_qRT	CTC AAT GGA GAG AAT ATC AAC CAA CA	ACA GGA CAG GTA TAG ATT CTT TCC TTT G
GM-GSF_qRT	AAG GGT CCT GAG GAG GAT GTG	GAG GTT CAG GGC TTC TTT GA
IL-6_qRT	TCG GAG GCT TAA TTA CAC ATG TTC T	GCA TCA TCG TTG TTC ATA CAA TCA
Cyclophyllin a_qRT	ATGGTCAACCCCACCGTGT	TTCTGCTGTCTTTGGAACTTTGTC
Rac1_qRT	CGGAGCTGTTGGTAAAACCTG	ATAGGCCCAGATTCACTGGT
Rac2_qRT	TGGGCCTCAGATGCAATGCAG	ATAGTCCTCCTGACCTGCGG
Rac3_qRT	ATCAAGTGCGTGGTGGTTGGC	TCCCGCAGCCGTTCAATCGT
GAPDH	TACTAGCGGTTTTACGGGCG	TCGAACAGGAGGAGCAGAGAGCG A

Table 5: List of antibodies and applications.

antibody	species	dilution	application	company
Hsp90	rabbit	1:1000	WB	Cell signaling
Actin	mouse	1:5000	WB	Sigma
Amylase	goat	1:1000, 1:200	WB / IHC / IF	Santa Cruz
E-cadherin	goat	1:200	IHC/ IF	R&D
BrdU	rat	1:250	IHC	Serotec
Muc5A	mouse	1:100	IHC	Neomarkers
Rac1	mouse	1:1000	WB	Upstate
Rac1	mouse	1:100	IHC / IF	BD
Insulin	rabbit	1:200	IHC	DAKO
Glucagon	guinea pig	1:200	IHC	DAKO
CK19 (TROMAIII)	rat	1:200	IHC	DSHB
E-cadherin	rabbit	1:100	IF	Cell signaling
Cyclin D1 (sc-718)	rabbit	1:100	WB	Santa Cruz
Phospho-p44/42 MAPK (9106S)	mouse	1:2000	WB	Cell Signaling
Phospho-p44/42 MAPK (4376S)	rabbit	1:100	IHC	Cell signaling
Phospho β-Catenin (9561S)	rabbit	1:1000	WB	Cell signaling
Stat3	mouse	1:1000	WB	BD
Phospho Stat3 (9145S)		1:100, 1:1000	WB, IHC	Cell signaling

Phospho-EGFR (Tyr1173)	goat	1:500	WB	Santa Cruz
EGF Receptor	rabbit	1:1000	WB	Cell signaling
Phospho Akt (Ser 473)	rabbit	1:1000	WB	Cell Signaling
CD 45	rat	1:200	IHC	BD
α smooth muscle actin	mouse	1:100	IHC	Dako

3. Results

3.1 The role of Rac1 in murine PDAC development and chemically induced acute pancreatitis

3.1.1 *Rac1* overexpression increases with murine PDAC progression in different mouse models

In order to investigate possible involvement of *Rac1* in the initiation and/or progression of *Kras*-induced murine pancreatic cancer, *Kras*$^{wt/LSL\text{-}G12D}$ (*K*) mice were crossed to *Ptf1a*$^{wt/Cre(ex1)}$ (*C*) mice as previously described [21, 22] (for genotype abbreviations see table 3). The gene and protein expressions of *Rac1* in murine PDAC were analyzed at several time points as shown in figure 6. In *CK* model, the overexpression of total *Rac1* started approximately at the age of 1 month, because no upregulation of *Rac1* was noticed at the age of 7 days (Fig. 6A-C). Levels of active, GTP-bound form of Rac1 were not changed in *CK* and *WT* mice (Fig. 6B) at the age of 1 month. This finding suggests that the transformation process in the pancreas of *CK* mice starts approximately at 1 month, since histological analysis of 1 month-old pancreata (Fig. 6D) confirmed the presence of scattered, few ductal-like metaplastic structures associated with only some mPanINs. The amount of total *Rac1* significantly increased during the course of the disease progression on both mRNA (Fig. 6C, 6 months) and protein level in the *CK* model (Fig. 6A, 9 months).

In addition, the status of *Rac1* mRNA and protein was analysed in a second model of pancreatic cancer: *Ptf1a*$^{wt/Cre(ex1)}$*;Kras*$^{wt/LSL\text{-}G12D}$*;Ela-Tgfa(T)* (*CKT*) mice [21, 22] (for genotype abbreviations see table 3). It was previously described that enhanced EGFR signaling induced via overexpression of its main ligand TGFa strongly accelerates mPanIN progression and leads to mIPMN precursor development as well as increased tumor incidence compared to the *CK* model [21, 22]. Indeed, due to the increased EGFR-signaling activation, *Rac1* was strongly upregulated in pancreata of this model already at the very early age of 7 days (Fig. 6A,C). The expression pattern correlated with the histology of a 7 days old *CKT* pancreas showing start of ADM/PanIN formation (Fig. 6D). Consequently, at the age of 1 month, when the histological analyses revealed great areas of ADM/mPanIN development (Fig. 6D), total and GTP-bound Rac1 were present at significantly higher levels compared to both *WT* and *CK* mice (Fig. 6B).

Following the findings described above, presence and localization of Rac1 was analyzed on tissue samples taken from 6 months-old *CK* pancreata. Here, Rac1 was weakly expressed in normal acini (Fig. 6E). Moreover, only ADM (Fig. 6E top panel) but not PanIN (Fig. 6E bottom panel) expressed basally Rac1. This observations, strongly suggest a transient acinar and metaplastic Rac1 expression whitch disappears in mPanIN lesions. Interestingly, both murine and human preneoplastic as well as malignant tissue revealed a strong Rac1 expression in mPanIN and mPDAC surrounding stromal and inflammatory compartment (Fig. 6E-G).

Taken together, these results confirm a strong correlation between Rac1 overexpression and the increasing mataplastic process during mPDAC progression. As expected, abnormal activation of EGFR signaling caused an earlier and more pronounced Rac1 upregulation in the pancreas following accelerated ADM/mPanIN formation.

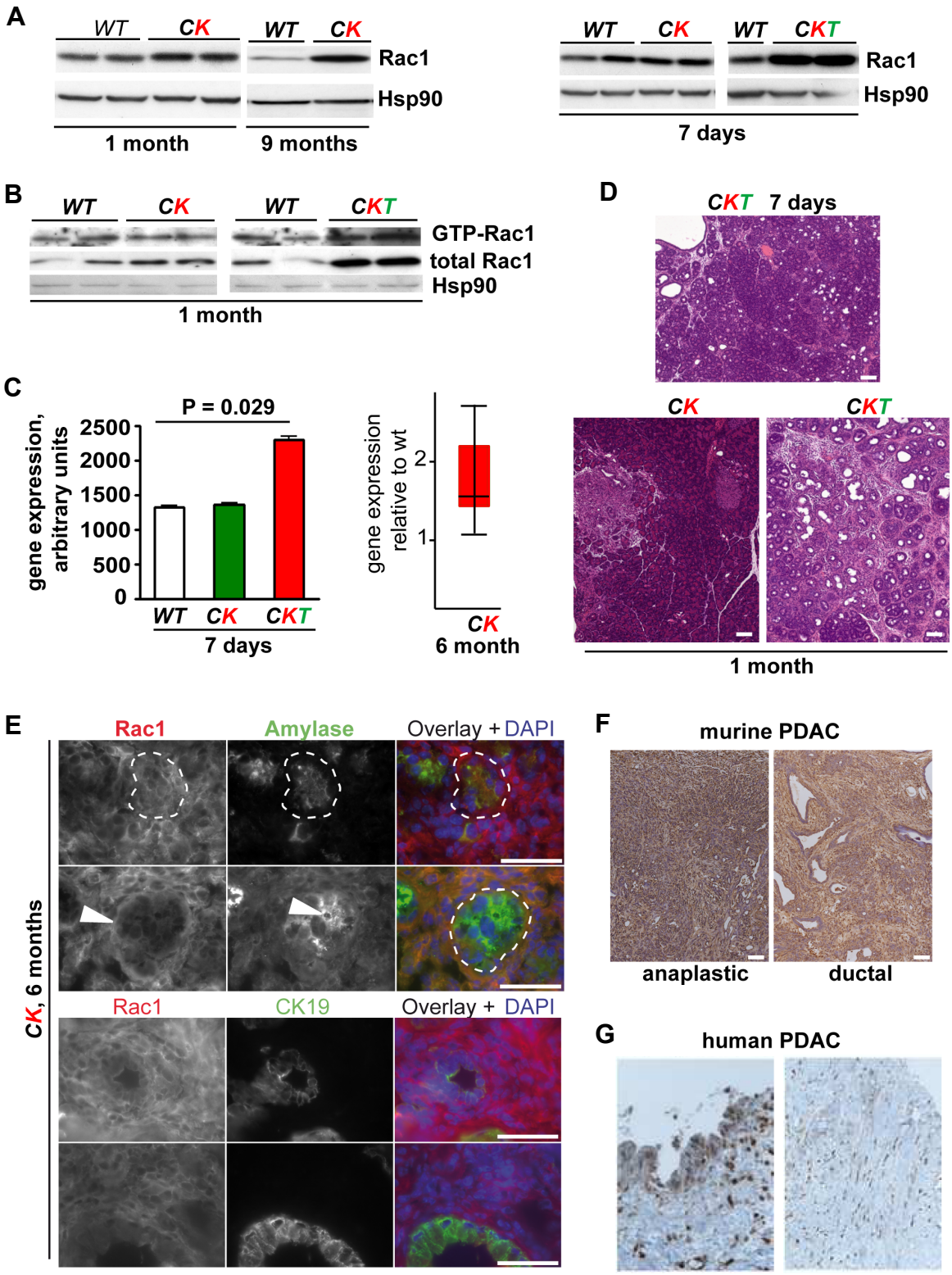

Figure 6: Rac1 expression increases during murine and human pancreatic cancer progression. A: Immunoblot analyses of pancreatic whole-tissue lysates show enhanced protein levels of total Rac1 in the *CK* model at time points of 1 and 9 months (left panel). In the *CKT* model (right panel) the amount of total Rac1 in the pancreas is augmented already at 7 days after birth. Hsp90 serves as loading control. B: Pull down assay of pancreatic whole-tissue lysates. The level of active GTP-Bound Rac1 is unchanged in 4 weeks-old *CK* pancreata compared to the *WT*. *CKT* pancreata reveal significantly increased GTP-Rac1 at the same time point. C: mRNA analysis of *Rac1* expression in mouse pancreas of indicated phenotype detected by micro-array (left panel, n = 4/group) and quantitative RT-PCR (n = 4/group, P = .029). D: Pancreas histology (H&E) reveals only few mADM/mPanIN lesions in the 1 month-old *CK* and 7 days-old *CKT* mice marking beginning of metaplastic process, whereas 1 month-old *CKT* animals show abundant

changes. E: Immunofluorescence double stainings for Rac1 and amylase (top) or CK19 (bottom) in 6-months-old pancreatic tissue of *CK* mice. Rac1 is weakly expressed in normal acini and localizes basally while ADM progression (top panel, white arrow). At the same time Rac1 expression is increased in surrounding stromal tissue. In PanIN lesions Rac1 expression is nearly absent (bottom panel). F, G: Immunohistological staining of Rac1 in murine (F) and human (F) PDAC tissue. Scale bar = 50 µm.

3.1.2 Loss of Rac1 leads to no major pancreatic abnormalities

Rac1 is ubiquitously expressed during pancreas development in all pancreatic compartments, including ductal, acinar, endocrine and mesenchymal cells [68]. In order to analyze whether Rac1 deletion has an effect on the pancreas formation itself, previously described floxed $Rac^{fl/fl}$ (*R*)[147] mice were crossed with $Ptf1a^{wt/Cre}$ (*C*) line in order to generate $CR^{fl/fl}$ genotype (Fig. 7A, for genotype abbreviations see table 3). $CR^{fl/fl}$ mice were viable and born at the expected Mendelian ratio. The successful Cre-mediated recombination of the floxed loci in the pancreas was proven by genotyping PCR analyses from DNA of isolated pancreatic and control organs tissue samples (Fig. 7B). Moreover, X-gal staining of cryosections from the $CR^{fl/fl}Rosa26R^{LSL\text{-}LacZ}$ reporter line showed strong blue coloration of acini, ducts as well as islets of Langerhans, proving correct recombination in all compartments (Fig. 7C). In addition, Western Blot analysis and immunofluorescence staining (Fig. 7D) revealed clear ablation of Rac1 in the pancreas of 1 month-old animals.

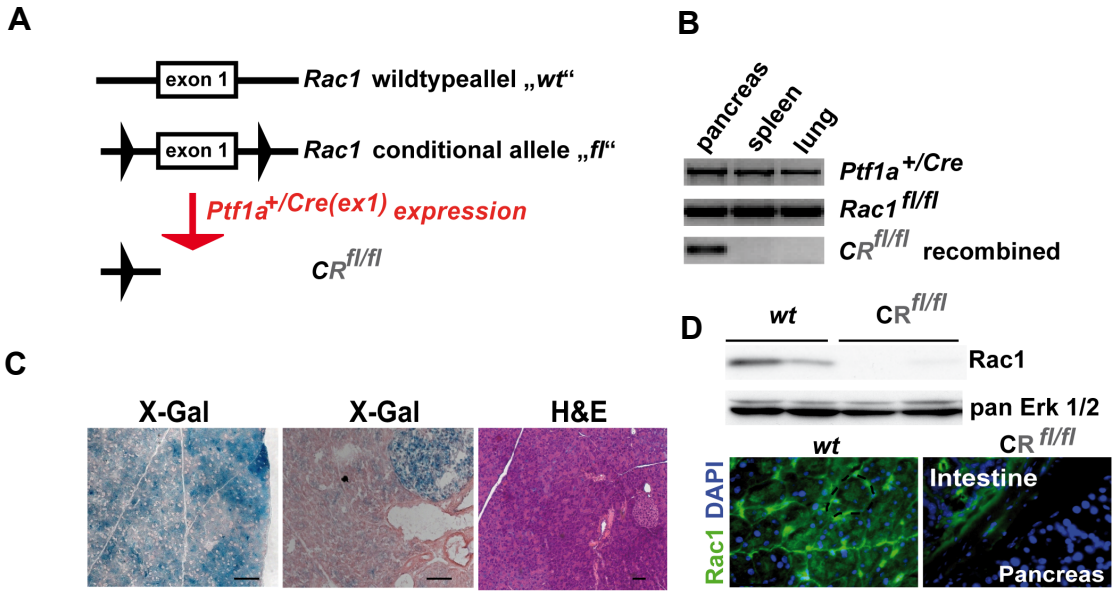

Figure 7: Pancreas specific ablation of *Rac1* in $CR^{fl/fl}$ mice. A: Diagram of Cre-mediated recombination. Adapted from 147. B - D: Rac1 is specifically deleted in pancreas tissue. B: PCR analysis of fresh isolated tissue samples from a 6 moth old $CR^{fl/fl}$ mouse. The recombined allele is present only in pancreas tissue. C: X-Gal staining on cryo-sections from CRfl/flRosa mouse pancreata. Abundant blue positive acinar and island cells demonstrate high Cre expression and pancreas specific recombination (left and middle panel). H&E staining of pancreas from a 6 months old $CR^{fl/fl}$ mouse shows grossly normal histology (right panel). Scale bar = 50 µm. D: Immunoblotting and immunfluorescence staining of Rac1 expression in 1 month-old pancreatic tissue of indicated genotype.

Histological analyses of $CR^{fl/fl}$ animals at different time points revealed normal gross morphology of the pancreas up to the higher age (18 month) (Fig. 7C, data not shown). Also, analysis of acinar cellular integrity and possible changes of adherent junctions by E-cadherin and ZO-1 staining (Fig. 8A) as well as ß-cathenin expression (Fig. 8B) revealed no differences compared with the *WT* tissue samples.

Greiner *et al* described 2009 a transgenic mouse model expressing dominant negative Rac1 under the rat insulin promoter, which mainly resulted in the disrupted island cell migration. In $CR^{fl/fl}$ model an increased association of pancreatic islands with the adjacent ducts was also present. Furthermore, glucose tolerance test (GTT) revealed a minor impairment in the endocrine function in 1 month-old $CR^{fl/fl}$ mice (Fig. 8C), which also persisted in older animals (data not shown). However, neither total body weight nor size of the $CR^{fl/fl}$ mice was altered compared to the WT littermates (data not shown). Moreover, immunohistological analyses of $CR^{fl/fl}$ pancreatic tissue demonstrated normal expression of endocrine markers (insulin and glucagon) (Fig. 8C).

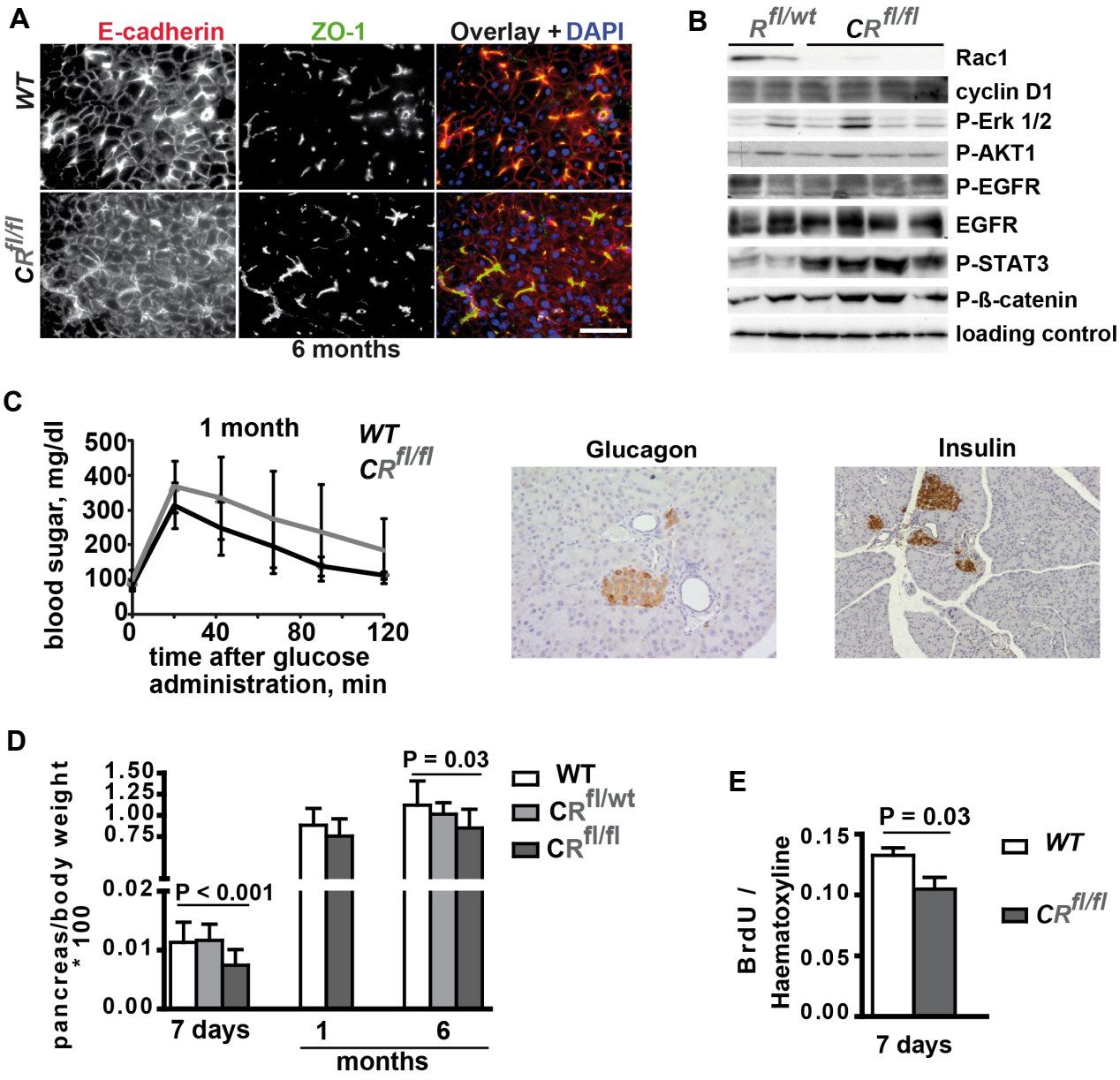

Figure 8: Deletion of *Rac1* in $CR^{fl/fl}$ model does not lead to histological changes however has a mild impact on pancreatic endocrine function and proliferative capacity. A: Acinar cellular integrity is normal in $CR^{fl/fl}$ animals. Immunofluorescence analysis of E-cadherin (red) and ZO-1 (green) in pancreata of *WT* and $CR^{fl/fl}$ mice shows intact adherent junctions. Scale bar = 50 µm. B: Deletion of *Rac1* in $CR^{fl/fl}$ model has no impact of the main EGFR-signaling effectors and ß-cathenin, except for the elevated phospho-STAT3 activation. Immunoblott analysis of 1 month-old whole-pancreas lysates, P = phosphorylated form. C: Glucose tolerance test on 1 month-old animals reveals only slight delay in glucose uptake in $CR^{fl/fl}$ mice compared to the *WT* littermates (n = 4/group). Immonohistological analyses of the same mice show normal expression of endocrine markers (insulin and glucagon). D: Ratio of pancreas / body weight of $CR^{fl/fl}$ animals at indicated time point shows a slight yet significant decrease compared to

the *WT* littermates (n = 3-5/group). E: The $CR^{fl/fl}$ animals have a significantly reduced proliferation rate in the 7 days old pancreas (n = 4/group).

Merely, analysis of pancreatic weight in $CR^{fl/fl}$ mice revealed significant decline compared to the *WT* pancreata beginning at the 7 days and persistent trough the adulthood (Fig. 8D). In addition, a reduced proliferative capacity of the $CR^{fl/fl}$ pancreas was observed at the time point of 7 days (Fig. 8E). In order to explore the mechanism of diminished proliferation immonoblotting analysis were performed on 1 month-old whole-pancreas lysates of $CR^{fl/fl}$ mice (Fig. 8B). Interestingly, neither activation of EGFR nor expression of cyclin D1 or phospho-Erk1/2 - known modulators of proliferation - was changed in these samples. However, a strong STAT3 activation was observed and confirmed by IHC analysis (data not shown), suggesting that this pathway is more important for acinar cell integrity in $CR^{fl/fl}$ mice. Taken together, deletion of *Rac1* following *Ptf1a* induced Cre-recombination resulted in no major pancreatic abnormalities.

3.1.3 Ablation of *Rac1* reduces early mPanIN burden and impairs mPDAC development

In order to investigate the role of Rac1 in pancreatic carcinogenesis $Ptf1a^{wt/Cre(ex1)}$ and $R^{fl/fl}$ mice were crossed to the $Kras^{wt/LSL\text{-}G12D}$ (*K*) line to obtain $Ptf1a^{wt/Cre}Kras^{wt/LSL\text{-}G12D}Rac1^{fl/fl}$ ($CKR^{fl/fl}$) mice (for genotype abbreviations see table 3). Loss of both *Rac1* alleles resulted in a significantly smaller pancreas and an absence of visible cysts, typical for the age of 6 months in the *CK* model (Fig. 9A). The pancreas/body weight index of $CKR^{fl/fl}$ animals dropped to the levels of *WT* littermates (Fig. 9B), however the proliferative capacity of 7 days-old pancreatic tissue in all models remained unchanged (Fig. 9D). Comparison of *CK* and $CKR^{fl/wt}$ cohorts (n = 5 each) revealed very similar gross morphological and histological appearance (data not shown, Fig. 9A-C), suggesting that one allele of Rac1 is sufficient to support the metaplastic transdifferentiation. Thereby, by the time of 6 months larger areas of the pancreas were replaced by mADM/PanIN1-2 surrounded by abundant stroma, high quantity of inflammatory infiltrates and fibrosis were observed in $CKR^{fl/wt}$ model (Fig. 9C). In contrast, histological analysis of the $CKR^{fl/fl}$ mice (n = 8) at 6 months of age showed almost normal pancreas with small rare areas of mADM/PanIN development (Fig. 9C). Consequently, the reduction of pancreatic weight was attributed to an impressive impairment of mADM/PanIN development and substantial reduction of adjacent stroma in $CKR^{fl/fl}$ model compared to *CK* or $CKR^{fl/wt}$ pancreas (Fig. 9C). The amount of detected lesions was significantly lower as quantified in Fig. 9E (P = .003 for comparison of *CK and* $CKR^{fl/fl}$ pancreata; P = .159 for evaluation of $CKR^{fl/wt}$ *and* $CKR^{fl/fl}$ animals). This observations lead to the conclusion, that deletion of *Rac1* leads to substantial reduction of metaplastic process in *CK* model of mPDAC.

For analysis of mPDAC development a cohort of mice was followed for signs of disease progression until death. The clinical course of desease in *CK* mice was described before [22, 23] with an approximat mPDAC incidence of 50-60% and a median survival of 411 days. Notably, loss of Rac1 prevented mPDAC development and resulted in a significantly prolonged survival rate (median survival 529 days; Fig. 9F). Histological endpoint analysis of the $CKR^{fl/fl}$ pancreata revealed mixed phenotypes. The pancreata of most mice contained areas of normal appearing tissue composition with few chronic pancreatitis-like inflammatory infiltrates and low grade PanINs. In two animals we noted high grades of fatty metaplasia (Fig 9G, upper panel). At least four of eight analyzed mice developed lymphoma-like disease (Fig. 9G, middle panel). Further immunohistochemical analysis revealed these lymphomas to be B-cell lymphoma (data not shown). PCR analysis of microdissected tumor tissue showed a weak band of recombined Rac1 most likely due to some pancreatic *Ptf1a*-derived cells within the lymphoma tissue (Fig. 9H). Only one of the eight mice showed higher-grade PanINs (Fig. 9G, lower panel). A PCR of of these

microdissected lesions showed Cre-mediated recombination of the *Rac1* alleles (Fig. 9H). Thus, Rac1 deletion nearly completely ablates PDAC development.

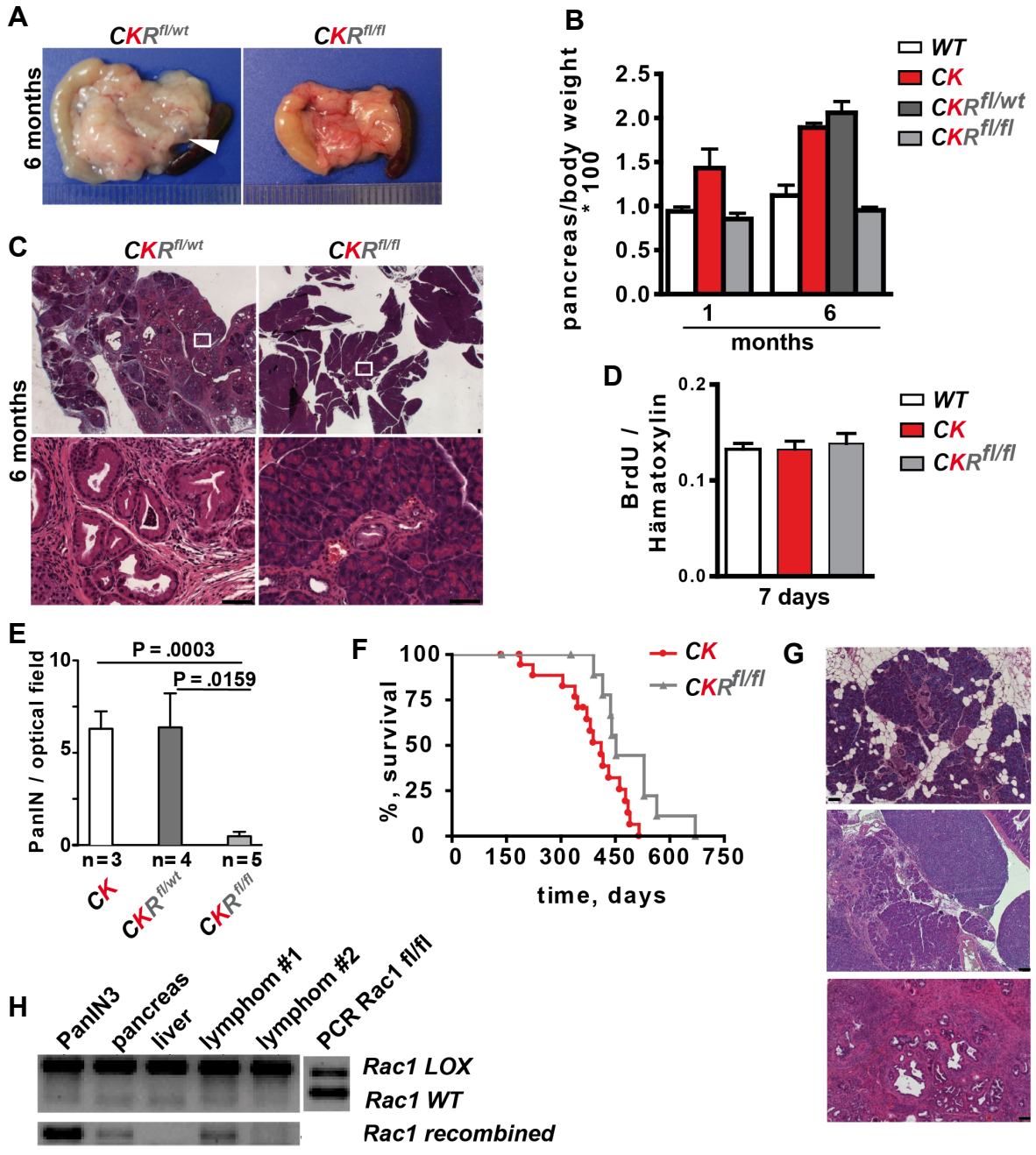

Figure 9: Loss of Rac1 leads to a substantial delay of mPanIN progression and inhibits mPDAC development in CK model. A-E: Deletion of *Rac1* in *CK* model results in substantial inhibition of preneoplastic lesion development. A: Macroscopic photographs of $CKR^{fl/wt}$ versus $CKR^{fl/fl}$ pancreas at the 6-months of age. Note the smaller size and absence of visible cysts (arrow) in $CKR^{fl/fl}$ pancreas. Ruler gap = 1 mm. B: The pancreas/body weight index of $CKR^{fl/fl}$ animals drops to the levels of *WT* littermates in $CKR^{fl/fl}$ model, underlying the absence of metaplastic process (n = 3 - 6/group). C: H&E staining of 6 months-old $CKR^{fl/wt}$ and $CKR^{fl/fl}$ pancreas. The heterozygous animals show disseminated mPanIN/ADM development spread in the whole organ whereas pancreata of homozygous *Rac1* deletion reveal only rare focal PanIN lesions. D: Quantification of proliferation rate in 7 days –old pancreas of *WT*, *CK* and $CKR^{fl/fl}$ animals (n = 3/group). E: Quantification of mPanIN1 in 6-month-old *CK*, $CKR^{fl/wt}$ and $CKR^{fl/fl}$ mice. F: Pancreas-specific *Rac1* deletion significantly prolongs the survival of $CKR^{fl/fl}$ compared to the *CK* cohort. Survival analysis of *CK* (n = 19, median 411 days) versus $CKR^{fl/fl}$ (n = 13, median 529 days) mice. G: Representative examples of end-point histology (H&E staining) of pancreatic tissue from $CKR^{fl/fl}$ mice. Top

panel: normal pancreas with adipose replacement, middle panel: normal pancreas and lymphoma, bottom panel: high grade mPanIN lesions. H: PCR for *Rac1* wt, *Rac1* LOX and *Rac1* recombined from microdissected samples as indicated. Scale bar = 50 µm.

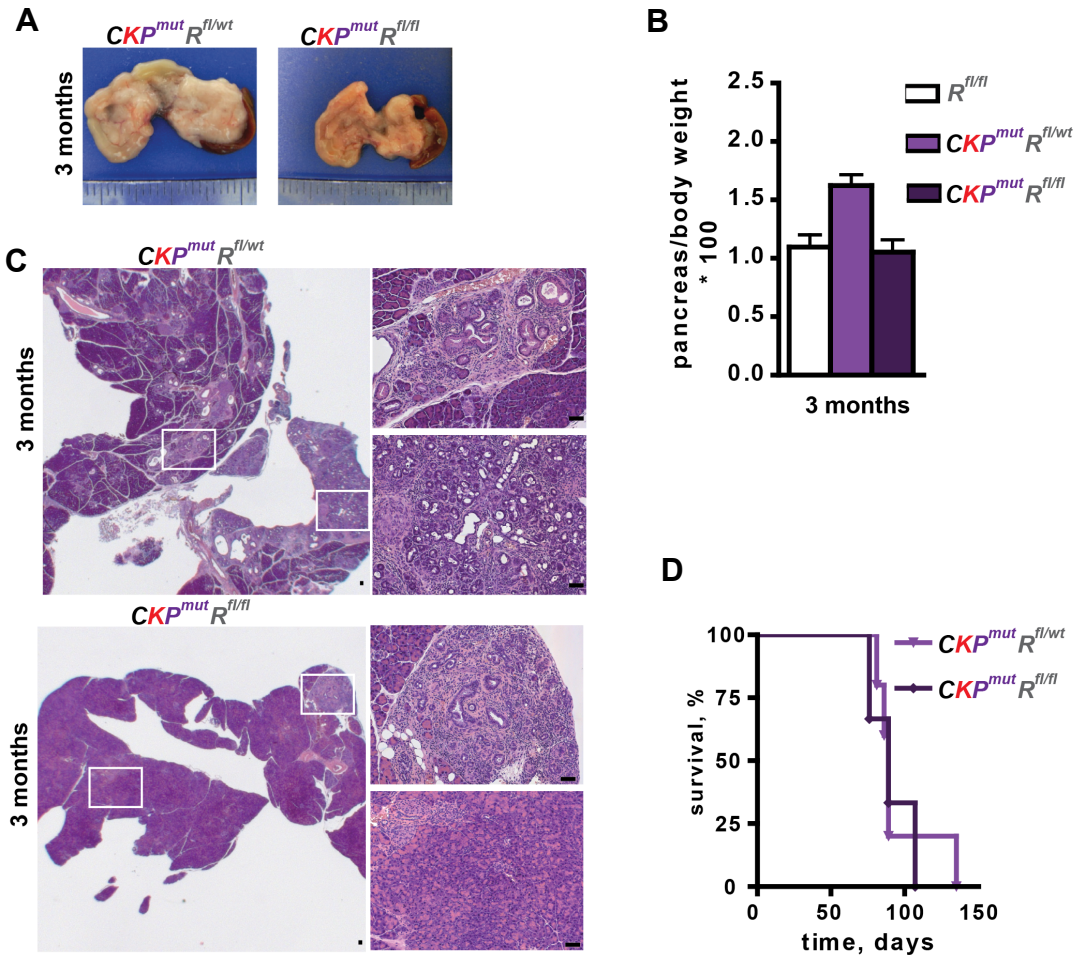

Figure 10: Deletion of *Rac1* inhibits mPanIN development in *CKP*$^{mut/wt}$ model. A-B: At the age of 3 months *CKP*^{mut}*R*$^{fl/fl}$ mice reveal a significantly smaller pancreas compared to *CKP*^{mut}*R*$^{fl/wt}$ animals, as shown by macroscopic photographs (A) and pancreas/body weight index (B). Ruler gap = 1 mm. C: H&E staining of 3 months-old *CKP*^{mut}*R*$^{fl/wt}$ and *CKP*^{mut}*R*$^{fl/fl}$ pancreas clearly shows, that homozygous *Rac1* deletion leads to substantial reduction of mADM/PanIN lesions development. Scale bar = 50 µm. F: Survival analysis of *CKP*^{mut}*R*$^{fl/wt}$ versus *CKP*^{mut}*R*$^{fl/fl}$ (n = 5, n = 3 respectively, median for both groups 89 days) mice. Both cohorts died of other, non tumor-related health reasons at the age of approximately 3 months.

To address the question whether the impairment of mPanIN development following Rac1 deletion was a model specific or a more general mechanism, *CK* mice were crossed to more aggressive *Trp53*$^{wt/LSL-R172H}$(*P*^{mut}) [24] line (for genotype abbreviations see table 3). As expected, pancreas/body weight ratios of these mice also dropped to the *WT* level (Fig. 10A, B). While normal pancreatic tissue was almost completely replaced by mADM/PanIN1-2 in *CKP*^{mut} mice at the age of 3 months, pancreata of the *CKP*^{mut}*R*$^{fl/fl}$ animals showed only very small, single areas with low grade mADM and sparce fibrosis or inflammatory infiltrates (Fig 10C). Histology of later time points in this models were not possible to assess due to early paralysis and short survival time of both *CKP*^{mut}*R*$^{fl/wt}$ and *CKP*^{mut}*R*$^{fl/fl}$ animals (Fig. 10D). Altogether, these results provide substantial evidence that *Rac1* is essential for the development of mADM/PanIN lesions as well as this process surrounding stromal and inflammatory reaction.

3.1.4 Rac1 is necessary for mIPMN and mPDAC development following over activation of EGFR signaling

To address the question whether pancreas specific deletion of *Rac1* influences the development of the second clinically most relevant lesion type mIPMN, *CKTR*$^{fl/fl}$ mice were generated and analyzed (for genotype abbreviations see table 3). As previously reported the *CKT* model mimics human pancreatobiliary IPMNs, the most aggressive papillary lesion type, leading to development of invasive metastatic mPDAC [22]. *CKTR*$^{fl/fl}$ pancreata revealed significantly lower weight at the early age of 7 days, compared to the *CKT* littermates (Fig. 12A, P = 0.28), suggesting impaired development of preneoplastic lesions and stromal reaction. Indeed, tissue staining of mucin 5A, a marker present in all stages of human and murine PanIN and IPMN, was nearly absent in pancreas of *CKTR*$^{fl/fl}$ animals (Fig. 11A, B; P < .001). Although, none of the 13 analyzed *CKTR*$^{fl/fl}$ mice developed typical mIPMNs, in 4 animals we observed acinus cell derived dense lesions shown in Fig. 11C. These lesions were positive for amylase and Pdx1, a pancreatic progenitor cell marker, however always negative for cytokeratin 19 and mucin 5A. This observation suggests that these acinar cells returned to a progenitor state in these lesions, however did not progress to mIPMN of mPanIN.

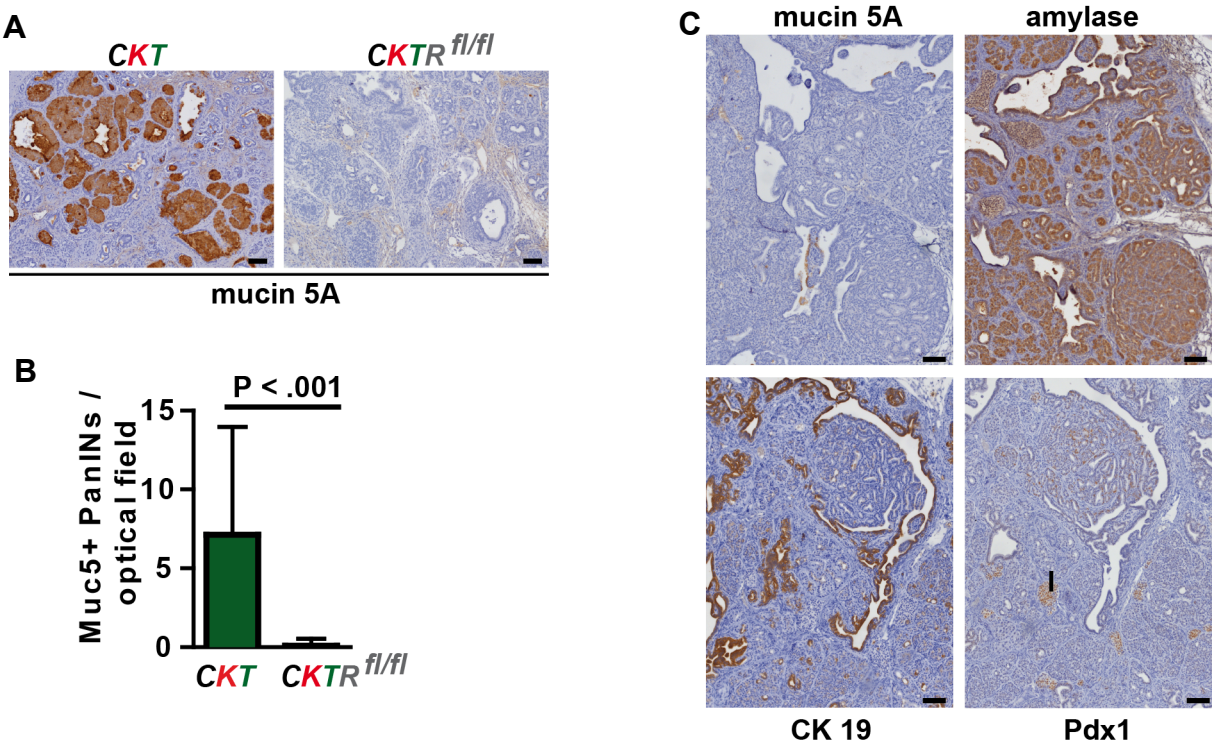

Figure 11: Ablation of *Rac1* inhibits mPanIN and mIPMN development in EGFR-induced *CKT* model of murine pancreatic cancer. Deletion of Rac1 in *CKT* model results in substantial inhibition of preneoplastic lesion development. A: *CKR*$^{fl/fl}$ animals do not develop mucineous lesions in the pancreas. Immunohistologcal analysis of mucin 5A experssion revealed significant reduction of staining in *CKTR*$^{fl/fl}$ pancreas compared to the *CKT* mice. B: Quantification of mPanIN in end stage *CKT* vesus *CKTR*$^{fl/fl}$ mice (P < .001, n = 4 – 7 animals/genotype). C: Representative example of an acinar cell derived lesions observed in pancreas of *CKTR*$^{fl/fl}$ animals (4/13). Immunohistological analysis revealed a strong amylase and Pdx1 staining in contrast to lacking mucin 5A and cytokeratin 19 stainings. Scale bar = 50 µm.

For analysis of mPDAC development, a cohort of mice was followed for signs of disease progression until death. End-stage *CKTR*$^{fl/fl}$ animals developed often cachexia (> 50%), however they did not present with ascites or cysts and bloody infiltrates typical for *CKT* mice (Fig. 12B). The pancreata of *CKTR*$^{fl/fl}$ animals remained significantly smaller than those of *CKT* littermates

beginning at the early stage and persisting to the end-point (Fig. 12A, B). In addition, none of the animals revealed macroscopic metastases to any of the organs, in contrast to freequently seen macroscopic metastases in *CKT* animals (data not shown). Surprisingly, *CKTR*$^{fl/fl}$ animas died significantly earlier than their CKT littermates (Fig. 12C, median survival 157.5 days in *CKTR*$^{fl/fl}$ cohort n = 14, compared to median of survival 303 days in *CKT* cohort n = 17). Histological analysis of the end-point pancreas revealed that all of the 13 animals developed chronic pancreatitis to different extend (Fig. 12D), suggesting it to be the cause of cachexia and dead. Indeed, *CKTR*$^{fl/fl}$ pancreata displayed adipose tissue accumulation (11/13), abundant chronic-pancreatitis-like inflammatory infiltrates (11/13) and acinus cell dysplasia (4/13) (Fig. 12D). Despite the fact that some of the mice had presented with large duct rich regions and rare formation of regressive ducal PanIN3-like structures, without mucineous metaplasia (3/13) (Fig. 12D), none of the animals developed mPDAC. Consequently, these results strongly underline the necessity of Rac1 for the development of mucineous preneoplastic lesions as well as invasive carcinogenesis in Kras- and EGFR-signaling driven mPDAC models.

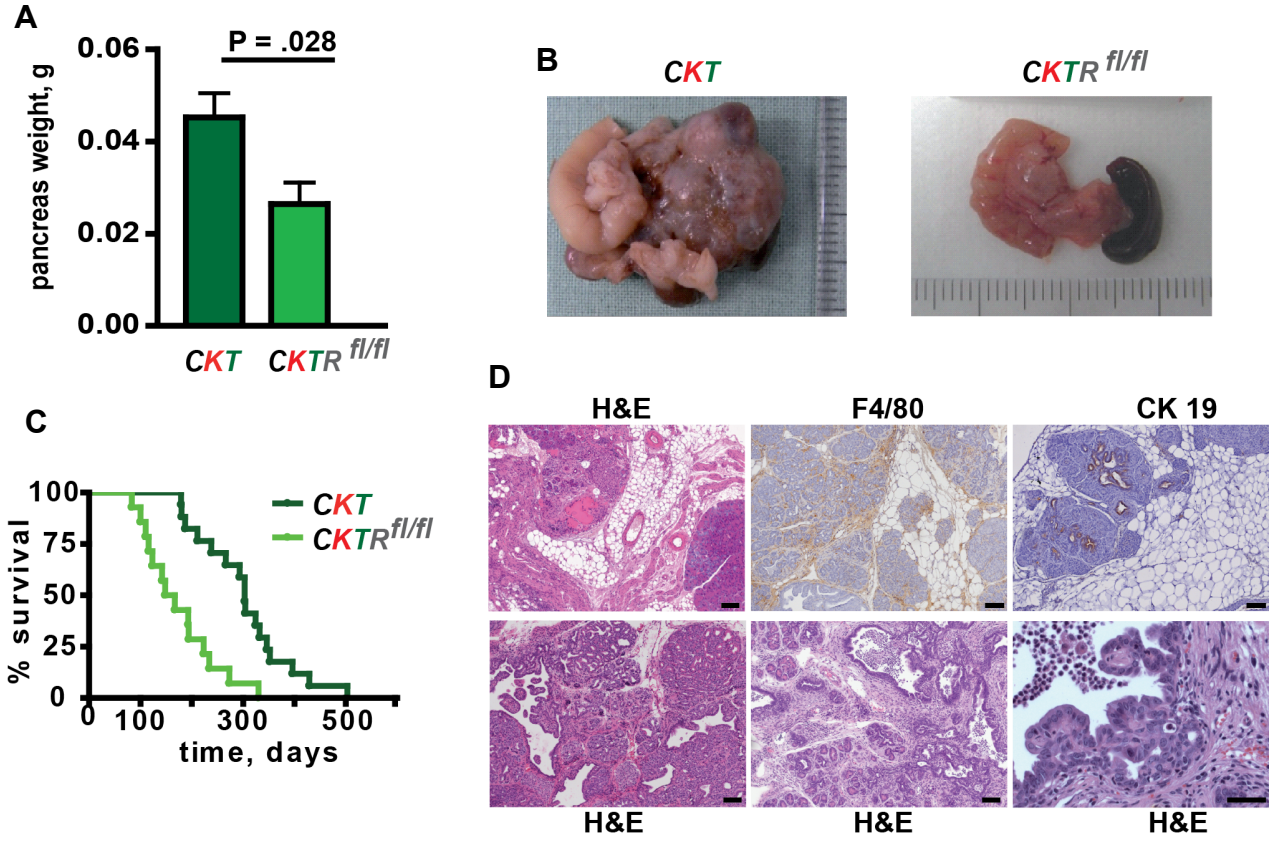

Figure 12: Rac1 is necessary for mPDAC development following overactiivation of Kras and EGFR signaling. Deletion of *Rac1* in *CKT* model leads to an ablation of mPDAC development however induces chronic pancreatitis accompanied by shortened survival. A: The pancreas/body weight index of 7 days-old *CKTR*$^{fl/fl}$ animals is significantly smaller than that of littermates in *CKT* model, underlying the absence of metaplastic process (n = 5 - 7/group). B: End-stage analysis of *CKTR*$^{fl/fl}$ pancreas displays a notably smaller organ as well as an absence of cysts or bloody infiltrates compared to CKT animals, as shown by macroscopic photographs. Ruler gap = 1 mm. C: Pancreas-specific *Rac1* deletion significantly reduces the survival of *CKTR*$^{fl/fl}$ compared to the *CKT* cohort. Survival analysis of *CKT* (n = 17, median 303 days) versus *CKTR*$^{fl/fl}$ (n = 14, median 157.5 days) mice (P < .0001). D: Representative examples of end-point histology of pancreatic tissue from *CKTR*$^{fl/fl}$ mice. Top panel: chronic pancreatitis with adipose tissue accumulation. Upper panel: H&E staining (left), inflammatory infiltrates verified by F4/80 staining (middle) and mADM shown by CK19 staining (right). Bottom panel: abundant chronic-pancreatitis-like inflammatory infiltrates (H&E, left), acinus cell dysplasia (H&E, middle) and regressive ducal PanIN3-like structures (H&E, right). Scale bar = 50 µm.

3.1.5 Deletion of Rac1 has no impact on the major EGFR-related pathways

To elucidate the underlying mechanisms of Rac1 activation during pancreatic carcinogenesis, proliferation rate in mPanIN lesions was compared in *CK* versus $CKR^{fl/fl}$ as well as in $CKP^{mut}R^{fl/wt}$ versus $CKP^{mut}R^{fl/fl}$ animals. However no differences were detected, revealing similar proliferative capacity in the developed lesions of all 4 genotypes (Fig. 13A, B). Because lack of *Rac1* in pancreatic tissue may be compensated by highly similar *Rac2* or *Rac3*, their expression was analyzed via qRT-PCR in 4 weeks old $CKR^{fl/fl}$ as shown in figure 13C. Here only *Rac1* was up regulated compared to the *WT* pancreas tissue, reflecting abnormal *Rac1* expression in preneoplastic lesions and surrounding stroma. In addition, activity of Rac1 closely related protein cdc42 was also not changed, as detected by GTPase-based immunoblotting assay and shown in figure 14A.

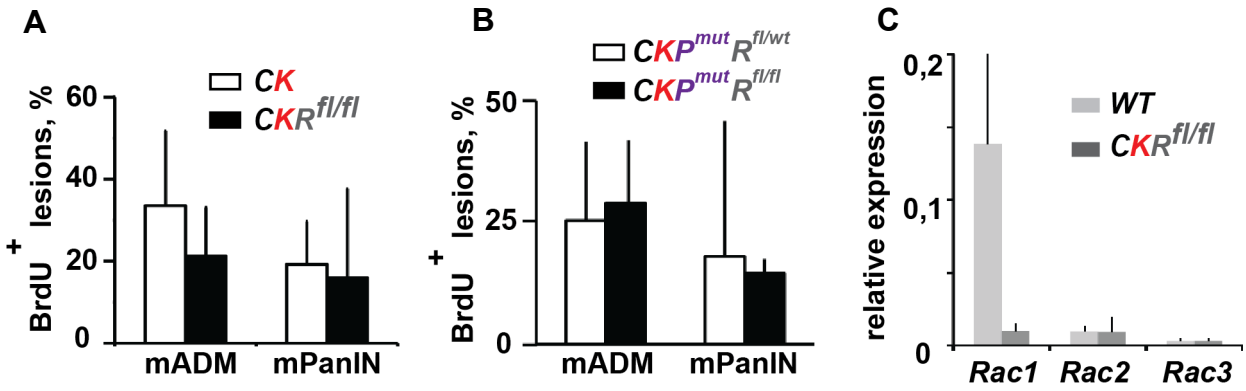

Figure 13: Deletion of *Rac1* has no impact on proliferation in mADM and mPanIN. A, B: Proliferation analysis of mADM and mPanIN lesions in pancreata of 6 months-old *CK* versus $CKR^{fl/fl}$ (A) as well as 3 months-old CKP^{mut} versus $CKP^{mut}R^{fl/fl}$ (B) animals (n = 3/genotype). C: Expression of *Rac1, 2* and *3* by qRT-PCR in 6 months old mice of indicated phenotype. No *Rac1* substitution by *Rac2/3* is observed.

Furthermore, the status of the main oncogenic pathways downstream of EGFR was assessed in pancreatic tissue samples of 4 weeks-old *CK* versus $CKR^{fl/fl}$ mice using Western blot analyses (Fig. 14B). EGFR-signaling pathways were unaffected at the beginning of the neoplastic process. Morover immunohistological staining of P-Stat3, P-Mek and P-Erk also revealed no changes in the later developed mPanIN lesions as shown in figure 14C. In addition, a possible involvement of the centroacinar compartment (CAC) into the impaired development of pancreatic lesions following *Rac1* deletion were analyzed in pancreatic samples of several time points by immunohistochemical staining of Pdx1, Hes1 and Notch2 (data not shown). None of the CAC markers displayed different expression between *WT* and *Rac1* deleted pancreata in either *Kras* wildtype or mutated (G12D) setting. Further IHC and qRT-PCR-based analysis of Notch and Hh pathway activation at 4 weeks was also not different between the genotypes (Fig. 14D), suggesting that Rac1 is not a major regulator of these pathways in our model.

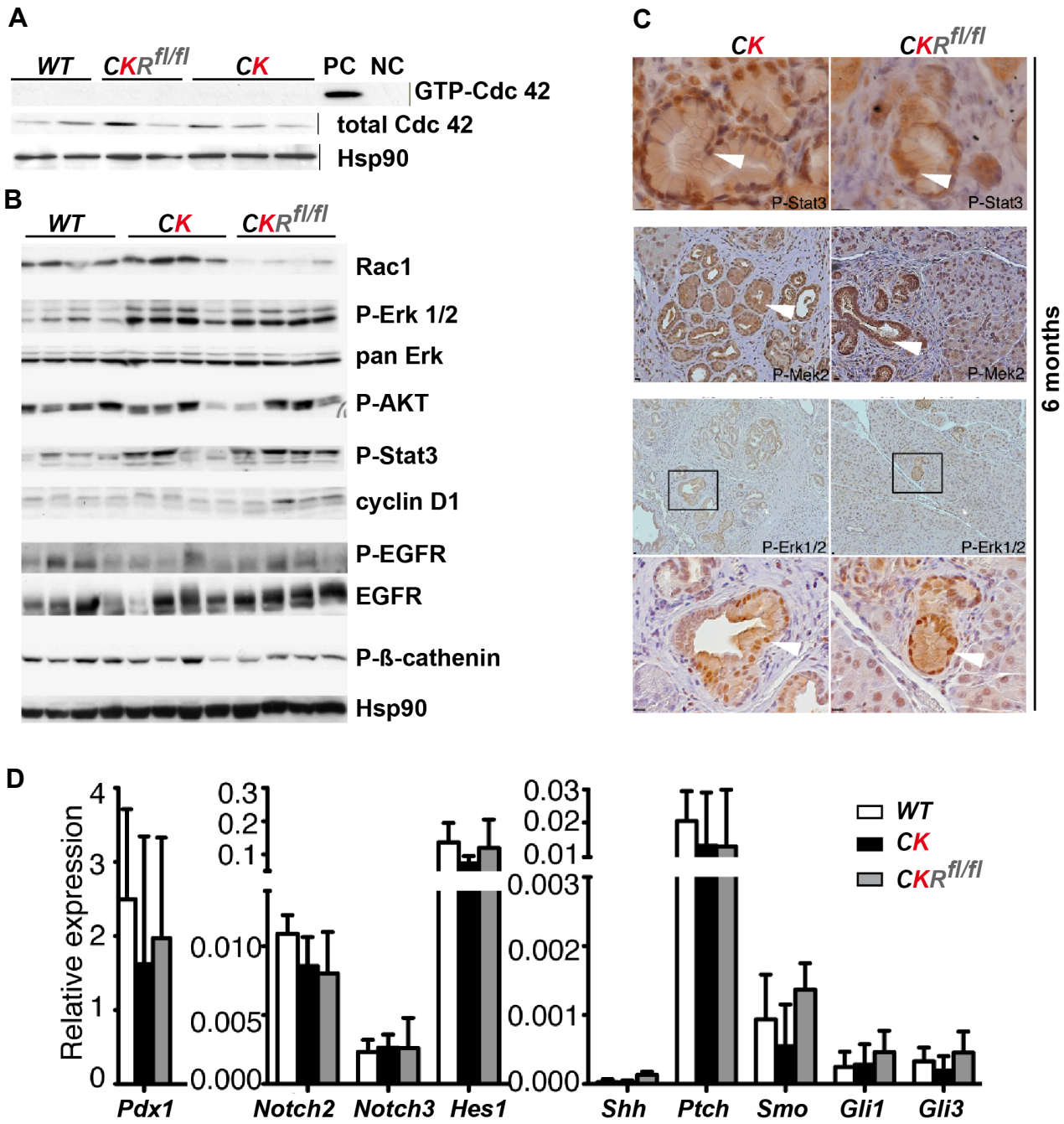

Figure 14: Deletion of *Rac1* has no impact on central RAS/EGFR- and Notch-dependent effector pathways. A: Cdc42 pull down assay of pancreatic whole-tissue lysates in 4 weeks-old pancreata of indicated phenotype. Hsp90 serves as loading control. B: Immunoblot analyses of the main RAS/EGFR pathway effectors in 4-week-old whole-pancreatic lysates reveal no significant changes. Hsp90 serves as loading control. C: Immunohistochemical analysis of exocrine pancreas and mPanINs from *CK* versus *CKR*$^{fl/fl}$ animals shows a comparable expression pattern of P-Stat3, P-Mek and P-Erk1/2 between the genotypes. D: Relative mRNA expression of *Pdx1*, *Notch*, *Hes* and *Hedgehog* signaling genes in the pancreata of 1-month-old *CK* versus *CKR*$^{fl/fl}$ animals. No significant differences between the genotypes are notable.

3.1.6 Rac1 is required for the initiation of acinar to ductal metaplasia and this process accompanied actin rearrangements

Since deletion of *Rac1* had no impact on the major PDAC-related pathways, it was hypothesized that the impaired mADM/mPanIN development in these models may occur due to the reduced cellular plasticity of *Rac1* depleted acini. Indeed, Bi *at al.* reported that Rac1 is strongly involved

in acinar morphological changes, F-actin redistribution, and amylase secretion upon CCK treatment *in vitro* [67]. To explore this hypothesis *in vivo*, a well-established model of cerulein-induced acute pancreatitis was employed [41]. Thus, two cohorts consisting of *WT* and *CR*$^{fl/fl}$ littermates were injected with cerulein over 2 days as described previously [41] and analyzed 24 and 72 hours thereafter. Deletion of *Rac1* significantly reduced development of CK19 positive mADM lesions during acute pancreatitis (Fig. 15A-D). Although the amount of ADM lesions at 72 hours failed to show significant differences in *CR*$^{fl/fl}$ compared with *WT* animals, a trend in favor of *CR*$^{fl/fl}$ pancreata was clearly visible (Fig. 15C, D).

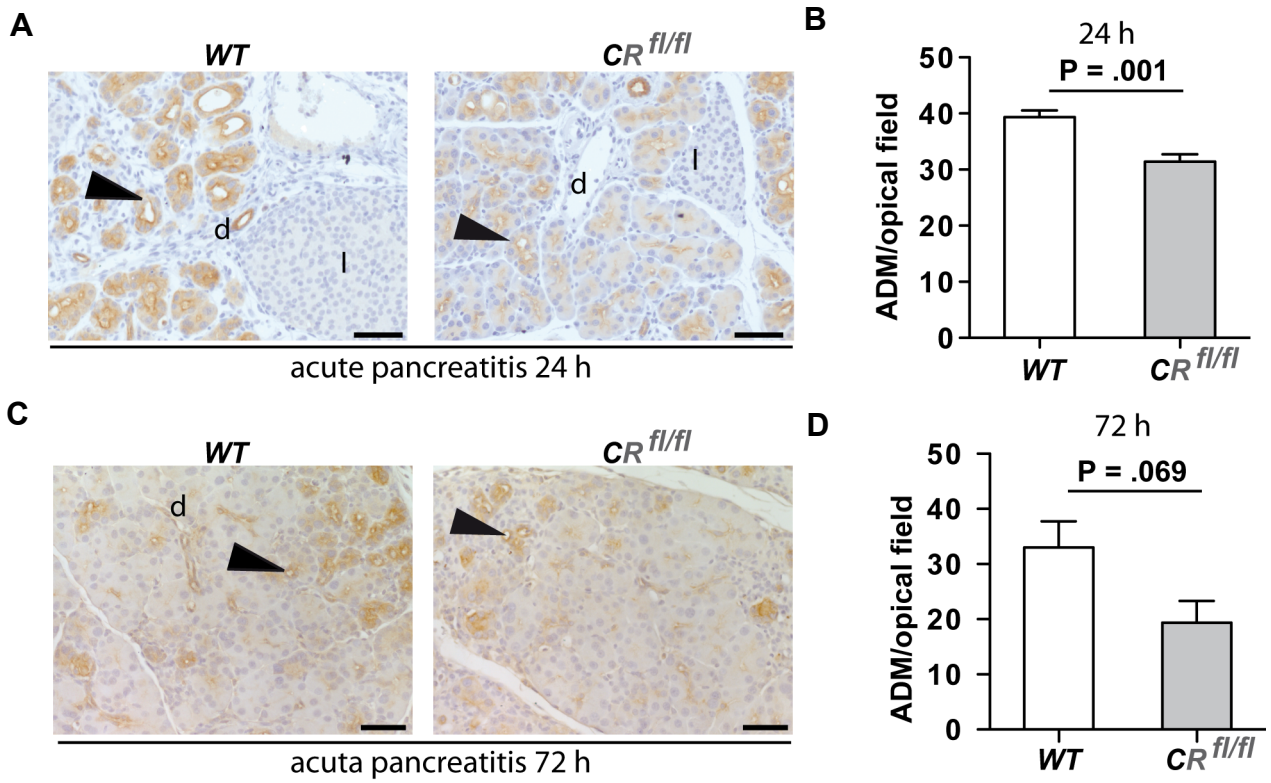

Figure 15: Loss of *Rac1* reduces mADM in cerulein-induced acute pancreatitis. A-D: Deletion of Rac1 reduces the development of mADM lesions during cerulein-induced acute pancreatitis in *CR*$^{fl/fl}$ mice compared with WT. A, C: CK19 staining. Arrowheads show CK19-positive mADM lesions (d, duct; I, islet). Scale bar = 50 µm. B, D: Quantification of CK19-positive ADM lesions in WT versus *CR*$^{fl/fl}$ mice (n = 4-6/group).

Importantly, the F-actin redistribution in mADM underlined the hypothesis (Fig. 16). In oncogenic setting as shown in figure 16A on samples of 6 months-old *CK* animals both F-actin and CK19 were translocated to the basal membrane during mADM in addition to the original apical location. A similar effect was observed in the cerulein-induced pancreatitis model, where F-actin was clearly located apically and redistributed basolaterally following 24 hours induction of pancreatitis in *WT* acini (Fig. 16B). This process was reduced in *CR*$^{fl/fl}$ mice, possibly explaining the impairment of mADM formation. Thus, a model for F-actin redistribution during ADM was proposed. The apical-located actin filaments protrude to the basolateral side and concentrate at both sides of the metaplastic transdifferentiating cells, a sign for loss of cell polarity (Fig. 16C). Consequently, Rac1 is an important determinant of mADM induction in both an oncogenic and inflammatory setting.

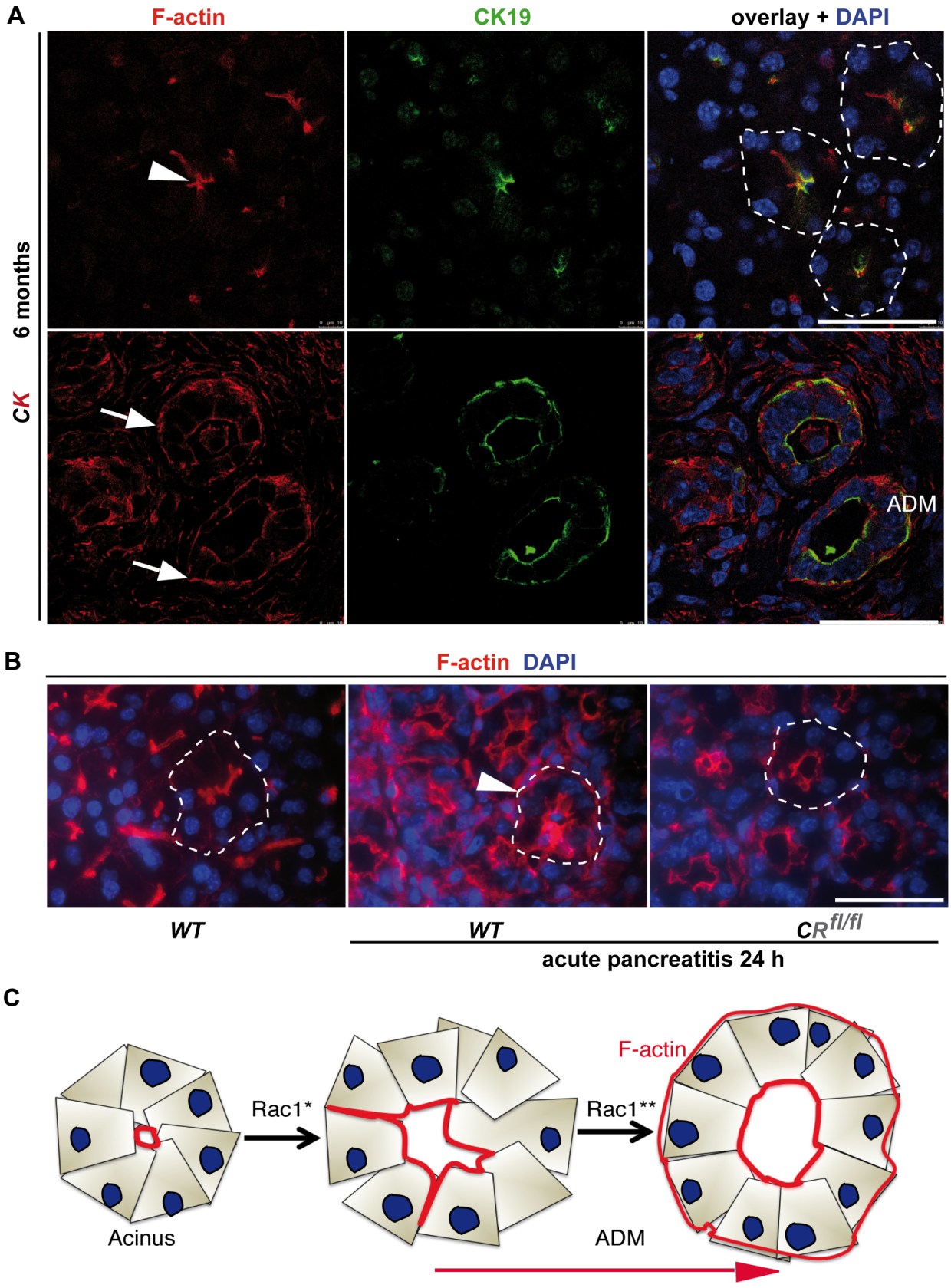

Figure 16: Murine acino-ductal metaplasia is associated with actin reorganization. Localization and redistribution of F-actin and CK19 during mADM in *Kras*^{G12D}- and cerulein-induced pancreata. Immunofluorescence single/double staining on pancreatic cryosections. Dashed lines visualize acini as example. Scale bar = 50 µm. A: F-actin is clearly apically located (white arrow, upper panel) in normal acini and shows basolateral localization (white arrows, lower panel) in mADM lesions (confocal analysis). B: F-actin is apically located in *WT* acini (left panel) and redistributes basolaterally following pancreatitis induction (white arrowhead). This process is considerably reduced in *CR*$^{fl/fl}$ mice. C: Model for F-actin (red

line) redistribution during mADM. The apical localized actin filaments redistribute to the basolateral side and concentrate at both sides of the metaplastic transdifferentiating cells. This process is supported by Rac1 activation in pancreatic tissue.

3.1.7 ADM of murine acinar pancreatic explants is highly Rac1 dependent

To further explore the above-made hypothesis an *in vitro* study with acinar pancreatic epithelial explants was performed. It was shown that acinar pancreatic explants cultured in collagen matrix can differentiate to ductal structures after TGFa stimulation thereby mimicking *in vivo* acinar-to-ductal metaplasia [36, 153]. Therefore, this method was used to assess the function of Rac1 in the exocrine metaplastic conversion upon TGFa stimulation. Freshly harvested explants from *WT* and $CR^{fl/fl}$ littermates consisted of acinar cells cluster expressing amylase and were morphologically indistinguishable (Fig. 17A, B). Immunofluorescence staining of acinar epithelial explants from *WT* and *CK* mice showed a weak Rac1 expression after isolation. However upon 1 hour of TGFa treatment Rac1 expression strongly increased [152]. Treated with 50 ng/mL TGFa for 5 days ~74.5% ± 22.4% (n = 3) of the *WT* acini acquired duct-like phenotype, characterized by cystic structures lined by simple epithelia and expressing the duct cell marker CK19 (Fig. 17B, D). In contrast, only 26% ± 36.8% (n = 2) of acinar explants from $CR^{fl/fl}$ animals transdifferentiated to ducts upon TGFa treatment (Fig. 17B, D). Moreover, the duct-like structures of $CR^{fl/fl}$ explants were smaller and lined by several cell layers. The less abundant CK19-expressing cells were mostly surrounded by cell clusters with retained acinar phenotype (Fig. 17B), suggesting incomplete transdifferentiation.

Compared to *WT*, pancreatic acinar explants from 4-week-old *CK* animals transdifferentiated spontaneously (88.1 ± 22.7%; n = 4) due to the presence of $Kras^{G12D}$ activation. TGFα treatment enhanced the metaplastic capacity of these acini to 100% conversion (Fig. 17E), consistent with the accelerated carcinogenesis in the *CKT* model [22]. Moreover, the *CK*-derived duct-like cysts displayed a distinct enlargement, complete loss of exocrine marker expression and strong CK19 staining (Fig. 17C). The explants from $CKR^{fl/fl}$ mice revealed only rare duct-like structures of smaller size (Fig. 17C). Ablation of pancreatic *Rac1* in CK acinar cells led to a substantial impairment of the metaplastic process: only 9.2 ± 12.9% (n = 3) of acini transdifferentiated spontaneously to duct-like structures after 3 days in collagen cultures and exhibited even greater impairment of metaplastic capacity upon TGFa treatment (Fig. 17E). These observations indicate that $Kras^{G12D}$- or EGFR-activated signaling was sufficient to initiate the ADM process, shown by CK19 expression of Rac1-lacking explants. However, the morphological changes, necessary for formation of duct-like structures were strongly inhibited in the absence of *Rac1*. Taken together, loss of Rac1 is sufficient to prevent the full conversion of acinar cells to a metaplastic ductal epithelium.

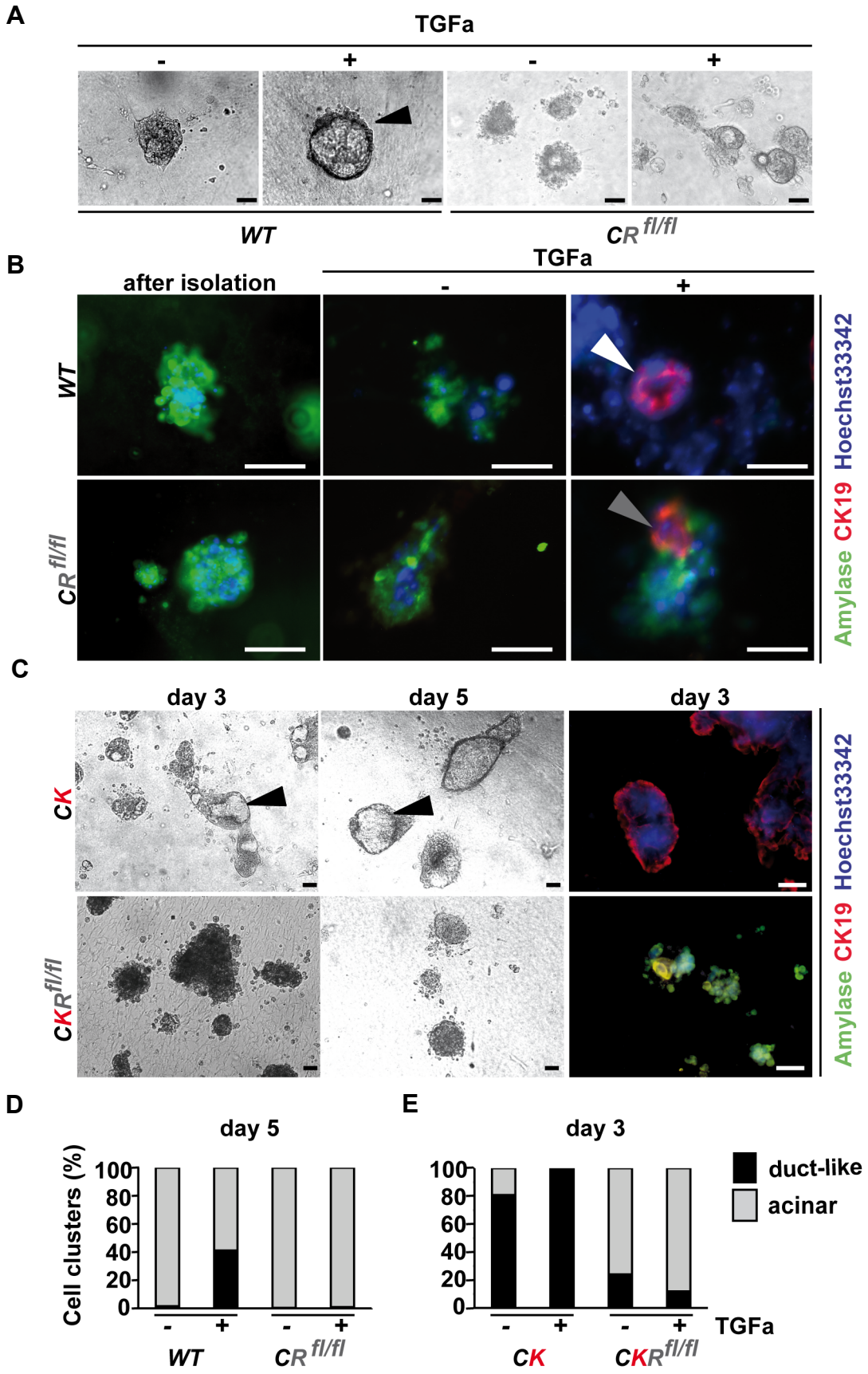

Figure 17: mADM in primary murine acinar epithelial explants is Rac1 dependent. Murine pancreatic acinar epithelial explants undergo transdifferentiation to ductal structures in collagen cultures under TGFa treatment (A) or spontaneously due to the presence of oncogenic *Kras*^{G12D} (C, middle panel). A, C: Phase contrast images and B, C: immunofluorescence staining for amylase and CK19. B: After isolation, acinar cells express amylase independently of the genotype *WT* explants convert to duct-like structures positive

for CK19 (white arrowhead) when cultured for 5 days with recombinant human TGFa. Acinar epithelial explants of mice lacking *Rac1* show no or aberrant duct-like morphology and retain amylase expression (gray arrowhead). C: Acinar explants of *CK* mice convert spontaneously to duct-like structures already at day 3 and express only CK19 (top, arrowheads). In contrast, explants from $CKR^{fl/fl}$ mice are significantly impaired in their ability to form duct-like structures. All nuclei are stained with Hoechst 33342. Scale bar = 50 µm. D, E: Quantification of acinar explants from *WT,* $CR^{fl/fl}$, *CK*, or $CKR^{fl/fl}$ mice as described previously (one representative experiment). The difference in the amount of duct-like structures is significant in D (*WT*/$CR^{fl/fl}$, P = .001; *WT*/$CR^{fl/fl}$ wt TGFa, P = .0002) and in E (*CK*/$CKR^{fl/fl}$, P =.01; *CK*/$CKR^{fl/fl}$ wt TGFa, P = .0006).

3.1.8 Ablation of *Rac1* substantially reduces *Kras*- induced inflammatory response in the pancreas

Several studies report that PanIN initiation and development is associated with prominent leukocyte infiltration and requires this oncogenic inflammation for progression to invasive PDAC [30, 40, 45]. Since 6 months-old $CKR^{fl/fl}$ pancreata displayed very little inflammatory infiltrates surrounding the few mPanINs (Fig. 9C, 19C), the neoplasia associated inflammatory response was analyzed in *CK* and $CKR^{fl/fl}$ models. Thereby, the time point of 1 month was choosen, because the preneoplastic changes in *CK* mice are just about to appear at this period and analyzed tissue would be approximately similar exept for the different inflammatory signals. As expected, pancreata of 1 month-old *CK* mice revealed some CK19 positive mIPMN/PanIN lesions whereas $CKR^{fl/fl}$ exhibited very rare if any mataplastic changes as shown in figure 18A and verified by quantification of CK19 positive lesions in figure 18B.

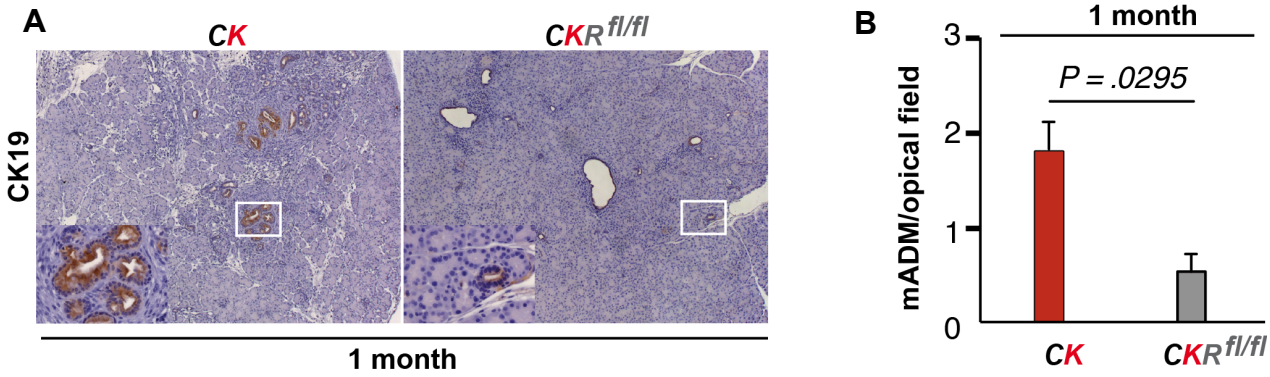

Figure 18: Pancreas-specific deletion of *Rac1* inhibits early stage mADM/PanIN development in the CK model. Deletion of Rac1 impairs the development of metaplastic acini in $CKR^{fl/fl}$ pancreata compared to CK model. A: CK19 staining of pancreatic tissue from 4-week-old animals of CK mice shows focal positive ADM lesions (insert). In contrast, pancreata of $CKR^{fl/fl}$ mice (right panel) reveal only very rare single mADM lesions. Scale bar = 50 µm. B: Quantification of CK19 positive mADM lesions in pancreata of indicated genotype (n = 3/group).

The pancreas of $CKR^{fl/fl}$ animals revealed clearly reduced infiltration of leucocytes ($CD45^{wt}$), macrophages ($F4/80^{wt}$) and cancer associated fibroblasts (CAFs, $a\text{-}sma^{wt}$) around metaplastic acini in comparison to *CK* littermates (Fig. 19A-C). Furthermore, N. Erez and colleagues identified recently a pro-inflammatory gene signature responsible for tumor-promoting behavior of cancer associated activated fibroblasts (CAFs) isolated from pancreatic, skin, breast and cervical cancers [58]. Thus mRNA-expression of 10 tumor associated proimflammatory cytokines and chemokines was tested by quantitative RT-PCR analysis from whole tissue mRNA of 1 month old pancreata of *CK* and $CKR^{fl/fl}$ animals (Fig. 19D). As expected, the deletion of *Rac1* in the *CK* mouse model led to a profound reduction of the inflammatory gene expression, in many cases

down to the level of the *WT* (data not shown). Thus, loss of Rac1 considerably reduced the inflammatory response to the early development of preneoplastic lesions, probably due to the substantial impairment of acinar cells to undergo metaplastic changes

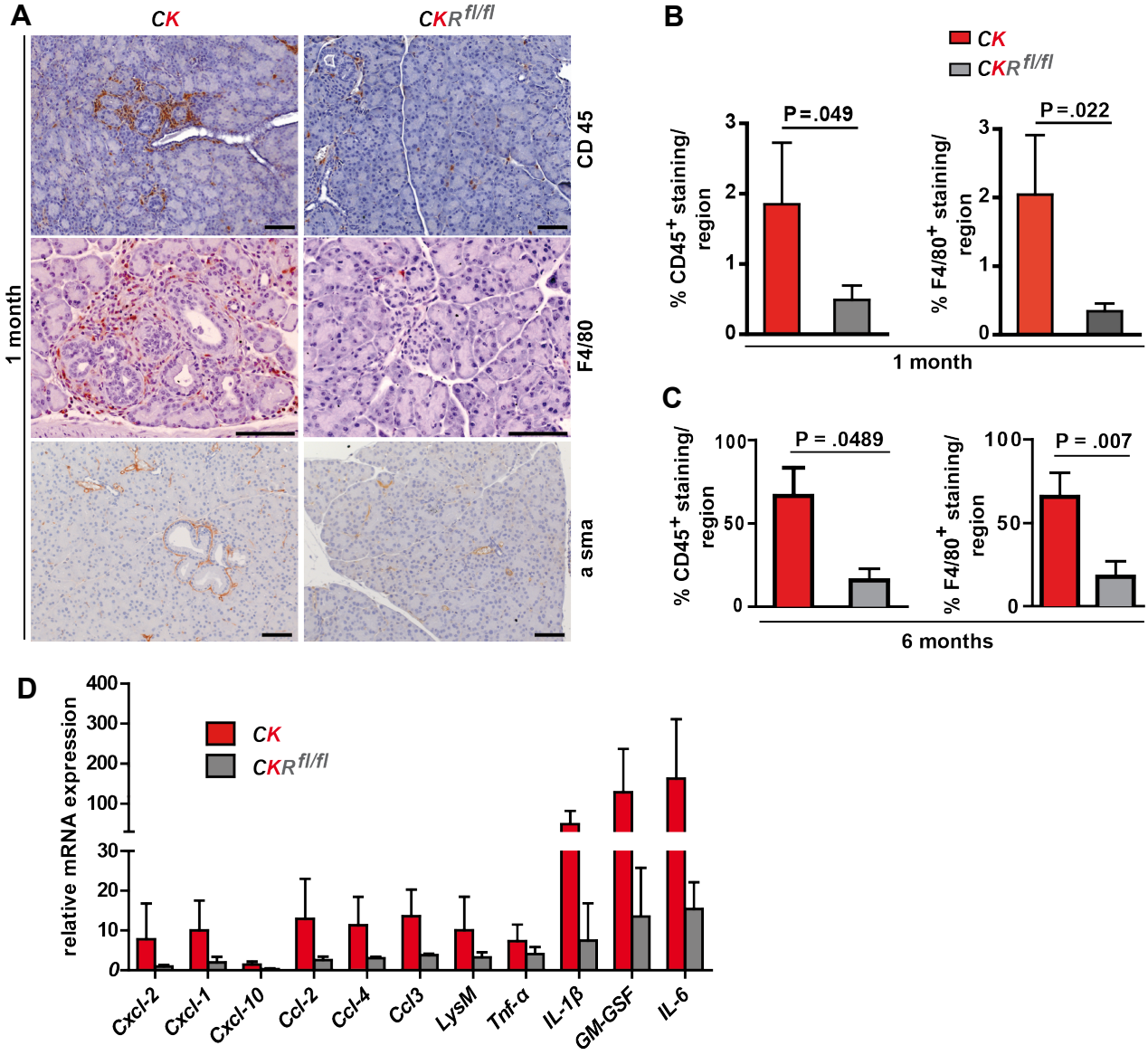

Figure 19: Pancreas specific deletion of *Rac1* causes pronounced reduction of Kras-driven infiltration of inflammatory cells. Deletion of *Rac1* impairs infiltration of myeloid cells and CAFs in *CKR*$^{fl/fl}$ pancreas compared to *CK* model. A: Immuno-histological analysis of pancreata from 1 month-old *CK* and *CKR*$^{fl/fl}$ animals. The pancreatic tissue of *CK* littermates reveals a profound infiltration of leucocytes (CD45^{+}), macrophages (F4/80^{+}) and CAFs (a-sma+) into the metaplastic areas. Scale bar = 50 µm. B, C: Quantitative analysis of leucocytes infiltration in 1 month- (B) and 6 months-old (C) pancreas of indicated genotype (n = 4/group). E: Gene expression analyses of neoplasia-associated cytokines and chemokines revealed that loss of *Rac1* leads to a substantial reduction of inflammatory process. Quantitative RT-PCR analysis of whole-tissue mRNA isolated from pancreas of 1 month-old animals of indicated phenotype. (n = 4/group).

3.1.9 Rac1 is an inflammatory response modulator in caerulein-induced acute pancreatitis

Next, the role of Rac1 in the modulation of the immune response accompanying mADM was explored in non-oncogenic but inflammatory setting. To do so, the described above *in vivo* model of chemically induced acute pancreatitis was applied in two cohorts consisting of *WT* and *CR*$^{fl/fl}$

littermates. Histological appearance of the pancreas was analyzed at the time points of 0, 24 and 72 hours after the last caerulein injection. As shown in Fig. 20A (upper panel, 0h) caerulein induced a substantial damage in the *WT* pancreas. Thereby, loss of acinar cells, prominent edema regions and leucocyte infiltrates were observed as proven by abundant $CD45^{wt}$ staining and its quantification (Fig. 20B; 0h). Surprisingly, $CR^{fl/fl}$ animals revealed significantly lower pancreatic injury, as well as clearly reduced inflammatory response (Fig. 20A, B; 0h). Importantly, concentration of amylase and lipase enzymes, clinically used read parameters for acinar cell damage, were significantly lower in blood sera $CR^{fl/fl}$ mice compared to *WT* samples (Fig. 21). These observations suggest an inflammation-promoting role of Rac1 in acute pancreatitis.

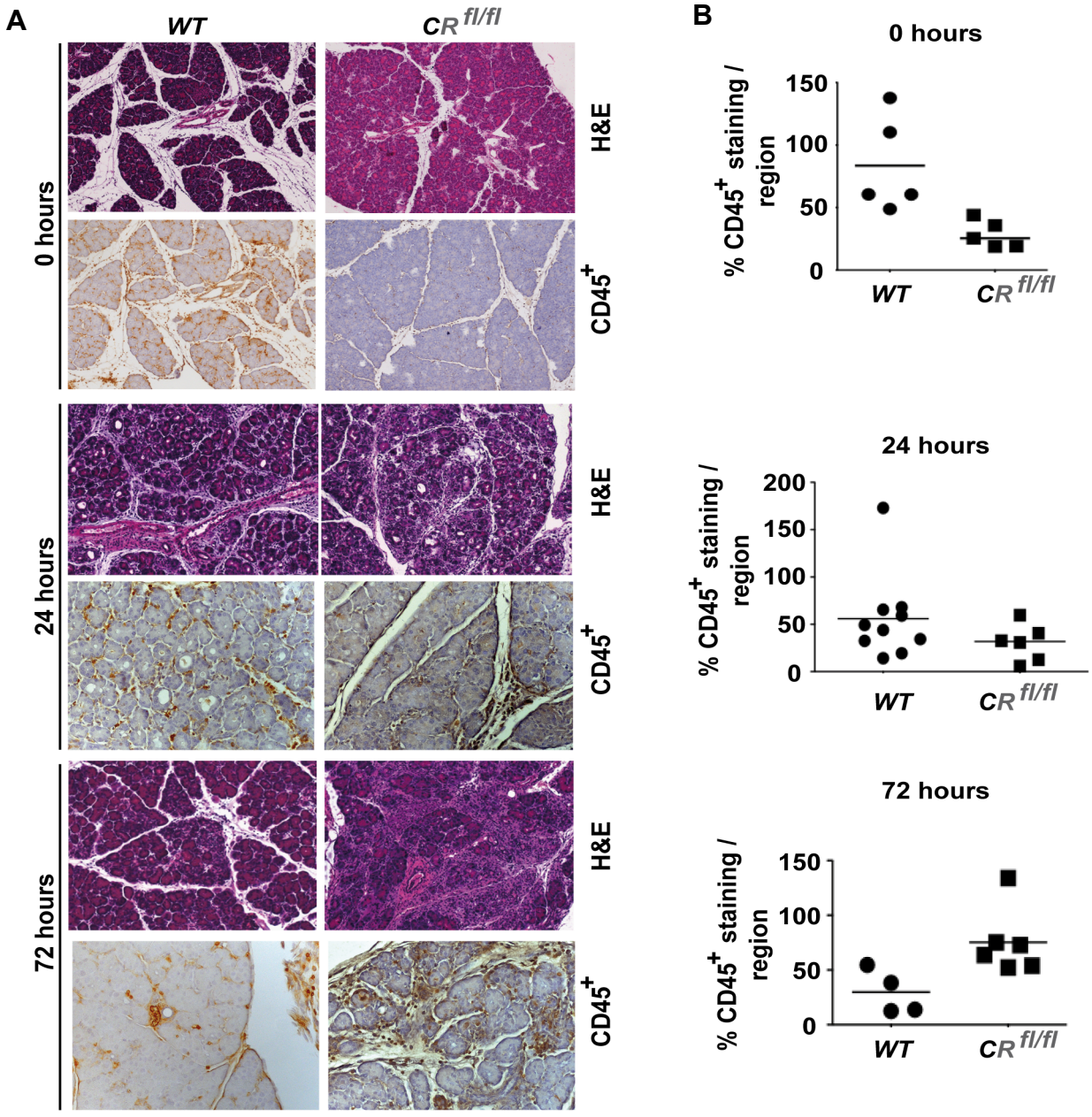

Figure 20: Rac1 is an inflammatory modulator in caerulein-induced acute pancreatitis. Deletion of *Rac1* in chemically-induced acute pancreatitis leads to a significant delay of inflammatory response $CR^{fl/fl}$ mice compared with *WT* animals. A: H&E and CD45 staining of pancreatic samples of indicated time after the last injection and phenotype. Scale bar = 50 µm. B: Quantification of CD45-positive staining in *WT* versus $CR^{fl/fl}$ mice (n = 4-6/group).

This variation in inflammatory response balanced out at the time point of 24 hours, as well as concentration of pancreatic enzymes found in blood sera of the animals (Fig. 20, 21; 24h). However $CR^{fl/fl}$ littermates still revealed a lower grade of inflammatory response in the pancreas as shown in figure 20. Consistent with this finding a significantly higher amount of mADM was found in WT pancreata as described in chapter 3.1.6 (Fig 15). Surprisingly, pancreas regeneration in both groups revealed significant differences: While *WT* pancreata healed, as proven by almost normal histology and low $CD45^{wt}$ staining, inflammatory response in $CR^{fl/fl}$ animals dramatically increased revealing abundant leukocyte infiltration in both H&E and $CD45^{wt}$ staining (Fig. 20; 72h). Taken together, these observations strongly suggest, that Rac1 plays a very important role in acinar damage and inflammatory response modulation following chemically induced pancreatitis.

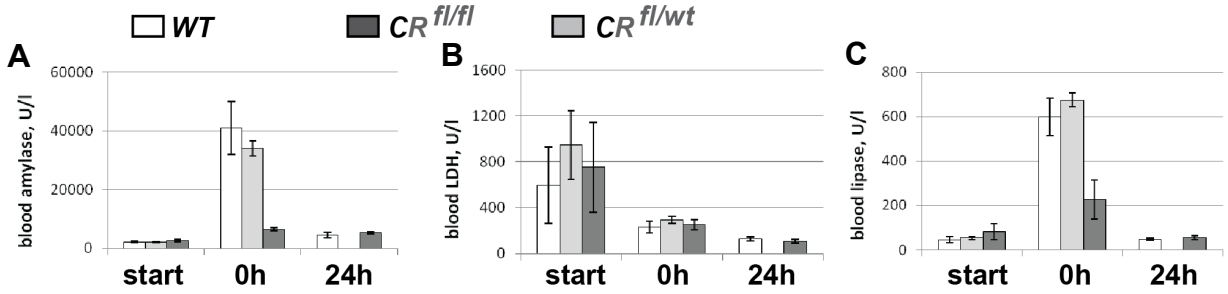

Figure 21: Acinar cell damage during cerulein-induced acute pancreatitis is regulated by Rac1. Deletion of Rac1 reduces acinar cells damage during cerulein-induced acute pancreatitis. Levels of amylase (A), LDH (D) and lipase (C) were measured in blood sera of cerulein-treated animals at the timepoint of 0 and 24 hours after the last injection.

3.2 Testing Rac1 inhibitors for mPDAC treatment

Based on the findings presented in the chapter 3.1 it was hypothesized, that depletion or inactivation of Rac1 may inhibit pancreatic tumor growth. Subsequently, two available Rac1 inhibitors were tested in a subset of human and murine pancreatic cancer cell lines.

3.2.1 Blockage of Rac1 activity by NSC23766 in combination with Gemcitabine inhibited mPDAC but not normal epithelial cell growth in a dose dependent manner.

For the evaluation of known and new therapeutic agents and their combinations primary mPDAC cell lines were isolated from a panel of more than 20 murine tumors. Using tetrazolium salt (MTT) assay as a readout system for cell viability, 12 treatment conditions and their combination with Gemcitabine were tested according to in the literature-established protocols. In summary, five main groups of therapeutics were evaluated: cytostatics (Gemcitabine, etoposide), tyrosine kinase inhibitors (erlotinig, gefitinib and cetuximab), PI3K/MAPK inhibitors (P6, LY29402, PD98059) and γ-secretase inhibitors (DAPT, DBZ and L685). One of the tested cell lines is shown in figure 22A as a representative example of therapy efficacy analysis using an established *in vitro* platform. Gemcitabine treatment (0.01 µM) caused 24.5% reduction of cell viability compared to the vehicle treatment. Only two inhibitors showed better cell growth inhibition alone at the tested concentrations compared to the vehicle: the Rac1 inhibitor NSC23766 (43,4%, 50 µM) followed by γ-secretase inhibitor L685 (34,3%, 1µM). Several combinations revealed synergism with Gemcitabine: Relative inhibition of cell viability for Gemcitabine in combinations with etoposide 37%, dasatinib 39%, P6 37% and LY29402 44% were higher than the single therapy. Nevertheless, Rac1 activity inhibition by NSC23766 demonstrated the most prominent tumor cell growth inhibition: 43% alone and 64% in combination with Gemcitabine compared to the vehicle.

Next, the selectivity of NSC23766 for Rac1 activation inhibition was tested using Rac1 pull down assay. Consistent with the previous reports [104, 105] NSC23766 robustly inhibited Rac1 activation upon FGF without any effect on closely related cdc42 as shown in Fig. 22B. Following, NSC23766 was tested in a subset of human (MIaPaCa2, Pank1) and murine (6 *CK* and 10 *CKT* and 6 $CKP^{fl/fl}$ cell lines) pancreatic cancer cell lines as well as in immortalized fibroblasts (NIH3T3). Treatment with NSC23766 decreased cell viability in a dose-dependant manner in all tumor cell line tested (Fig. 22C, data not shown). In contrast, NSC23766 had little effect on the survival of normal NIH3T3 fibroblasts. Moreover, tested in soft agar assay NSC23766 revealed a substantial inhibition of colony formation and therefore anchorage independent growth (Fig. 22D). Thus, NSC23766 is a potent inhibitor of Rac1activity that substantially hinders murine and human pancreatic tumor cell growth in 2D and 3D culture.

In addition, Rac1 activity inhibition revealed striking inhibitory impact especially in Gemcitabine resistant cells. As shown in figure 22E already single Rac1 activity inhibition by NSC23766 reduces cell viability to a greater level as Gemcitabine alone. In combination, NSC23766 caused a strong dose-dependent synergistic cell survival inhibition up to 70%. This observation was further confirmed with increasing Gemcitabine concentrations in 7 murine pancreatic tumor cell lines as shown in figure 22F.

In conclusion, repression of Rac1 activity induces growth inhibition in pancreatic cancer cell lines over normal epithelial cells, especially in combination with Gemcitabine.

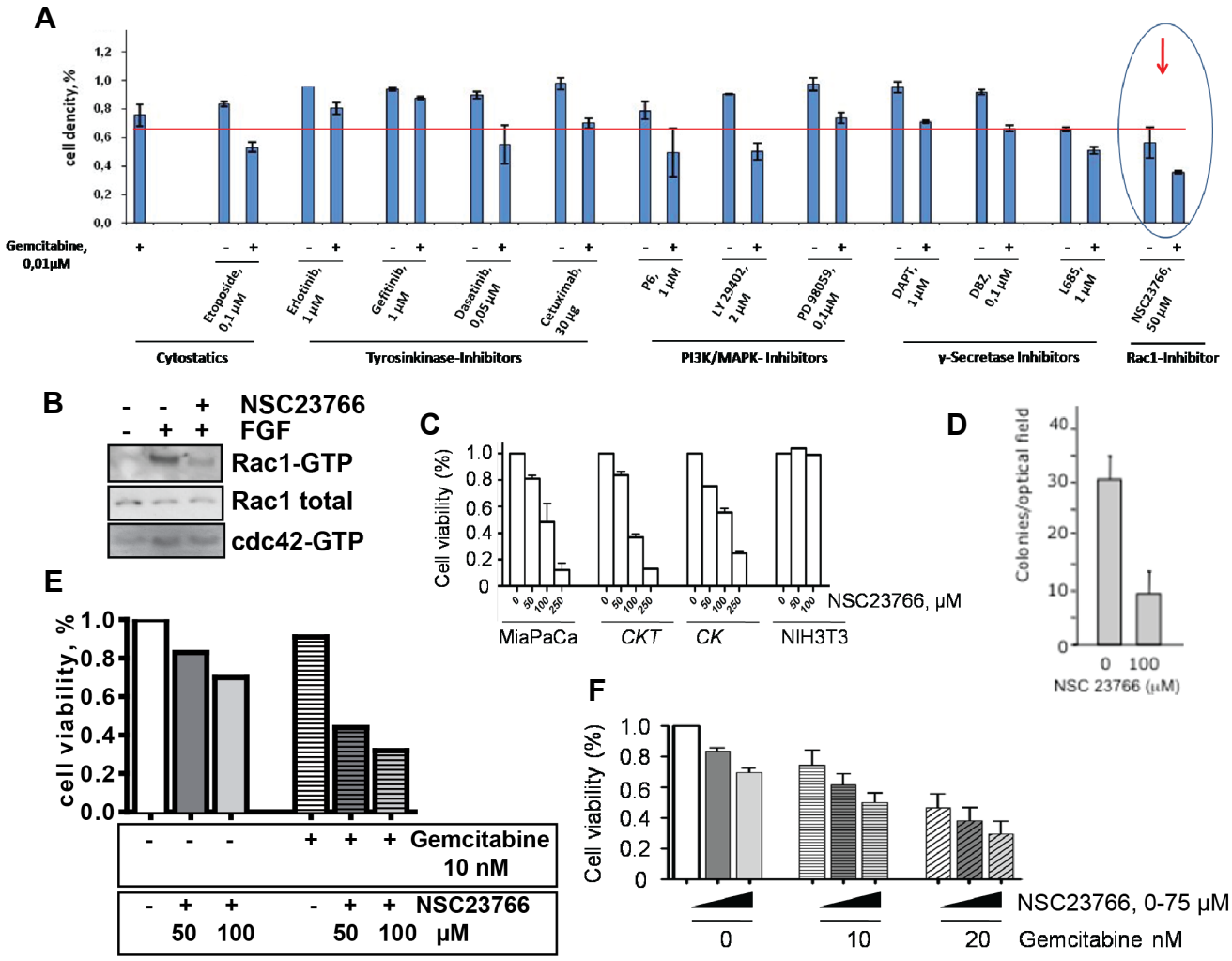

Figure 22: Inhibition of Rac1 activity by NSC23766 in murine primary and established human pancreatic cell lines. NSC23766 is a potent Rac1 activation inhibitor that substantially inhibits murine and human pancreatic tumor cell growth as detected by MTT assays and colony formation assay. Combination of NSC23766 and Gemcitabine reveales synergistic effects especially in cells that have not responded to Gemcitabine alone. A: Representative example of a primary murine cell line response to selected chemotherapeutics and small molecule inhibitors. All therapeutics were used at the in the literature standardized concentrations. Although combinations of etoposide, dasatinib, P6 and LY29402 also revealed synergistic effects, NSC23766 shows the most prominent tumor cell growth inhibition. Cell viability was determined via MTT assay in the full medium. Each bar represents at least 3 independent experiments. B: Rac1 pull down assay shows a clear Rac1-GTP reduction in the presence of NSC23766 inhibitor compared to the non-treated sample. The cdc42 levels remain unaffected upon Rac1 inhibition. Cells were starved for 16h with or without presence of 100µM NSC23766 and briefly activated with FGF (5 min) prior pull down assay. C: Dose dependent inhibition of cell growth by NSC23766 in human (MaPaCa2) and primary murine *CK* and *CKT* pancreatic tumor cell lines as well as non-tumorigenic fibroblastic cells (NIH3T3) detected via MTT assay. Whereas tumor cell lines reveal a clear dose-dependent growth inhibition fibroblasts do not change their proliferative capacity under the NSC23766 inhibition. D: NSC23766 inhibits anchorage independent growth of pancreatic tumor cells as detected by colony formation assay. E: Example of a cell line with a poor response to Gemcitabine treatment. Combination therapy of Gemcitabine with Rac1 activity inhibitor NSC23766 substantially inhibits cell growth in a dose dependent manner. Mean of three independent MTT experiments. F: Although murine pancreatic tumor cells respond well to Gemcitabine alone, a combined treatment with NSC23376 clearly induces increased synergistic inhibition of tumor cells growth persistent with the augmented Gemcitabine dose. Each bar represents a mean of 6 primary murine PDAC cell lines. Cell viability was detected by MTT assay.

3.2.2 Comparison of Rac1 activation inhibitors EHT1864 and NSC23766 using established *in vitro* system

Based on the promising results of chapter 3.2.1 an *in vitro* comparison of another commercially available Rac1 activation inhibitor EHT1864 was carried out. EHT1864 was tested together with NSC23766 inhibitor on 6 *CKP*$^{fl/fl}$ primary mPDAC cell lines. The MTT analysis revealed a clearly higher therapeutic efficacy of EHT1864 *in vitro* (Fig. 23). A representative example of concentration curves is shown in figure 23A. Here, IC50 of EHT1864 is 10 µM in comparison to IC50 of 78 µM for NSC23766. On average in 6 cell lines, EHT1864 showed 6.6 times stronger inhibition of tumor cell growth compared to NSC23766 (mean = 25.17 ± 5.6 µM for EHT1864, 158.8 ± 26.5 µM for NSC23766). Moreover, the EHT1864 inhibitor was efficient to reduce relative cell viability of confluent cells from 100% to 8 ± 9% level (Fig. 23C, 50µM), whereas cells treated with NSC23766 inhibitor were still viable even at the concentration of 250µM (cell viability of 80 ± 16%).

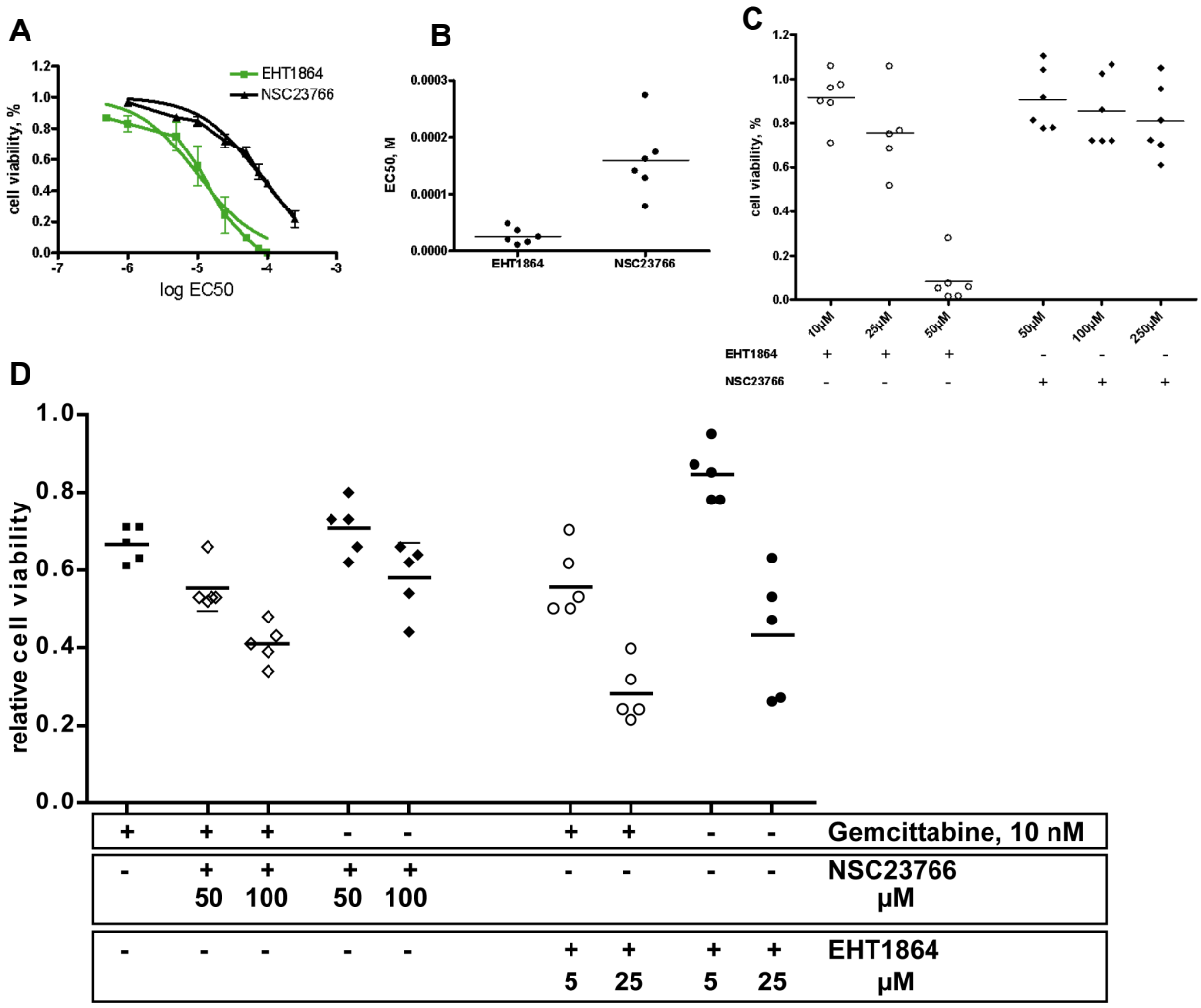

Figure 23: EHT1864 is a more potent inhibitor of cell growth compared to the NSC23766. *In vitro* MTT-based comparison of the two available Rac1 inhibitors EHT1864 and NSC23766 reveals a clear benefit of EHT1864. Compared to NSC23766, EHT1864 shows more than 6 times stronger inhibition of tumor cell growth as well as potent impairment of cell viability in confluent setting. In addition, synergistic effects of combination therapy with Gemcitabine are detectable already at four times lower concentration of EHT1864 than of NSC23766 inhibitor. Cell viability was measured by MTT assay in at least 3 independent experiments per cell line and calculated by Graph Pad Prism 4 software. A: Representative example of *CKP*$^{fl/fl}$ cell line showing the IC50 log curves for both inhibitors. The curves are shown as a mean of 3

independent experiments. B: IC50 plot for 6 *CKP*$^{fl/fl}$ cell lines. IC50 of EHT1864 is 6.6 times lower than the IC50 of NSC23766. C: Cell viability of 6 *CKP*$^{fl/fl}$ cell lines at confluent conditions under the treatment of indicated Rac1 activity inhibitors. 50µM EHT1864 caused nearly complete death of confluent cells. D: Comparison of NSC23766 and EHT1864 efficacy alone and in combination with Gemcitabine (5 *CKP*$^{fl/fl}$ cell lines). EHT1864 revealed greater synergistic effect at lower concentrations than NSC23766.

In addition, synergistic effects of Rac1 activity inhibitors in combination with Gemcitabine were tested using both inhibitors (Fig. 23D). As expected, Rac1 activity inhibition by EHT1864 together with cell growth inhibition by Gemcitabine resulted in a greater synergistic effect at lower concentrations then NSC23766. Also, already 5µM EHT1864 together with 10 nM Gemcitabine inhibited cell viability 1.3 times better that Gemcitabine alone. Furthermore, treatment of tumor cells with 25µM EHT1864 together with 10 nM Gemcitabine revealed 2.2 times better inhibition than Gemcitabine and 1.2 stronger cell growth impairment as 100 µM NSC23766 in combination with 10nM Gemcitabine. Thus, EHT1864 is a potent cell growth inhibitor especially in combination with Gemcitabine.

3.2.3 Pilot *in vivo* study of Rac1 inhibitors efficacy using *CKP*$^{fl/fl}$ model of endogenous mPDAC

In order to investigate the efficacy of EHT1864 and NSC23766 *in vivo* a pilot therapy study was performed using a group of 4 wild type and 4 *CKP*$^{fl/fl}$ mice. Therefore a new developed MRI-based platform for therapy monitoring that is described in chapter 3.3 was applied.

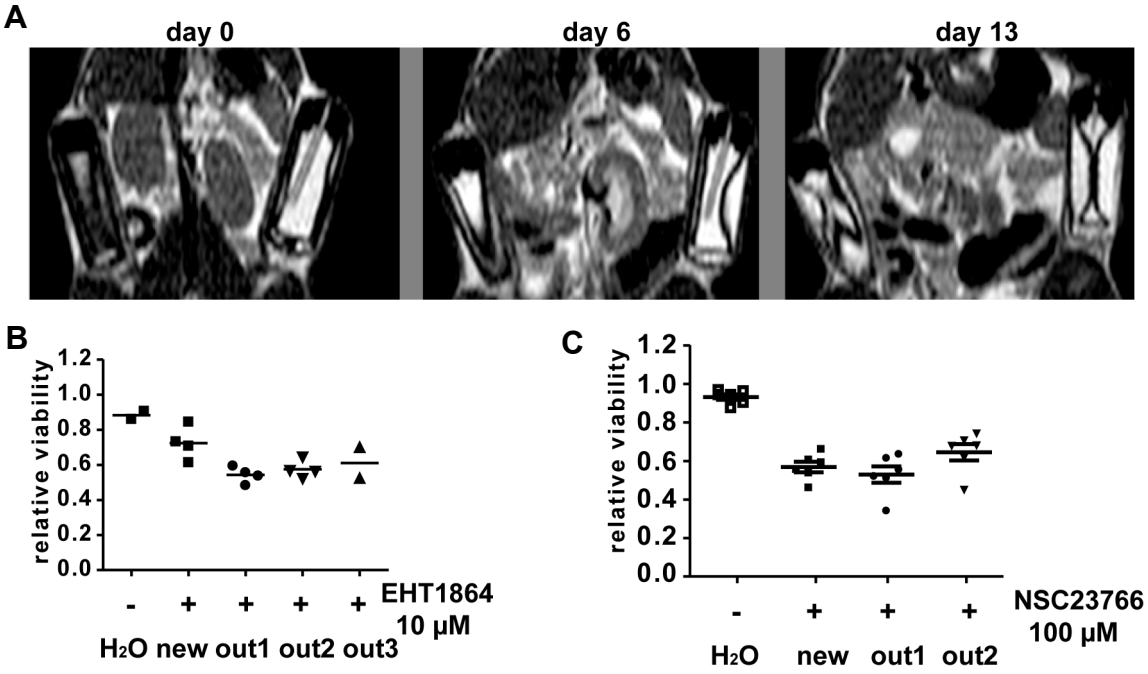

Figure 24: Validation of treatment technique as well as stability measurement of EHT1864 and NSC23766 *in vivo*. Both inhibitors remaine stable after resting for a period of 2 weeks in an Alzet osmotic pump implanted s.c. in a mouse body. A: Operation example of two Alzet osmotic pumps implanten s.c. into a mouse torso. Note how the salt sleeve of both pumps enlarged over time therefore pumping out the inhibitor solution, as shown by coronal T2w-MRI images. B, C: Validation of inhibitory efficacy of EHT1864 (B) and NSC23766 (C) after resting 2 weeks *in vivo*. Both Inhibitors remain effective at indicated concentration equally to the freshly dissolved compound (new). (out1 = inhibitor solution obtained from both pumps combined of mouse 1 after 2 weeks of treatment, etc.) The water control was taken from an animal bearing 2 pumps filled with water for 2 weeks.

First, Alzet osmotic pumps were validated for their functionality and possible side effects. Therefore, two pumps were filled with 100 µl of 100 µM inhibitor solution and implanted s.c. into a wild type mouse torso (2 pumps per mouse). The correct function of the pumps was monitored via T2w-MRI (Fig. 24A). As the water entered the salt sleeve, it compressed the flexible reservoir, displacing the treatment solution from the pump at a controlled, predetermined rate. The salt sleeves of both pumps enlarged over time, as shown by coronal T2w-MRI images. None of the mice (2 with NSC23866 and 2 with EHT1864) showed any visible side effects neither to the presence of pumps nor to the inhibitor treatment measured by weight and general appearance score (data not shown). Taken together, the use of Alzet osmotic pumps was considered as feasible for treatment administration of NSC23866 or EHT1864.

Next, the stability of both Rac1 inhibitors was tested *in vivo*. After 13 days *in vivo* the pumps were explanted post mortem and the remaining inhibitor solution was tested *in vitro* together with the freshly dissolved inhibitor on a subset of *CKP*$^{fl/fl}$ cancer cell lines (Fig. 24B, C). The water control was taken from an animal bearing 2 pumps filled with water for 2 weeks. As shown in figure 24B and C, both inhibitors (out) retained their therapeutic capacity and inhibited cell growth to the same extent as the fresh solution (new).

Finally, the efficacy of NSC23866 or EHT1864 inhibitors was tested in the *CKP*$^{fl/fl}$ mouse model of pancreatic cancer. Two animals were treated with two osmotic pumps containing 100 mM of each inhibitor solution and monitored regularly via MRI. The results of this pilot study are summarized in figure 25. MRI-based volume analysis revealed no differences in the tumor growth kinetics compared to the Gemcitabine treated and non-treated animals (Fig. 25A). All tumors treated with either of the two Rac1 inhibitors continued to growth.

However, diffusion weighted MRI using ADC analysis clearly revealed a treatment effect in the EHT1864 group (Fig. 25). Here, ADC mean values of vehicle treated tumors (NaCl) as analyzed by single slice MRI-histology correlation displayed mostly a decrease and/or no apparent trend over time (Fig. 25B). NSC23766 treated tumors appeared to follow this pattern (Fig. 25C). Still, more than 60% of the monitored EHT1864 treated tumor slices revealed a strong ADC mean value increase on day 3 (Fig. 25D). The change diminished on day 5 suggesting a transient response, however partially reappeared on day 13 (m2_tu1). An example of a more detailed representation of a non-responding and responding region is shown in figure 25E. The histogram of measured ADC values from non-responding region (left panel, black line, day 0) confirmed the histological observation that this area contains a large portion of preneoplastic lesions (ADC values > 1000 µm^2/s, also see chapter 3.3.6). Following the course of the therapy, the region has not responded to the treatment, as histograms shift to scale with lower values (colored lines), suggesting dense tumor growth as verified by corresponding histology (Fig. 25E, left bottom panel). In contrast, the responding region first showed a histogram of < 1000 µm^2/s (Fig. 25E, right panel, black line). However already at day 3 this tumor developed a second peak suggesting strong swelling or necrosis (Fig. 25E right panel, red line). Although the following measurement revealed a slight relapse with tumor fraction growing (day 6, blue line), the final histogram (green line, day 13) showed a very strong wide peak > 1000 µm^2/s histologically confirmed as necrosis (Fig. 25E, right bottom panel). The second animal treated with EHT1864 also revealed a necrotic tumor region, although of a smaller size. Thus, preliminary results strongly suggest that EHT1864 could be a potent inducer of tumor necrosis in murine PDAC. However, further studies with a larger animal number are necessary to verify this observation.

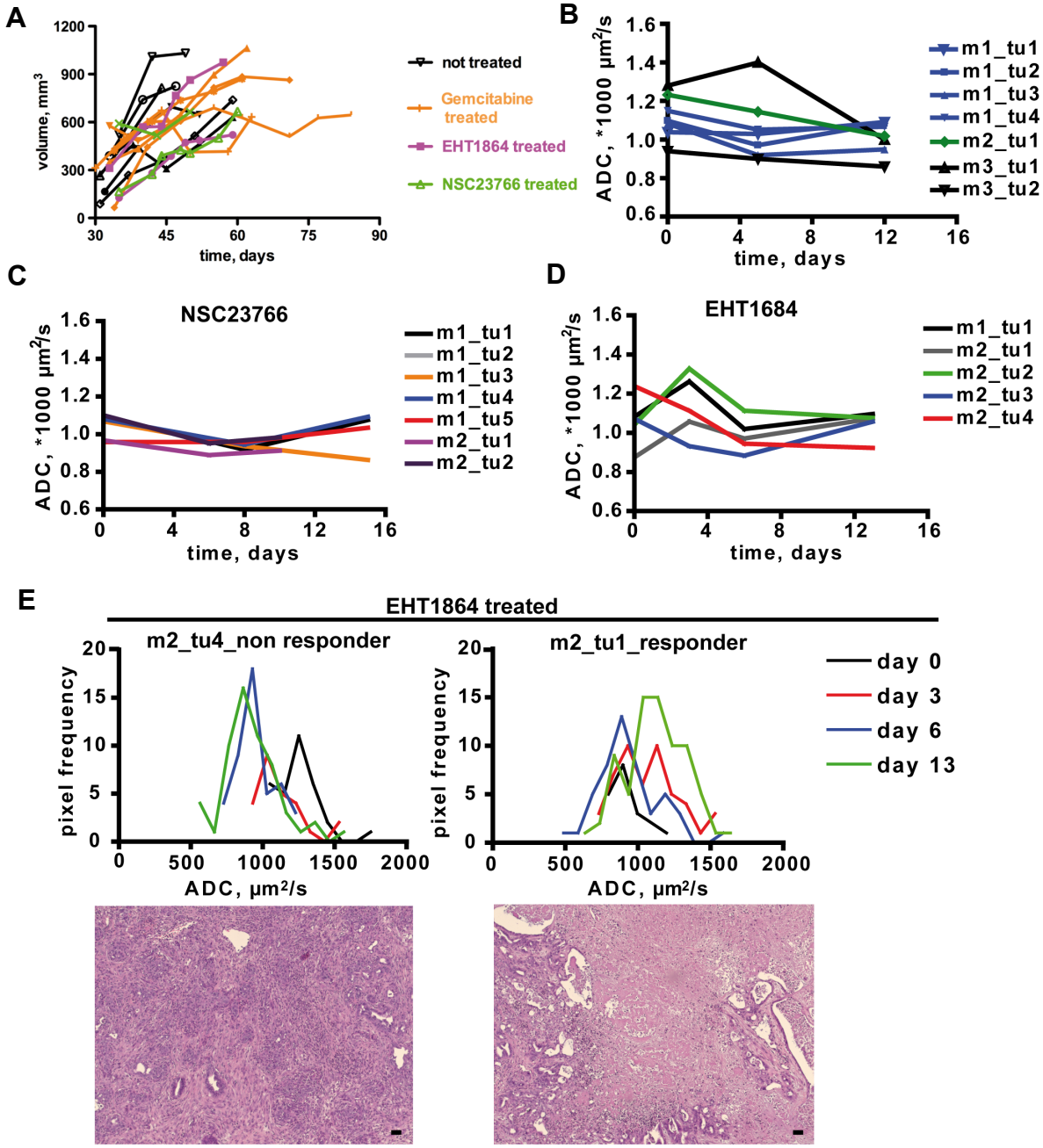

Figure 25: Treatment of mPDAC with EHT1864 caused tumor necrosis. A pilot *in vivo* study revealed necrotic areas in tumors of 2 animals treated for 2 weeks with EHT1864 successfully detected by DW-MRI and there out calculated ADC. However, there were no apparent changes in tumor growth monitored by T2w-derived volume analysis. All mice were of $CKP^{fl/fl}$ genotype. A: Volume analysis of tumor growth of indicated treatment. Each line represents one mouse monitored. B - D: Longitudinal slice based monitoring of tumor composition using ADC analysis. The vehicle (NaCL, B) treated tumors revealed stable or descending ADC values that are on average between 0.8 and 1.2 $*10^3$ $\mu m^2/s$. C: NSC23766 treated tumors shown no change in tumor composition monitored by DWI. D: Both mPDACs treated with EHT1864 revealed at least in one region per tumor a strong increase of ADC values on day 3 (m1_tu1, m2_tu1, m2_tu2). Some showed rather delayed (m2_tu3) or no response (m2_tu4) to EHT1864 treatment. E: Example of histologically verified region analysis of tissue composition under the EHT1864 treatment. A non-responder region displayed lower ADC values as shown by histograms of indicated time point and vital tumor end histology (left panel). Changes of tissue composition in the responder region were already detected at day 3 (red line, double peak suggesting necrosis) and substantially increased at day 13 (green line, the entire peak has shifted to the higher ADC values), revealing abundant necrotic area verified by histology (right panel). Scale bar = 50 µm.

3.3 Validation of preclinical MRI- and PET- based imaging platform using murine endogenous PDAC

As described above, genetically engineered mouse models (GEMMs) reflect very well not only human PDAC pathology but also mimic tumor behavior such as perfusion, stroma content and vascularity [43]. Therefore, endogeneous mPDAC models are valuable, predictive tools for preclinical research. The aim of this study was to validate clinically available MRI- and PET-based modalities as a comprehensive non-invasive imaging approach for GEMM characterization and therapy response monitoring.

3.3.1 Platform modalities and monitoring schedule

In order to validate the clinically available imaging modalities, GEMMs with different PDAC characteristics were analyzed for tumor growth kinetics, tissue composition, perfusion and metabolic status as well as proliferation using multiparametric MRI, [^{18}F]-FDG-PET or [^{18}F]-FLT-PET imaging (Fig. 26A).

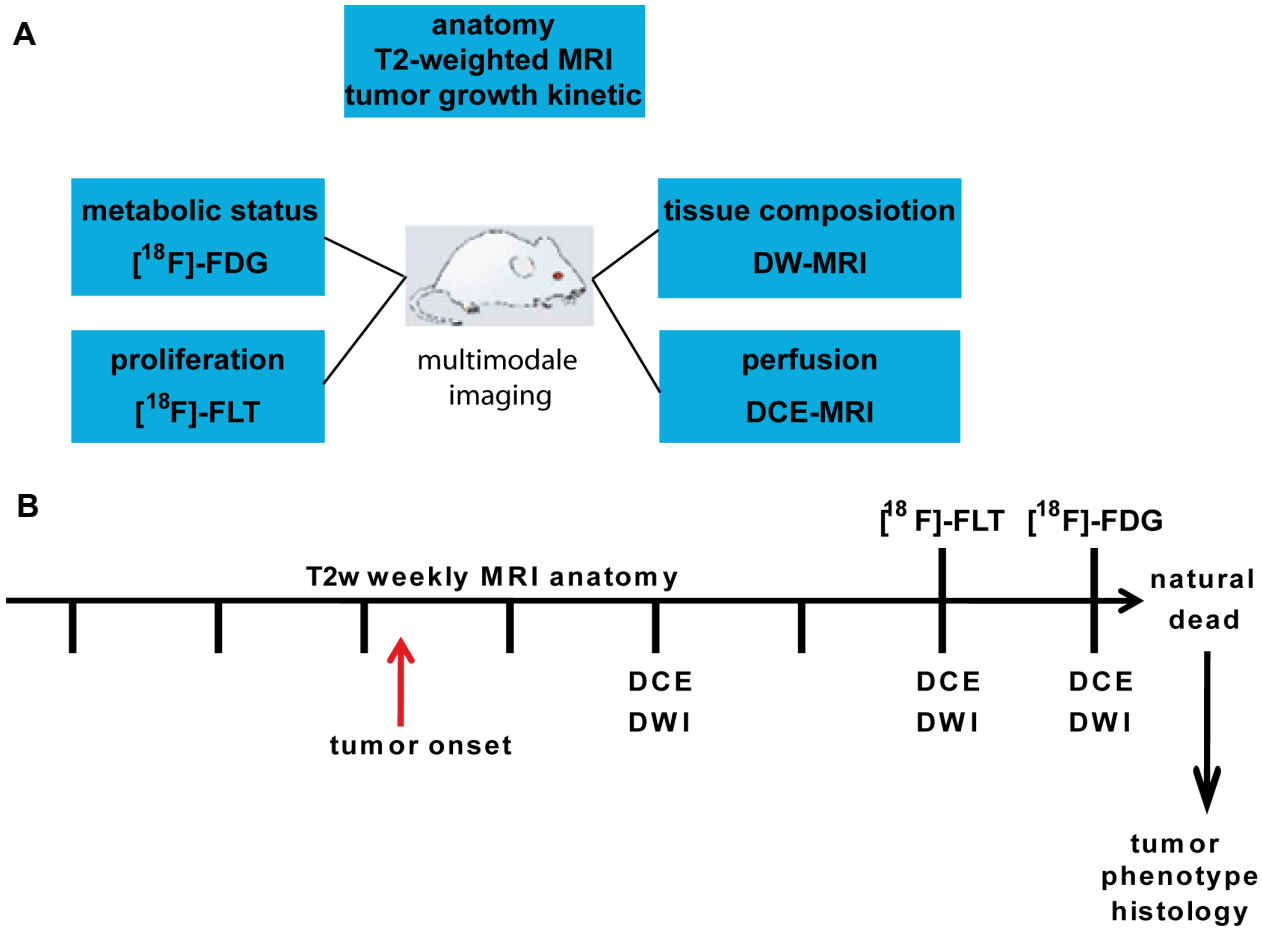

Figure 26: Multimodale imaging platform and protocol used for mPDAC characterization. A: Schedule of the study protocol. Summary of modalities applied in the study. B: Longitudinal protocol used for GEMMs characterization. Animals received weekly abdominal T2w-MRI, followed by more extensive protocol upon tumor detection including DW- and DCE-MRI as well as PET measurements and histological validation upon natural death.

As shown in figure 26B animals were subjected longitudinally to weekly abdominal and prior death whole body T2w-MRI for tumor volume calculation and metastases detection respectively. Upon identification of a solid tumor appearing in at least 3 slices on the T2w sequence, diffusion

weighted- and dynamic contrast enhanced MRI techniques were employed. Detecting Brownian motion of water molecules in the analyzed tissue DW-MRI gave valuable information about tumor tissue composition and possible spontaneous necrosis. Gd-DTPA enhanced tumor perfusion was detected using DCE-MRI. Depending on the health status of the animal, additional [^{18}F]-FDG-PET and/or [^{18}F]-FLT-PET scans were performed to assess tumor metabolic and proliferative status, respectively. Finally, mice were monitored until they showed any of the termination criteria such as 20% body weight loss, icterus, lethargy or ascites. End-scan data were used for histological correlation and validation of the performed analysis.

3.3.2 Phenotypical characterization of GEMMs used in the study

Five alleles were crossed in different combinations in order to obtain the following genotypes: *CKP*$^{fl/wt}$, *CKP*$^{fl/fl}$, *CKT*, *CKT*$^{R172H/wt}$ and *CKTP*$^{fl/wt}$ as shown in figure 27A (also see table 3). All genotypes showed differences in tumor onset, growth kinetics and appearance as well as metastatic pattern (Fig. 27B).

CKP$^{fl/wt}$ animals developed mostly G2 - G3 poorly differentiated adenocarcinomas with medium to low desmoplastic reaction in all pancreatic regions with tumor onset between the ages of 3-9 months. Once developed, tumors grew exponentially and caused mice to die within 2 - 4 weeks. Although, approximately 30% of the animals with these genetic alterations died of other causes like spinal paralysis or respiratory problems all of the 21 mice revealed histologically confirmed pancreatic tumor nodules of different size. Some mice presented with macroscopic but mostly microscopic liver metastases. The mean survival of this genotype was calculated at 168 days (Figure 27).

CKP$^{fl/fl}$ animals revealed the shortest mean survival time (55 days) as well as reliable 100 % tumor penetration approximately at the age of 5-7 weeks. Animals with tumors in pancreas head revealed significantly lower live expectancy due to the bile duct obstruction and very prominent icterus. Furthermore, app. 80% of the animals developed rapid ascites towards the end of their live span. Histologically, the most *CKP*$^{fl/fl}$ tumors were characterized as moderately differentiated highly fibrotic G2 – G3 mPDACs with abundant inflammatory infiltrates and were rich in reactive ductal structures compared to the *CKP*$^{fl/wt}$ tumors (Fig. 27A). In rare cases, G1 tumors were observed. However, these animals rarely had metastases to the liver or peritoneal wall.

Harboring an acinar cell-specific overexpression of *Tgfa,* murine PDAC developed from either mPanIN or mIPMN in *CKT*, *CKTP*$^{R172H/wt}$ and *CKTP*$^{fl/wt}$ mice. As previously published, all Tgfa-bearing pancreata were visibly enlarged already on the starting point of the study. Tumor onset as well as tumor progression were highly variable between the individual animals (Fig. 29 as described below). These animals developed frequently multiple cysts of different size, large mIPMN lesions as well as metastases (app. 70%) to the lung, liver as well as seldom to the spleen or peritoneal wall. Most of these tumors were characterized as G2 - G3 poorly to moderately differentiated adenocarcinomas with mid-level desmoplastic reaction (Fig. 27A, e.g. *CKTP*$^{fl/wt}$, *CKT*). However, five acinus cell carcinomas (one with metastases to the liver) were observed and confirmed by positive amylase staining (Fig. 27A, e.g. *CKTP*$^{R172H/wt}$). Moreover, two mice developed sarcomatoid and four anaplastic carcinomas with no stroma and very high tumor cell density (Fig. 27A, e.g. *CKT*). More importantly, often the different regions were developed within one animal allowing simultaneous analysis of different tumors under the same circumstances. Similar to *CKP*$^{fl/wt}$ animals, not all mice died due to the tumor burden, however all animals revealed at least 2 - 3 small tumor regions in the pancreas as verified by histology. Animals with advanced mPDAC exhibited additional pathologies, such as ascites, pleural effusion, cachexia and/or jaundice. *CKT* animals survived the longest (on average 270 days)

reflecting intact presence of p53 tumor-suppressor gene, whereas partially lacking or mutated p53 led to a reduced mean survival of 98 days and 128 days in $CKT^{R172H/wt}$ and $CKTP^{fl/wt}$ mice respectively (Fig. 2/B).

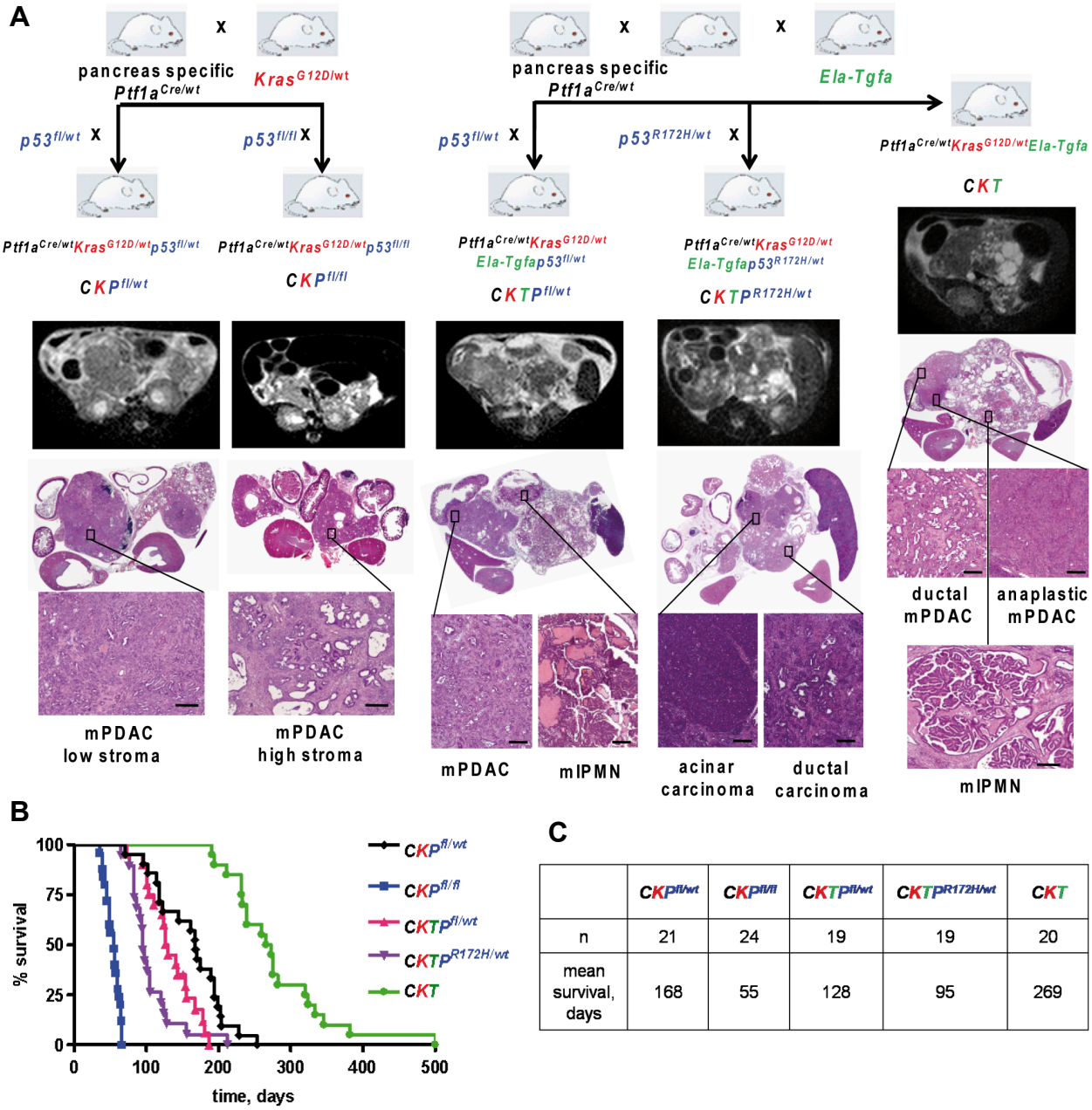

	CKP fl/wt	CKP fl/fl	CKTP fl/wt	CKTP R172H/wt	CKT
n	21	24	19	19	20
mean survival, days	168	55	128	95	269

Figure 27: Summary of genotype combinations and representative tumor histology of endogenous mouse models used in the study. The 5 genotype combinations have given rise to a wide spectrum of murine cancers including mPDAC with high and low stroma content, anaplastic and acinar cell carcinoma. All mice developed mPanIN lesions. Tgfa-bearing animals showed mPanIN and mIPMN lesions and revealed high intratumoral heterogeneity, with cystic and solid regions clearly distinguishable in the T2w-images. Note presence of up to 5 different lesions (cysts, mIPMN, mPanIN, mPDAC and acinar neoplasia) within the same mouse. Survival analysis correlated with the aggressiveness of introduced genetic alteration. A: Scheme of genotype combinations followed by representative example of anatomical appearance on axial T2w-image as well as corresponding histology slice of the indicated genotype. Enlarged boxes show distinct histological examples of indicated regions. Scale bar = 200 µm. B: Survival analysis and table of mean survival time of indicated genotypes. CKPfl/fl animals revealed the shortest live span, 100% tumor incidence and the most homogeneous histological appearance.

3.3.3 Anatomical T2w-MRI

The normal pancreas was not visible on the 1.5 T T2w-MRI. Once pancreatic preneoplastic changes occur, murine pancreata become more apparent as a bright and very heterogeneous region between the duodenum and the spleen. Single mPanIN lesions are not detectable on the T2w images. However due to the relatively high content of inflammatory infiltrates and edema mPanIN-based areas appear hyperintense relative to the tumor tissue and spleen (Fig. 27A left panel, $CKP^{fl/wt}$). T2w-MRI allowed robust identification of solid pancreatic nodules in the head, neck and tail of the pancreas (Fig. 27A). Pancreatic tumors appeared mostly as roundish hypointense lesions compared to the adjacent preneoplastic tissue. TGFa-expressing animals revealed high intratumoral heterogeneity, with cystic and solid regions clearly distinguishable in the T2w-images. Cysts were displayed as bright well delimited mostly round areas. Importantly, T2w imaging differentiated between mIPMNs and solid tumors where preneoplastic highly cellular mIPMNs appeared clearly hypointense compared to solid ductal hyperintense mPDAC fractions. Interestingly, some of the acinus cell carcinomas were partially mistaken for mIPMN due to their highly hypointence appearance compared with the surrounding lesions. However retrospectively, these tumors were clearly identified by DWI and histology as acinar cell neoplasia (Fig. 27A, $CKT^{R172H/wt}$ example). In cases where only one tumor type occurred, no prognosis of tumor type could be made on plane T2w-image. Also, anaplastic or sarcomatoid tumors were indistinguishable from ductal mPDACs on the T2w-MRI images.

Lung and liver metastases emerged hyperintense on the T2w-MRI in comparison to the surrounding normal tissue (Fig. 28). For robust metastases identification a minimum size of 30 mm^2 and nodule presence in at least 2 subsequent slices was required.

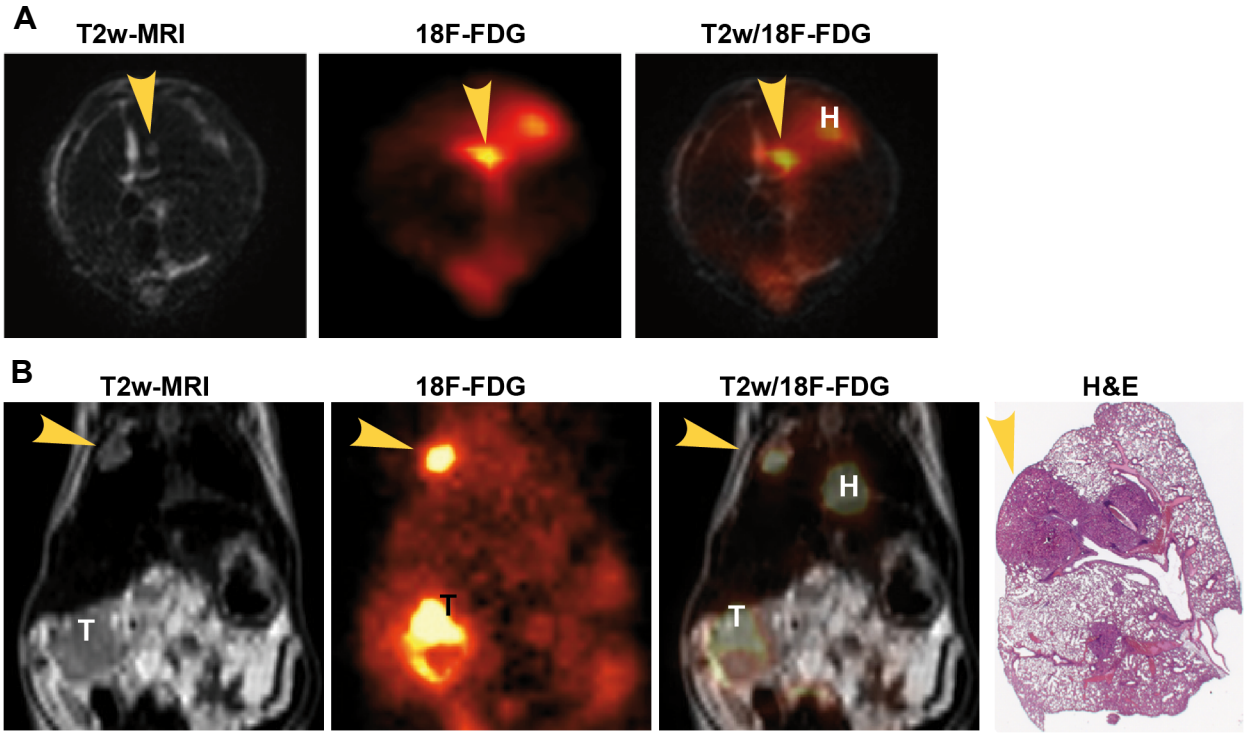

Figure 28: Detection of metastases in murine PDAC. Despite low resolution of 1.5 T clinical scanner macroscopic liver and lung metastases are clearly visible on the T2w and scans. Histologically confirmed mPDAC metastases (yellow arrow) show specific [^{18}F]-FDG tracer uptake. A, B: Representative example of liver (A) and lung (B) metastases found in two separate CKT animals. Left panel: T2w-MRI, middle left panel: [^{18}F]-FDG PET, middle right panel: T2w/[^{18}F]-FDG fusion image, right panel: H&E histology of the corresponding region. T = tumore, H = heart.

3.3.4 Longitudinal monitoring of tumor volume using 1.5 T MRI

Due to the high heterogeneity of the endogenous tumors as well as in order to exclude spontaneous necrosis or intratumoral cysts a semi-automatic volume calculation tool was developed (Fig. 29A). First, all T2w scans were equalized to a standard manually selected range in order to avoid single scan variability of the gray values. Next, whole tumors were manually defined in each slice by experienced radiologist and segmented automatically in cystic (gray) and solid (blue) parts according to customized threshold. Hence, calculated spontaneous course of solid tumor progression is presented in Fig. 29B.

The volume increase of solid tumor part indicated exponential growth of all tumors with different slopes as shown on the black curves (mean fit for the indicated genotype) compared to the red curves (mean fit assuming exponential growth of indicated genotype) (Fig. 29B). Although a mean growth pattern was clearly visible for every genotype, high heterogeneity was observed among single individuals within a group. Importantly, $CKP^{fl/fl}$ and $CKTP^{fl/wt}$ genotypes showed the most homogeneous group-wise growth pattern. In all cohorts first changes in pancreas appearance were possible to detect on the T2w-image at the initial volume of 100 – 400 mm^3 (Fig. 29C). The mean starting volume for each genotype were 296.40 ± 102.68 mm^3 ($CKTP^{fl/wt}$), 303.61 ± 114.69 mm^3 ($CKT^{R172H/wt}$), 504.23 ± 140.13 mm^3 (*CKT*), 235.76 ± 36.9 mm^3 ($CKP^{fl/wt}$) and 239.61 ± 158.46 mm^3 ($CKP^{fl/fl}$). Higher starting volume of the *CKT* animals reflected later enrollment of these animals into the study (app. at 3 months of age, due to later cancer onset). The tumor-end-volume was very heterogeneous and ranged between 300 mm^3 and 3900 mm^3 for all animals. The most prominent tumor volume increase revealed *CKT* animals with the mean end-volume of 2839.32 ± 649.16 mm^3, followed by $CKTP^{fl/wt}$ mice with the mean volume of 1826.35 ± 872.38 mm^3 (Fig. 29C). These findings correlated with the observation that Tgfa overexpressing animals are already born with an enlarged pancreas and lived the longest (Fig. 12, 27B). Other genotypes revealed mean tumor-end volume of 707.55 ± 313.07 mm^3 ($CKT^{R172H/wt}$), 592.89 ± 338.92 mm^3 ($CKP^{fl/wt}$) and 753.26 ± 240.42 mm^3 ($CKP^{fl/fl}$).

In order to further characterize the growth kinetics of each genotype, a slope of relative volume increase was calculated (Fig. 29D). The tumor onset and therefore volume value to which all further values were normalized, was determined visually by experienced radiologist on T2w-image. The five different genotypes revealed highly significant differences in the growth kinetics (ANOVA $P < .0003$). The highest mean slope of relative volume increase was observed in animals carrying single or double *TP53* deletions ($CKP^{fl/wt}$: 0.16 ± 0.08 (n = 10), $CKTP^{fl/wt}$: 0.25 ± 0.19 (n = 8), $CKP^{fl/fl}$: 0.23 ± 0.13 (n = 9)). However, $CKP^{fl/wt}$, $CKTP^{fl/wt}$, $CKP^{fl/fl}$ animal cohorts revealed also the biggest heterogeneity within the group regarding tumor kinetics (Fig. 29D). Thereby, $CKP^{fl/fl}$ animals showed the most homogeneous growth pattern in the fast growing tumor groups (Fig. 29B, D). Correlating with the published findings, *CKT* tumors grew slower but more homogeneous (mean slope 0.045 ± 0.043, n = 5). Interestingly, dominant negative $TP53^{R172H}$ mutation in the *CKT* background accelerated tumor growth only in 2 animals. This cohort displayed the most uniform as well as the slowest growth kinetics (Fig. 29D, mean slope 0.035 ± 0.042, n = 8). The differences in the mean slope of relative volume increase between the $CKTP^{fl/wt}$ and $CKT^{R172H/wt}$ cohorts were statistically significant ($P < .01$). In contrast to dominant negative *TP53* mutation, deletion of a single *TP53* allele in the *CKT* background significantly increased the tumor growth as represented by slope of relative volume increase in Fig. 29D ($P = .036$, T-test).

Taking together, the $CKP^{fl/fl}$ animals revealed a fast and the most homogeneous growth pattern compared to the other quick growing genotype cohorts.

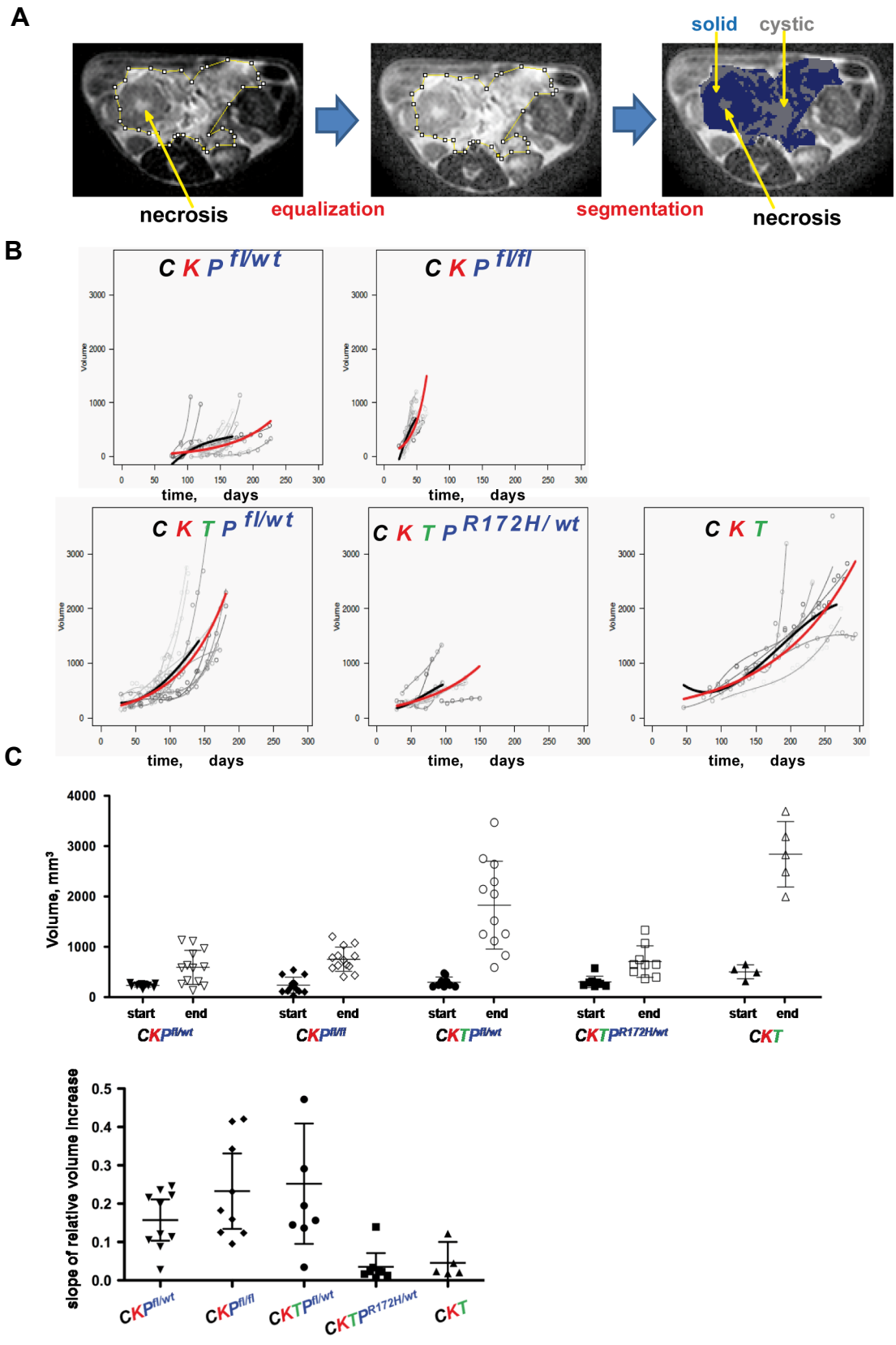

Figure 29: Longitudinal tumor volume analysis. T2w-MRI allows reliable tumor volume calculation using customized semi-automatic tool for extraction of solid tumor proportion. The five genotype cohorts differ significantly in their tumor onset, growth pattern and end-volume analysis. A: Example of semi-automatic volume calculation tool used for separation of solid (blue) and cystic (gray) parts of the tumor. B: Longitudinal tumor volume measurements of indicated genotype. The black curve represents mean fit for the indicated genotype. The red curve represents mean fit assuming exponential growth of indicated genotype. C: Tumor volume analysis. The initial tumor volume (filled symbols) and tumor-end volume

(empty symbols) of indicated phenotype. Although the starting volume is very similar, depending on genotype the end-point tumor volume is highly different. Especially *CKT* and *CKTP*$^{fl/wt}$ animals reach very high end-pont volume of > 2000 mm^2. D: Slope of relative tumor increase normalized to tumor onset determined visually by experienced radiologist revealed significant differences between the genotype cohorts (ANOVA, P < 0.0003). Tumors carrying single or double *TP53* deletion evolved considerably faster than tumors of other genotypes (*CKTP*$^{fl/wt}$ compared with *CKT* and *CKTP*$^{R172H/wt}$ P < 0.05 and P < 0.01 respectively). The *CKP*$^{fl/wt}$, *CKTP*$^{fl/wt}$ and *CKP*$^{fl/fl}$ cohorts display high slope heterogeneity within the cohort.

3.3.5 [^{18}F]-FDG-PET is a potent tumor prediction marker for metastatic mPDAC

[^{18}F]-FDG-PET allowed reliable visualization of murine pancreatic carcinoma (Fig. 30) as well as mPDAC derived lung and sometimes liver metastases (Fig. 28, 30D). Liver metastases were more difficult to detect due to their close location to other organs that highly enrich [^{18}F]-FDG tracer (Fig. 28A). As shown in figure 30A and B tumor regions (T, green line) verified by T2w-image and subsequent histological analysis revealed a very strong [^{18}F]-FDG uptake compared to the adjacent regions as well as preneoplastic tissue or mIPMN. However, [^{18}F]-FDG-PET analyses alone were complicated by non-specific uptake in brown fat tissue, heart, kidney, bladder and gut and routinely required MRI-PET image fusion. Fused images allowed reliable quantification of the tumor parts. The calculated tumor-to-muscle ratio (T/M) of solid tumors ranged between 2.8 and 12.72 with the mean values of 6.34 ± 2.38 for *CKT* cohort (n = 17) and 3.67 ± 0.44 *CKTP*$^{fl/wt}$ (n = 7) as well as 4.723 ± 1.38 for *CKP*$^{fl/fl}$ (n = 8) tumors respectively (Fig. 30D). Thus, T/M above 3 (n = 42) was considered as solid tumor. There were no significant differences between the genotypes analyzed.

The preneoplastic sections consisting of predominantly mPanIN and reactive ductal structures as well as mIPMN regions could be reliably identified as areas of low [^{18}F]-FDG uptake (Fig. 30A I, red line; 30B P). Precisely, the mean T/M ratio for preneoplastic mPanIN reach regions was 2.05 ± 1.06 and for mIPMN areas 2.33 ± 0.99 respectively (Fig. 30D). All T/M for solid tumors were significantly different form T/M raios of preneoplastic areas (ANOVA P < .0001). Thus, regions with T/M ratios below 3 were considered as predominantly preneoplastic. Moreover, mice bearing single genetic alteration of pancreas specific TGFa-overexpression (*T*) were used to prove specificity of [^{18}F]-FDG tumor uptake since these mice develop mostly adenomas [48, 49]. Indeed, some of these large benign lesions clearly failed to enrich [^{18}F]-FDG as shown in figure 30C. However, other animals of this cohort revealed higher content of mPanIN and reactive ductal structures as verified by histology. Such lesions revealed a low [^{18}F]-FDG uptake leading to a mean T/M ratio of 2.16 ± 1.06 in the *T* group (n = 4, Fig. 30D).

Additionally, lung metastases of size bigger than 10 mm^2 were distinguishable with the [^{18}F]-FDG-PET due to a higher tracer uptake in the metastatic region compared with the healthy organ (Fig. 28 and 30D). The lung metastases displayed a mean T/M ratio of 3.60 ± 1.89 (n = 8).

Furthermore, a second [^{18}F]-FLT PET tracer was tested as mPDAC marker. As shown in figure 30E a highly proliferative anaplastic tumor part verified by immunohistological staining of BrdU revealed [^{18}F]-FLT enrichment in comparison to the low proliferation area of mPDAC. However this tumor was the only one, which showed an [^{18}F]-FLT uptake of 1.66 and was considered as positive. The other 18 analyzed tumors were negative for [^{18}F]-FLT uptake and revealed a mean T/M value of 0.821 ± 0.13. In adition, mPDAC derived lung metastases were also negative for [^{18}F]-FLT uptake (mean T/M 0.833 ± 0.02, n = 3).Taking together, [^{18}F]-FDG-PET is a reliable mPDAC marker for solid tumor identification, and detection of lung metastases. Although, [^{18}F]-FLT PET may be a marker for highly proliferative murine anaplastic pancreatic tumors, the more

commonly found moderately proliferative mPDACs as well as lung metastases typically remained negative for this tracer.

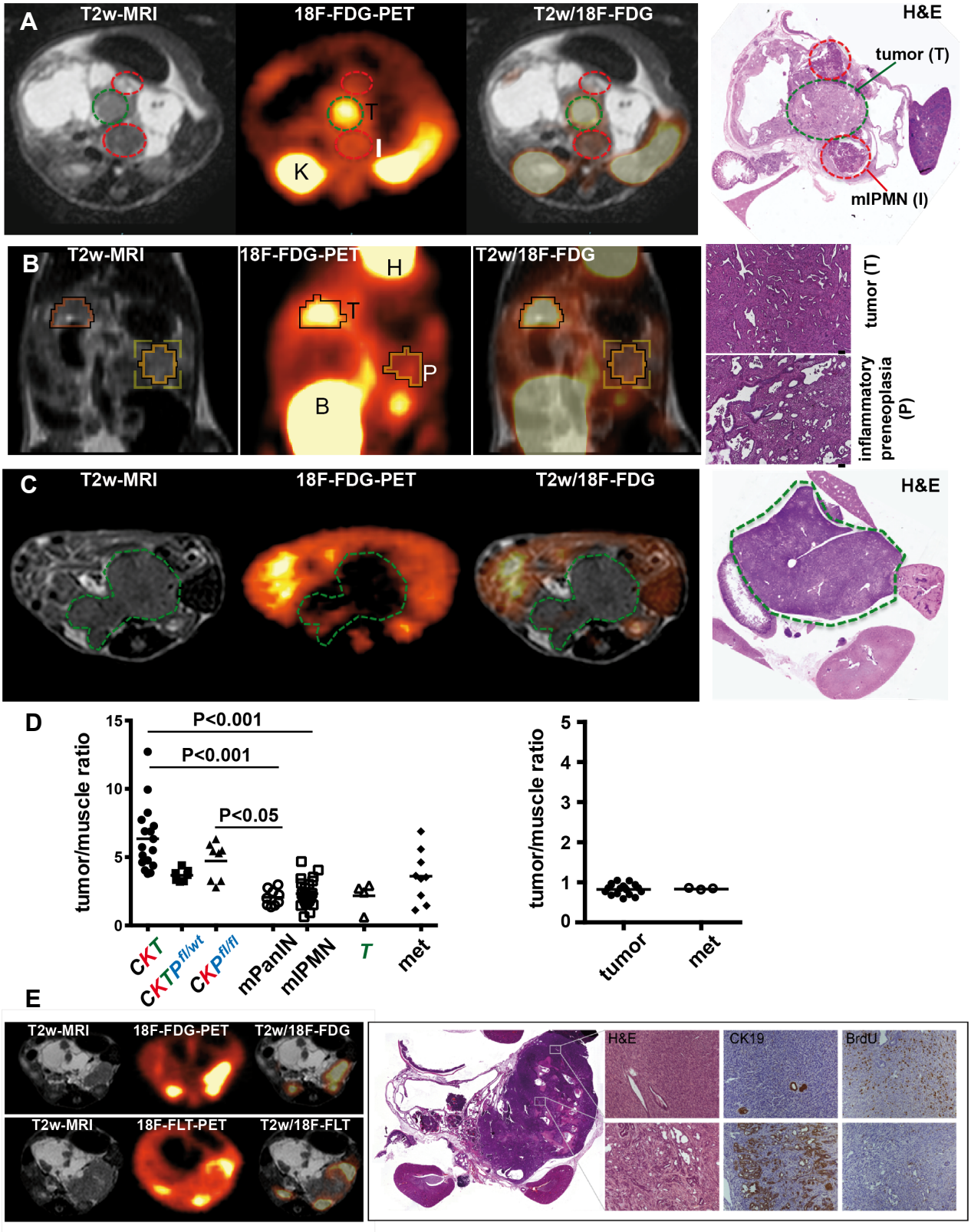

Figure 30: Evaluation of [^{18}F]-FDG and [^{18}F]-FLT tracers as tumor marker for mPDAC. Representative examples of tumor detection using [^{18}F]-FDG- and [^{18}F]-FLT-PET as well as T/M ratio quantification. While [^{18}F]-FDG-PET reliably identified pancreatic tumors and lung metastases, [^{18}F]-FLT-PET was positive only in one animal. Predominantly preneoplastic regions were determined by T/M < 3. A: An example of *CKTP$^{fl/wt}$* animal showing distinct [^{18}F]-FDG-enrichment in the tumor region (T, green line) verified by histology. mIPMN regions (I, red line) were clearly negative. K = kidney. B: An example of *CKP$^{fl/fl}$* animal

revealing distinct [^{18}F]-FDG-enrichment in the tumor region (T) and low tracer uptake in the preneoplastic mPanIN reach area (P). B = bladder, H = heart. C: Tgfa mice exhibited large, [^{18}F]-FDG negative lesions. A-C: Left panel: T2w-MRI, middle left panel: [^{18}F]-FDG-PET, middle right panel: T2w/[^{18}F]-FDG fusion image, right panel: H&E histology of the corresponding region. D: T/M quantification of mPDAC of indicated genotype, preneoplastic regions, mIPMN, Tgfa animals and lung metastases (met) for [^{18}F]-FDG-PET (left panel) and all tumors combined as well as lung metastases for [^{18}F]-FLT-PET (right panel). The T/M values of preneoplastic regions differ significantly from those of the tumor parts (ANOVA, P<0.0001). E: Multimodale PET-imaging of a pancreatic tumor from a *CKT* animal. Ventral tumor region showed specific [^{18}F]-FLT uptake; dorsal tumor region was [^{18}F]-FLT negative. Both regions revealed high [^{18}F]-FDG uptake. Histologically, ventral tumor part revealed an anaplastic, CK19 negative, highly proliferative phenotype. The amount of BrdU positive cells in the [^{18}F]-FLT-PET enriched tumor region was significantly higher compared to the [^{18}F]-FLT-PET negative, CK19 positive, low proliferative, ductal tumor area. Left panel: T2w-MRI, middle left panel: [^{18}F]-FDG-PET, middle right panel: T2w/[^{18}F]-FDG fusion image, right panel: H&E, CK19 and BrdU stainings of the corresponding region.

3.3.6 Validation of DWI-MRI-derived ADC as marker for tumor composition

Diffusion-weighted imaging (DWI) describes tissue composition and gives information about the cellular content of the tumor. Therefore, the aim of this study was to test apparent diffusions coefficient (ADC) as a marker for stratification of different tumors and/or preneoplastic tissue, as well as detection of spontaneous necrosis. In order to test sensitivity of apparent diffusions coefficient (ADC) in different mPDAC regions, an example *CKTP$^{fl/wt}$* mouse was analyzed. As shown in figure 31A and B all four histollogically distinct regions were clearly identifiable on the ADC-map and reveal distinct histograms. Cell dense acinus cell neoplasia revealed a mean ADC value of 0.56 *10^3 µm^2/s and was clearly distinguishable on the histogram analysis as a sharp peak with low ADC-values (red line). Vital mPDAC with preneoplastic areas (blue line) displayed a mean value of 0.79 *10^3 µm^2/s. The histogram of the necrotic ductal tumor overlapped with the vital tumor on the histogram, however revealed a second peak by approximately 1.2 *10^3 µm^2/s as well as a long tail of higher values representing necrosis (mean value 1.32 *10^3 µm^2/s). Finaly, mIPMN appeared very cellular and had a mean value of 0.88 *10^3 µm^2/s, as well as overlapped with the tumor histograms. However, mIPMN are very distinct hypointense on the T2w-images and can be therefore easily differentiated from the tumor (Fig. 27A, 30A). Thus, DWI was potent in identification of morphologically different areas and calculated ADCs were discriminating different parts of the tumor within the same animal.

Following the observation made above, the applicability of ADC as tumor marker was further quantified using a larger animal cohort grouped by histological appearance independently of the genotypes. Preneoplastic lesions with inflammatory tissue were detected with ADC values higher than 1,2 *10^3 µm^2/s. mIPMNs exhibited mean ADC value of 0.99 ± 0,02 *10^3 µm^2/s. Solid highly ductal stroma rich mPDAC had a mean ADC value of 1.031 ± 0.02 *10^3 µm^2/s, while sparsely ductal low stroma tumors displayed a mean ADC value of 0.80 ± 0.01 *10^3 µm^2/s. Undifferentiated acinus cell carcinomas and anaplastic PDACs exhibited the lowest mean ADC value of 0.67 ± 0.03 *103 µm^2/s.

In addition, correlation of tumor cellularity and collagen content with the corresponding ADC values was determined by histological stainings of haemalaun and collagen in a subset of representative animals. As expected ADC correlated strongly with cellularity r^2 = 0.73 and desmoplastic reaction r^2 = 0.65 (Fig. 31C, D).

In summary, ADC appears as a higly applicable tool and potential biomarker for differentiation between the tumor types as well as preneoplastic and inflammatory areas.

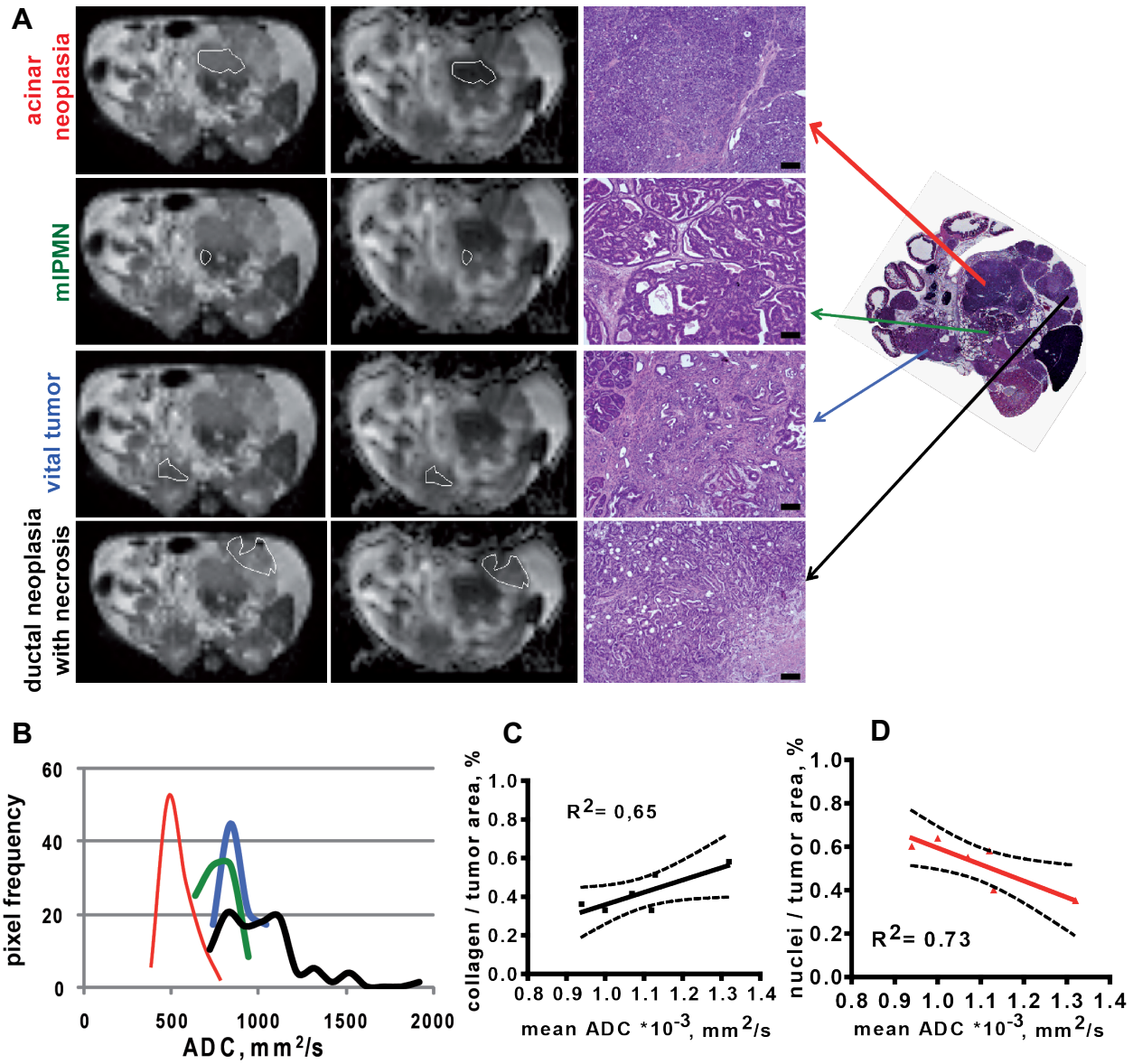

Figure 31: ADC is a potent tumor marker discriminating different tissue composition. Representative example of morphologically different areas and therewith associated ADC histograms revealed clear detection of different parts within the same animal via DWI. Spontaneous necrosis was also clearly detectable. Mean ADC values correlated well with tumor cellularity and collagen content. A, B: An example of *CKTP*$^{fl/wt}$ animal showing four distinct histological regions on the corresponding overview H&E staining (left picture). Necrotic (black arrow), vital (blue arrow) and acinar cell (red line) tumors as well as mIPMN were clearly distinguishable on the ADC-map as well as with the resulting histograms. Left panel: T2w-MRI, middle panel: ADC-map, left panel: H&E histology of selected tumor region. Scale bar = 200µm. C,D: Histological correlation of mean ADC values with collagen (Movat staining) content of the tumor (C) as well as tumor cellularity (D).

3.3.7 DCE-MRI is a potential discriminator for different tumor types

DCE-MRI using Gd-DTPA as contrast agent provides information about tumor perfusion. To answer the question if tumors developed in the 5 investigated genotypes can be discriminated by DCE-MRI, 38 tumors were measured prior the sacrifice. As shown in figure 32A, no significant differences were detected between the different genotypes using the whole tumor DCE – analysis. The mean $iAUC90_{rel}$ were 1.28 ± 0.9 for *CKP*$^{fl/wt}$ (n = 7), 1.99 ± 0.5 for *CKP*$^{fl/fl}$ (n = 8), 2.04 ± 0.95 for *CKTP*$^{fl/wt}$ (n = 10), 1.98 ± 0.7 for *CKTP*$^{R172H/wt}$ (n = 5) and 1.81 ± 0.55 for *CKT* (n = 8).

However, based on the prior observation, that Tgfa-overexpressing tumors revealed high intra-individual differences a more exact analysis may be needed in order to see inter-tumoral variances via DCE-MRI. An example of this analysis is shown in figure 32B. Based on histological appearance whole tumor was divided into 4 regions: acinar neolasia, ductal neoplasia with necrosis, vital ductal tumor and mIPMN. Different regions were characterized by different perfusion status. Vital ductal tumor (blue line) was relatively well perfused compared to all other regions, followed by moderate perfusion status in the cellular mIPMN (green line). Spontaneous necrosis in a ductal tumor was clearly detectable via DCE-MRI resulting in a slow upwards slope of the Gd-DTPA-curve (black line) compared to the vital tumor curve (blue line). This curve flow describes passive Gd-DTPA diffusion into the tumor rather than active perfusion. Surprisingly the region of acinar neoplasia was very badly perfused (red line) compared to all other areas.

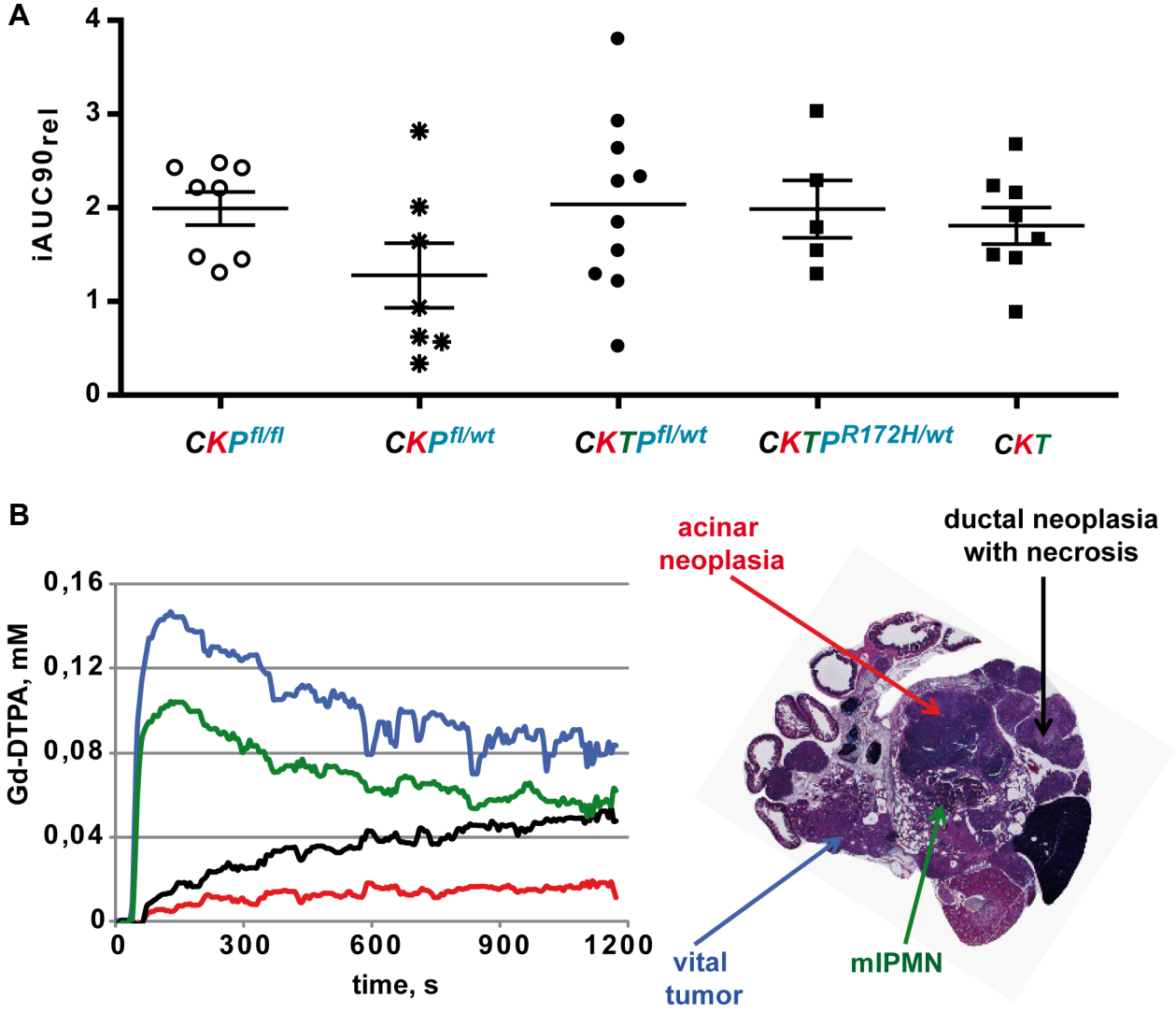

Figure 32: DCE-MRI is a potent discriminator of different tumor types within the same animal. Whole tumor analysis by genotype revealed no significant differences between the tumors. Single slice based DCE-MRI analysis closely correlated with the corresponding histology of the tumor clearly displayed intra-individual differences within the pancreas of the same animal. A: Summary plot of $iAUC90_{rel}$ of whole tumor analysis of indicated genotype. B: Representative example of single slice DCE-analysis (left panel) and its histological correlation (right panel). Acinar neoplasia (red line) and necrotic ductal tumor (black line) were badly perfused in contrast to the well-perfused vital ductal tumor (blue line) and mIPMN (green line).

In conclusion, whole tumor analysis and grouping by genotype revealed no differences between the tumors. However, DCE-MRI may be a potent discriminator of the various tumor types and revealed intra-individual differences even in the same animal. For this reason, single slice DCE-

MRI analysis in close correlation with the histological appearance of the tumors is needed in order to further prove the DCE-MRI as a usable marker. However, this analysis exceeds the scope of this work and will be carried out in a different investigation.

3.3.8 Longitudinal monitoring of spontaneous course of tumor progression via multi-parametric imaging

The applicability of the multimodal imaging platform for detection of spontaneous necrosis was tested in a longitudinal pilot study using a small group of 3 *CKTP*$^{fl/wt}$ animals. Figure 29 shows a representative example of spontaneous tumor necrosis detection within the period of 2 weeks.

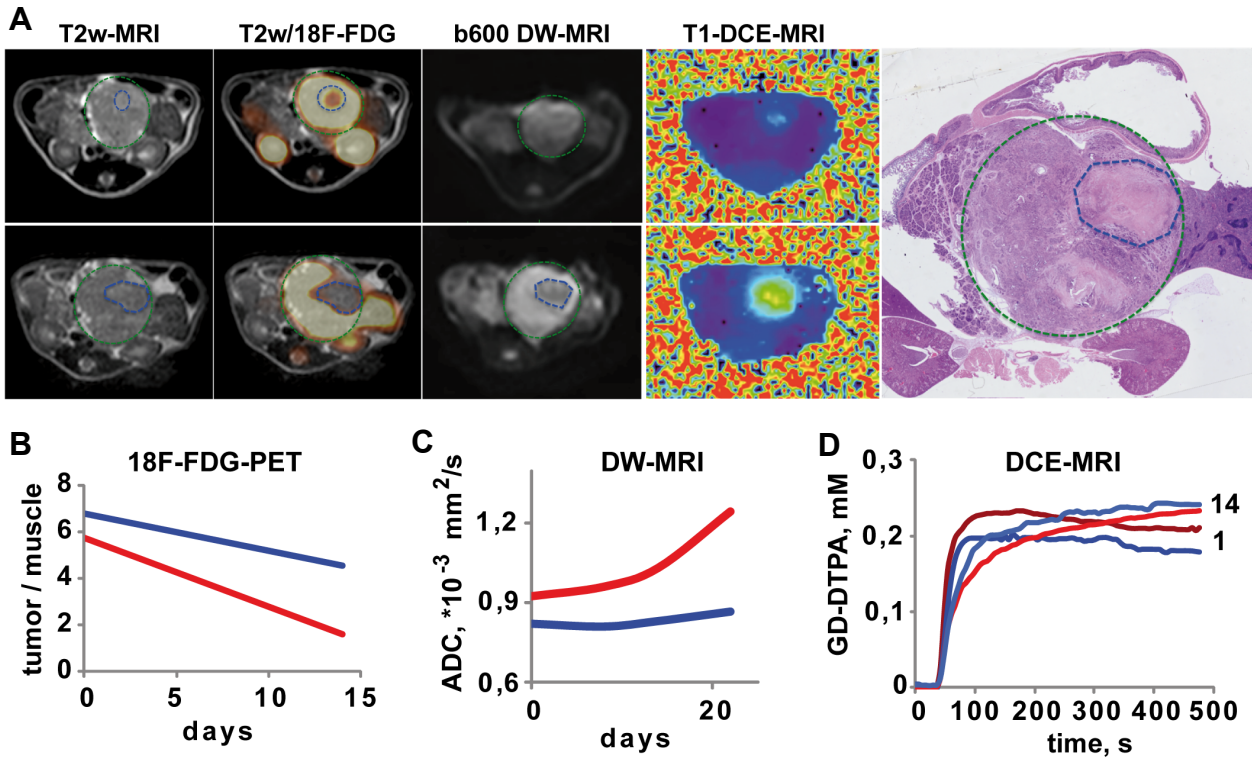

Figure 33: Longitudinal observation of spontaneous tumor development and necrosis detection using multimodale imaging platform. Spontaneous necrosis is clearly identifiable with all functional modalities used in the study. A: Summary of longitudinal protocol used for GEMMs characterization. T2w image of large solid tumor in a *CKTP*$^{fl/wt}$ animal at day 1 (upper panel) and day 14 (buttom panel) of imaging schedule. T2w/[^{18}F]FDG PET fusion image shows a small region of reduced tracer uptake (upper middle left panel), which enlarges over time (bottom middle left panel). Corresponding b600 images identify the necrotic region at late time point only (middle panel). Corresponding T1 color maps reveal reduced T1 shortening after Gd-DTPA injection at early time point, which is more pronounced at late time point (right middle panel). H&E staining confirms large necrotic tumor region surrounded by vital tumor tissue (right panel). B, C, D: [^{18}F]-FDG (B), ADC (C) values and Gd-DTPA concentration curves (D) plotted for vital (blue line) and whole tumor (red line) regions.

As previously described, T2w-MRI allowed robust identification of solid pancreatic mass in head of the pancreas (Fig. 33A upper left panel). In this example, two weeks later (Fig. 33A bottom left panel) T2w-MRI images revealed a bigger pancreatic mass, consistent with the rapid tumor growth. Spontaneous necrosis was not clearly identifiable by T2w-MRI. However, all other used modalities allowed a robust identification of spontaneous necrosis within the tumor. Thus, [^{18}F]-FDG-PET revealed already on the day 1 a small region of reduced tumor uptake suggesting the presence of necrotic area (Fig. 33A upper left middle panel). This assumption was confirmed by a second [^{18}F]-FDG-PET scan on day 14 showing a large cold area within the tumor (Fig. 33A

bottom left middle panel). Slice based tumor uptake analysis of this region revealed an apparent decrease in T/M ratio in the whole tumor (red line) as well as in the vital part (blue line) suggesting scattered necrosis also in the vital area (Fig. 33B). DW-MRI analysis underlined this statement. Although, no clear necrosis area was visible on b600 image on day 1, the mean ADC tumor value was higher 0.924 $*10^3$ $\mu m^2/s$ than the vital tumor ADC 0.82 $*10^3$ $\mu m^2/s$ (Fig. 33A middle panel, C). In the course of observation, the mean ADC value for the whole tumor increased up to the 1.244 $*10^3$ $\mu m^2/s$ underlying robust necrosis identification by this method. Due to the scattered necrosis, also the ADC values of vital tumor slowly increased (Fig. 33C). Finally, spontaneous necrosis was robustly discriminated by T1 colored map of DCE-MRI (Fig. 33A right middle panel, D). Whereas only a small area of low perfusion was present on day 1 of the analysis, a large region of low contrast is identifiable on day 14 on the T1-map. The Gd-DTPA concentration curves underline the observation: both whole tumor (red lines) as well as vital tumor (blue lines) curves change their shape after 14 days. Instead of peak after injection representing a vital tumor, the curves reveal a slow slope increase consistent with partial passive diffusion of Gd-DTPA into the ROI area due to necrosis (Fig. 33D). Similar observations were made with the other 2 animals used in this study (data not shown).

In summary, the represented multimodal platform allowed a robust identification of spontaneous necrosis using [^{18}F]-FDG-PET, DW-MRI and DCE-MRI.

3.3.9 Multimodal platform validation for therapy response monitoring using s.c. transplanted mPDAC model.

In order to validate the methods established above in a therapeutic setting a cohort of s.c. transplanted mPDACs was generated using immunocompetent C57BL/6 animals. The study protocol is summarized in figure 34A. After positive tumor identification via T2w-MRI, animals were stratified into two cohorts for Gemcitabine and placebo treatment. A pre- and post-therapeutic imaging using [^{18}F]-FDG-PET and DCE-MRI were additionally applied for response monitoring. Due to the close proximity of tumors to the surrounding air and therefore resulting high image distortion, no DWI was possible to measure. After two weeks of therapy imaging modalities were verified by histology.

S.c. implanted murine PDACs revealed exponential growth under the vehicle treatment determined by volume analysis of T2w-MRI images (Fig. 34B). The mean tumor doubling time in the vehicle treated group was 6.834 ± 0.34. Gemcitabine treated s.c transplanted tumors were growing more slowly in comparison to the vehicle treated group reveling a treatment effect (Fig. 34D). The mean tumor doubling time in this group was 8.251 ± 0.35. The differences were significant P = 0.0057.

In addition, [^{18}F]-FDG signal uniformly increased in the vehicle treated group correlating with the tumor growth (Fig. 34D). The mean T/M ratio of [^{18}F]-FDG-uptake increased 1.5 times from 7.039 ± 0.6 to 10.6 ± 1.13. In contrast, Gemcitabine treatment had a negative impact on the glucose uptake in the treatment group (Fig. 34E). Correlating with the slower tumor growth, animals treated with Gemcitabine revealed no increase in [^{18}F]-FDG T/M ratio over time before (7.34 ± 0.5 or after (7.11 ± 0.15) the therapy. Despite the fact that some of the tumors in the Gemcitabine treated group have not responded to the treatment the overall glucose uptake after the treatment was significantly lover in the Gemcitabine group in comparison to the vehicle treated cohort (P = .073).

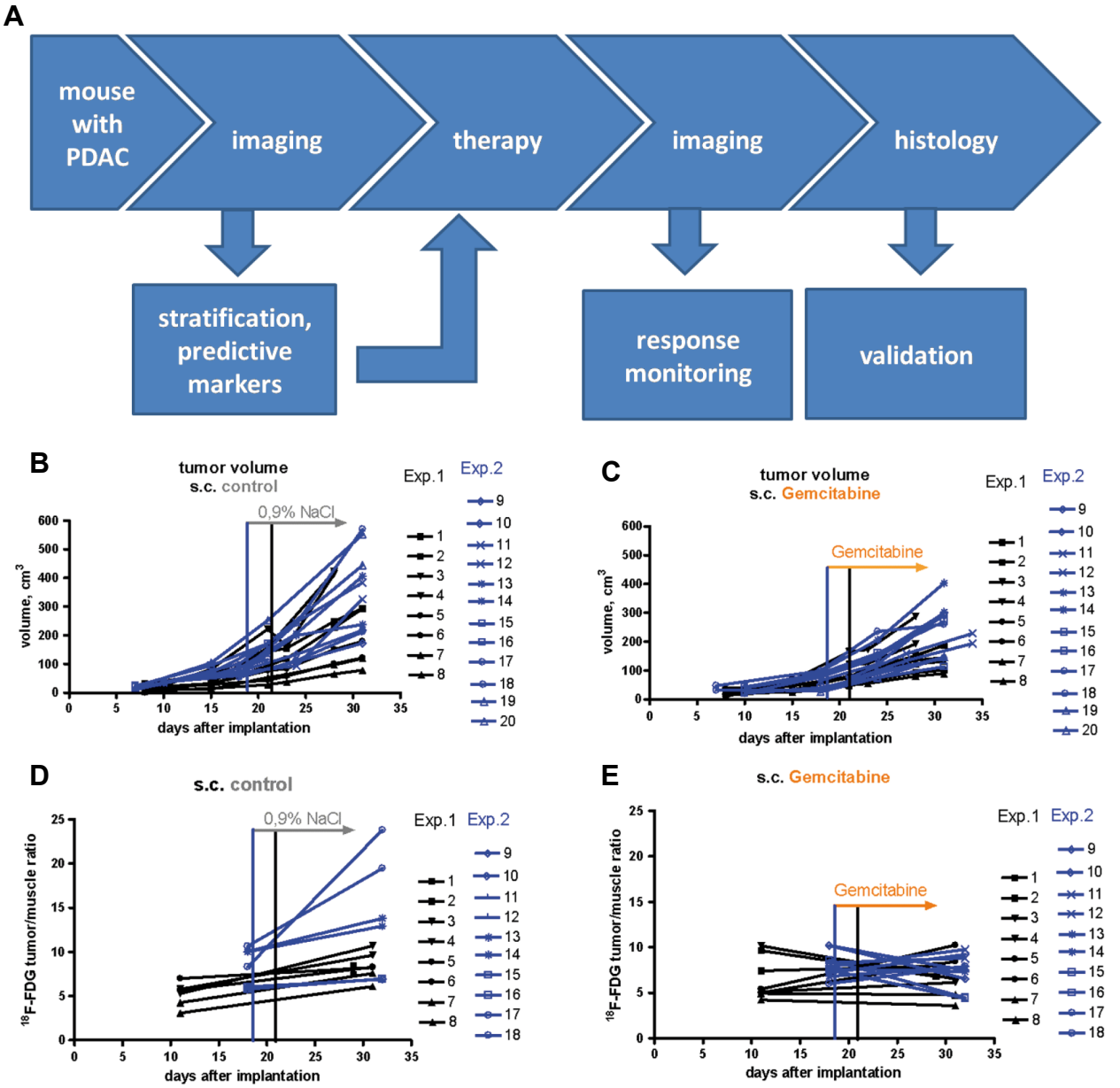

Figure 34: Therapy response monitoring in s.c. transplanted model of murine PDAC. A: Study protocol applied. After tumor identification via T2w-MRI, animals were stratified into two cohorts for Gemcitabine and placebo treatment. A pre- and post-therapeutic imaging using [^{18}F]-FDG-PET and T2w-MRI were additionally applied for response monitoring. After 2 weeks of therapy imaging modalities were verified by histology. B-E: Subcutaneous growth (B, C)) and [^{18}F]-FDG-uptake (D, E) of primary murine PDAC cells implanted into the wild type mice under vehicle (B, D) and Gemcitabine (C, E) treatment. Both imaging modalities demonstrate clear responsiveness of s.c. mPDAC to Gemcitabine treatment. Exp. = experiment.

The DCE-MRI analysis using Gd-DTPA as a contrast agent revealed no differences between the two treatment groups. The mean iAUC90rel prior the treatment was 1.48 ± 0.8 and 1.02 ± 0.2 for vehicle and Gemcitabine treated cohorts respectively. After the treatment mean iAUC90rel accounted for 1.12 ± 0.37 in the vehicle treated group versus 1.67 ±0.43 in the Gemcitabine treated animals.

Taken together, volume, [18F]-FDG and DCE-MRI were validated as therapy markers in a preclinical study with s.c. transplanted mPDAC. Volume analysis as well as [18F]-FDG-PET are clearly feasible for therapy response detection in this setting and may be applied in studies with

endogenous tumors. DCE-MRI analysis revealed no differences between the two treatment groups.

3.3.10 Pilot therapy study in endogenous mPDAC

Based on the study in s.c. transplanted tumors, therapy response monitoring was tested in a small pilot study using endogenous mPDAC of *CKT* (N = 6: m1-m3, m7 in the non-treated group and m1, m2 in the treated group) and *CKTP*$^{fl/wt}$ (N = 4: m4-m6 in the non-treated group and m3, in the treated group) models (Fig. 35).

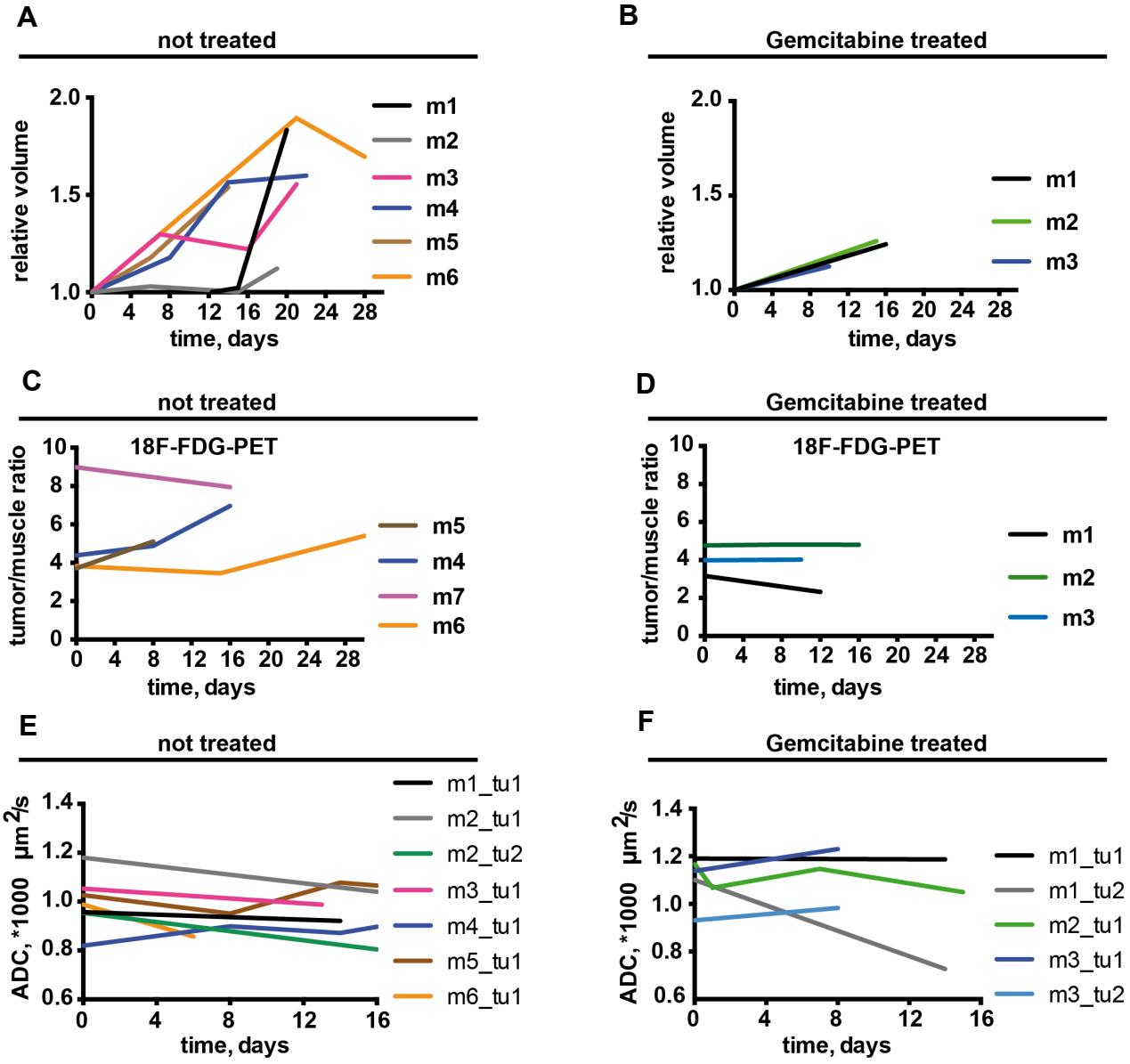

Figure 35: Tumor response monitoring in endogenous mPDAC using longitudinal multimodal imaging platform. Two groups of non-treated (A, C, E) and Gemcitabine treated (B, D, F) animals bearing endogenous mPDAC were followed using T2w-MRI for volume analysis, [^{18}F]-FDG-PET and DW-MRI. Relative tumor volume analysis revealed a slower increase in Gemcitabine treated group. Only trend, but no significant treatment-induced changes were observed using [^{18}F]-FDG-PET and DW-MRI between the groups. A, B: Whole tumor volume analysis normalized to the volume of mPDAC shortly prior the therapy start. C, D: [^{18}F]-FDG-uptake measured by T/M ratio of whole tumor. E, F: Slice-based DW-MRI analysis using ADC men values. Both groups revealed stable or descending ADC values suggesting dense tumor growth. m = mouse, tu = tumor.

As shown in figure 35A relative volume changes of non treated animals revealed high heterogeneity among the individuals. The calculated starting solid whole volume underlined inter-individual diversity (non treated group 269 – 5100 mm^3, treated group 358 – 3660 mm^3). Due to the high variability of tumor onset time and starting volume, a relative volume analysis was applied. Interestingly, Gemcitabine treated animals revealed slower tumor growth (0.015 ± 0.014 N=3) detected by slope of relative volume increase in contrast to the non-treated group (0.033 ± 0.034 N=6) (Fig. 35 A, B). However, the low sample size and large heterogeneity in tumor growth characteristics as well as histology (data not shown) raise a question of reliability of this observation. Although, the relative changes in tumor volumes after the therapy onset in this study were statistically significant (P = .0022), further tumor volume analysis with larger number of individuals and/or more homogeneous tumor model are necessary to verify influence of Gemcitabine on the tumor growth of mPDAC. Still, this study indicates that tumor volume could be used as reliable therapy monitoring read out parameter in endogenous mPDAC.

[^{18}F]-FDG T/M ratio showed a trend to increased tumor-uptake with the time in the non-treated group (Fig. 35C). Correlating with the slower tumor growth, the Gemcitabine treated animals showed either no change or a slight decrease in [^{18}F]-FDG T/M ratio (Fig. 35D). However, linear regression analysis revealed no significant differences between the cohorts. Moreover, the non-treated animals exhibited larger inter-individual variations as observed in the treated group, suggesting a higher inter-tumoral variability per se. Thus, further tests with larger cohorts are necessary in order to prove [^{18}F]-FDG T/M ratio as tumor monitoring marker in endogenous mPDAC.

In addition, diffusion weighted MRI were performed in 9 animals (non-treated N = 6), Gemcitabine treated (N = 3). Due to the abdominal location of the mPDAC image distortion was reduced compared to the s.c. transplanted tumors. Correlating with the results presented in chapter 3.3.6 and 3.3.8, tumors used in this study revealed ADC mean values from 0.82 till 1.19 $*10^3$ $\mu m^2/s$. Thereby most tumors were histologically confirmed as G2-G3 mPDAC with moderate to high stroma and duct content (data not shown). Only one tumor was of lower differentiation grade and showed an ADC value of 0.82 $*10^3$ $\mu m^2/s$. ADC mean values of non treated tumors displayed mostly a decrease and/or no apparent trend over time (Fig. 35E). Only one tumor in the non-treated group (m5_tu1) has revealed an ADC value increase, verified histologically as necrosis (Fig. 33). Most Gemcitabine treated tumors have shown a decrease of ADC mean value, suggesting a growing tumor, which becomes denser with the time (Fig. 35F). However one mouse (m3) revealed a slight increase in ADC value, suggesting tumor swelling or beginning necrosis that was verified histologically. Thus, ADC values could be a potentially sensitive parameter for changes of tissue composition upon treatment and identify single responders. However, overall analysis of linear regression has not revealed significant changes underlying the necessity of further evaluation for this imaging parameter in endogenous mPDAC.

Taken together, this pilot study showed that tumor volume could be a good monitoring parameter for therapy response surveillance. No significant differences between the Gemcitabine treated and non-treated cohorts were observed using [^{18}F]-FDG T/M ratio or ADC as read out parameters for metabolic status and tissue composition of tumors respectively. However, both imaging markers revealed a trend in response to Gemcitabine treatment and may identify single responders. Thus, further larger studies using more homogeneous model, e.g. $CKP^{fl/fl}$ are necessary inorder to validate all tree parameters as useful tumor response monitoring biomarkers.

4. Discussion

The therapeutic time window of patients with pancreatic cancer is very short or mostly already closed at the time of diagnosis [154]. Due to the retroperitoneal localization of the pancreas, absence of specific symptoms and lack of sensitive diagnostic techniques most patients are diagnosed with metastasized disease and therefore beyond curative resection. Moreover, even patients with complete resection relapse very often within 5 years after surgery [2]. In addition, Pancreatic Ductal Adenocarcinoma (PDAC), the most common and most aggressive type of pancreatic cancer, has extremely high intrinsic resistance for chemo- and radiotherapy with very little palliative options for advanced tumors [114]. Thus, intensive research in all fields of pancreatic cancer including molecular pathway analysis of PDAC onset and progression, early detection, and development of new therapeutic regiments is of utmost importance in order to improve pancreatic cancer patient's care.

In this work a comprehensive approach is presented combining basic and preclinical research platforms based on sophisticated use of Genetically Engineered Mouse Models (GEMMs). Precisely following aspects were investigated and will be discussed below:

1). The importance of Rac1 for actin reorganization, development of preneoplastic lesions as well as inflammatory reaction in murine PDAC and acute pancreatitis.

2). The benefit of combination therapy of EHT1864 or NSC23766 and Gemcitabine tested *in vitro* on primary pancreatic cancer cells as well as feasibility of chemical inhibition of Rac1 activity *in vivo*.

3). Characterization of murine pancreatic cancer heterogeneity and therapy response monitoring using quantitative MRI techniques and PET.

4.1 Rac1 is required for development of preneoplastic lesions and adequate inflammatory response during murine pancreatic carcinogenesis

Given the normal histology, no reconstruction by *Rac2/3* and normal survival of $CR^{fl/fl}$ mice, Rac1 does not seem to be essential for pancreatic development or adult tissue homeostasis. However, *Rac1* overexpression appeared to be relevant in the abnormal pancreas. In accordance to previous *in vitro* findings [106], weak acinar Rac1 expression increased *in vivo* upon CCK treatment, supporting the importance of Rac1 in acinar plasticity following inflammatory stimuli. In context of oncogenic $Kras^{G12D}$ the significance of Rac1 was confirmed by a strong staining in stromal cells surrounding acinar clusters and preneoplastic duct-like lesions. These observations are consistent with a gene expression study of human pancreatic samples where *Rac1* was found to be highly up-regulated in PDAC [75]. Interestingly, the stromal *Rac1* expression was already suggested in this study, since up-regulated Rac1 was found mainly in bulk PDAC tissue and not in tumor aspirates.

Despite the seemingly low expression, deficiency of *Rac1* had an impressive effect in $Kras^{G12D}$-induced carcinogenesis: Deletion of *Rac1* in the mouse pancreas not only drastically reduced the development of preneoplastic lesions and mPDAC in three different models but also significantly prolonged survival of $CKR^{fl/fl}$ animals. Moreover, no macroscopic metastases were observed in any of these highly metastatic GEMMs. However, the evident oncogenic role of Rac1 in $Kras^{G12D}$-induced pancreatic carcinogenesis was not explainable by differences in proliferation or changes in RAS/EGFR- dependent pathways essential for survival. In contrast to these findings, Kissil *at al*. found that loss of *Rac1* affects the proliferative capacity of $Kras^{G12D}$ baby mouse kidney cells [80]

and Wang *at al.* revealed a hyperproliferation-specific function of Rac1 in DMBA/TPA-induced skin tumor formation signaling through MEK and AKT activation [79]. However, developing acinar cells may react differently to the oncogenic pressure and rely on additional signals absent in lung or skin neoplasia conditions. In contrast to the observed almost complete tumor development abrogation in murine pancreas, only a delay but not inhibition of tumor development was observed in a *Kras*^{G12D}-induced lung cancer model [80]. Thus, other, yet unknown pathways may play critical role in mPDAC development. For example the role of Rac1 in the production and management of reactive oxygen species (ROS) via phagocyte-like NADPH osidase (Nox) may be an appropriate investigation target, since these molecules are strongly involved in both cancer associated inflammation and metabolic function of the pancreas [58, 155].

Initiation of pancreatic carcinogenesis goes along with well-described changes in cellular morphology, starting with ADM as a key event prior to PanIN development [17, 29, 38]. The fact, that mADM development was substantially reduced in *Rac1* deficient mice underlines the necessity of Rac1 for the very first metaplastic events in the acinar cells. Moreover, the elevation of Rac1 overexpression in the pancreas correlated with augmented EGFR signaling and therefore with increased carcinogenesis as reported for this model [22]. These findings suggest a stepwise raise of Rac1 protein laevel following the development of preneoplastic lesions of mPDAC. Consequently, not only the development of invasive high-grade mPanINs but also that of aggressive pancreatobilliary mIPMN lesions was drastically impaired following Rac1 deletion. These observations imply that Rac1 has a central role in the development of mPDAC and is not easily bypassed, since also no differences in the expression of Ras-dependent effectors or genes of the Notch and Hedgehog pathway were found. However, the existing lesions showed Cre-mediated recombination as proven by analysis of microdissected areas. A possible explanation for mPanIN development in the analyzed models would be through a mADM-independent route from yet unknown alternative preneoplastic cell. Unfortunately, it is still completely unclear from which cell of origin IPMNs derive. The notice, that deletion of Rac1 drastically impaired and possible changed the route of mPanIN and mIPMN development is very interesting and opens new questions in the research field of mPDAC.

Besides activation of oncogenic Kras mutations, additional signals are thought to be required for preneoplastic precursor development such as inflammation-induced reprogramming of acinar cells [30, 31, 40]. A significant reduction, yet not a complete abrogation, of mADM was noted during acute cerulein-induced pancreatitis. This observation suggests that Rac1 may play a predominant role in Ras-dependent regulation of acinar plasticity, whereas cerulein-induced induction of ADM might depend on additional pathways such as EGFR and/or EGFR-downstream signaling events [36]. Still, these results are in line with a recent study showing attenuation but not abolishment of cerulein-induced pancreatitis due to the chemical Rac1 inhibition [106]. Furthermore, Binker *at al.* showed that blocking Rac1 activation by selective compound NSC23766 inhibited Rac1 translocation from cytoplasm to the membrane of acinar cells, a process necessary for actin rearrangements. The actin cytoskeleton was previously described to play an important role in acinar cells including mediation of exocytosis, secretion and modulation of cell shape [156]. In accordance with this findings, a profound loss of cellular polarity was present in cerulein-induced pancreatitis as well as in *Kras*^{G12D}-activated cells undergoing preneoplastic transdifferentiation correlating therefore with the increasing metaplasia. Furthermore, the similarity in phenotype of *Rac1*-deficient and chemically actin-disrupted cultured acinar cells regarding ADM suggests that this axis plays a finely tuned role in acinar cell morphology. Thus, a model for F-actin redistribution during ADM (Fig. 14C) was proposed, where increasing ADM-dependant cytoskeletal changes require Rac1 overexpression and/or activation.

Pancreatic carcinogenesis is closely associated with abundant desmoplastic stromal reaction accompanying the neoplastic process [157]. The two major active stromal compartments comprise of cancer-associated fibroblasts (CAFs) and recruited inflammatory immune cells, both supplying growth factors, matrix remodeling components, ROS and other bioactive molecules variously influencing cancer cell proliferation and survival [158]. Recently, Erez N. and colleagues associated CAFs surrounding hyperplastic lesions with recruitment of inflammatory immune cells into the neoplastic regions of murine pancreatic as well as squamous cell carcinoma [58]. Moreover, a proinflamatory gene signature was identified in CAFs, which can be abolished by Nf-kB inactivation. The findings of this study revealed a great importance of Rac1 in the development of stromal reaction during PDAC development. Thus, early and late stage murine and human PDAC showed abundant Rac1 expression in the stroma, whreas pancreas-specific deletion of *Rac1* led to an almost complete lack of smooth muscle actin positive and therefore active fibroblasts as proven in the *CKR$^{fl/fl}$* model. Consequently, a profound reduction of inflammatory cell infiltrate was noted which persisted through adulthood. Additionally, in accordance with almost absent stromal reaction, the expression of a proinflammatory gene signature found by Erez *et al.* was substantially reduced in pancreatic tissue with Rac1 deletion. These findings suggest that Rac1 may play a crucial role in cell-cell cross talk and initiation of inflammatory reaction during pancreatic preneoplasia. Indeed, the predominant role of Rac1 in the accumulation of myofibroblastic hepatic stellate cells and subsequent development of liver cirrhosis was recently proven in a rat model [159].

Moreover, the regulatory link between Rac1 and lack of mPDAC development may also be hidden in IL-6/Stat3/Socs3 trans-signaling. Recently, this pathway was identified as very important determinant for the development of mPanIN and inflammatory response in murine models of PDAC [96]. Besides, all IL-6/Stat3/Socs3 genes are known to be modulated by Nf-kB signaling [160]. Inhibition of Rac1 as well as its major activator VAV1 were shown to directly impair Nf-kB activity, proliferation and malignant transformation in human lung [161] and pancreatic [93] cancer cells, respectively. Furthermore, several *in vitro* studies revealed a direct connection between Rac1 and Stat3 activation [99, 100]. Thus the relation of Rac1/Nf-kB/Stat3 and their direct or indirect connection to each other opens new questions in the field of pancreatic research and may provide important insides of the origin of PDAC associated stromal reaction. However the role of Rac 1 in the inflammatory setting appears to be controversial: while deletion of Rac1 in *CK* and *CKP$^{mut/wt}$* models resulted in a prominent reduction of inflammatory response following absence of preneoplastic lesions, pancreata of *CKTR$^{fl/fl}$* animals revealed substantially increased inflammation and development of chronic pancreatitis. As mentioned before, Rac1 may play a more important role in Ras-dependent regulation of acinar plasticity, whereas additional pathways such as EGFR and/or EGFR-downstream signaling events may be independent of Rac1 [36].

In addition, Rac1 plays an important role as inflammatory modulator not only in cancer setting. In accordance with previously published findings of chemical Rac1 inhibition [106], deletion of Rac1 in a cerulein-induced model of acute pancreatitis markedly delayed all signs of the disease such as edema, inflammatory infiltration and acinar cell damage. This observation may be explained by a connection of Nf-kB signaling and Rac1 activity in the acinar cells during pancreatitis. Indeed, Treiber *at al.* recently reported a necessity of RelA/p65 for protection of acinar cells against the damage through chronic inflammation [162]. Another publication of the same group, lead by Alguel H. further underline curtail role of Nf-kB signaling in the protection of acinar cell against damage during cerulein-induced acute pancreatitis [163]. Furthermore, Binker at al. have not followed regeneration period of caused acute pancreatitis. Interestingly, 72 hours after last cerulean injection inflammatory reaction increased in pancreata lacking Rac1. A likely explanation for this

observation may be an involvement of proinflamatory cells derived from distant compartments, which may cause a delayed infiltration of the inflammatory cells into the pancreas. Thus, Treiber *at al.* reported an involvement of rather myeloid and not pancreatic cells into the generation of fibrosis in a mouse model of chronic pancreatitis [162]. Consequently, these findings additionally underline the assumed relation of Nf-kB axis and Rac1 signaling and may explain the observed protective effect in Rac1 lacking acinar cells. The suggested myeloid origin of infiltrating cells during acute pancreatitis stands in correlation with recent findings and opens new interesting questions regarding the connection of pancreas regeneration and Rac1 effectors.

Taken together, this work uncovered Rac1 as a crucial determinant of the development of preneoplastic lesions, accumulation of the surrounding stroma and cancer progression in the murine pancreas. Although Rac1-dependent regulation of the actin cytoskeleton is well documented, most studies were performed *in vitro* using overexpression of dominant-negative or constitutively active mutants in cultured cells leaving the functional role *in vivo* undefined. The finding of Rac1-dependent basolateral actin redistribution in pancreatic acini *in vivo* as well as in 3D cultures reveals a clear evidence for an important functional role of physiologically expressed Rac1 in this process. Moreover, a model of actin polymerization as central determinant of acinar cell plasticity and metaplastic transdifferentiation during carcinogenesis was proposed. Consequently, metaplasia and inflammation associated stromal changes appear also to be Rac1 dependent. Thus, modulation of Rac1 activation and actin/stroma regulation is a potentially promising new target to interfere with the initiation of pancreatic carcinogenesis.

4.2 Inhibition of Rac1 activity by EHT1864 reveals strong synergism with Gemcitabine *in vitro* and causes necrosis *in vivo*

Pancreatic cancer is notoriously resistant to chemical and radiotherapies. Several studies underlined recently the importance of stroma density and interstitial pressure for the functional vascularity and therefore drug delivery in human and murine PDAC. Thus, K. P. Olive and colleagues demonstrated a better delivery of the standard agent of care Gemcitabine, higher vascularity and prolonged survival in animals receiving stroma remodeling agents such as IPI-926, a Smoothened inhibitor [43]. Following work by Jacobetz at al. and Provenzano at al. proved efficacy of PEGPH20, a pegylated human recombinant PH20 hyaluronidase, for the reduction of interstitial pressure and reexpansion of the microvasculature in the murine PDAC [164, 165]. However, according to the report at the 2012 AACR conference “Pancreatic cancer: Progress and Challenges” by Dr. K. P. Olive, the clinical trial conducted using Smoothened inhibitor failed to improve overall survival of patients with pancreatic cancer. Hence, development of novel therapeutic strategies using standard therapies and/or new agents is still the main goal of the pancreatic cancer research community. As previously discussed, Rac1 is highly expressed in stromal compartment of murine and human PDAC and deletion of Rac1 has a clear cancer preventive effect in mPDAC. Thus, chemical inhibition of Rac1 activity in a cancer setting was proposed as a possible therapeutic option.

Although cancer cell culture platforms do not completely recapitulate the complex *in vivo* conditions, due to the isolated microenvironment without such important factors like tumor stroma interactions and subsequent immune response as well as lacking adequate pharmacokinetics, they can be very well used in the preliminary high through put testing of new therapeutic regiments. In this project, both NSC23766 was proven to be the effective to cause cancer cell death alone as well as in combination with Gemcitabine. More importantly, NSC23766 was very effective on the Gemcitabine resistant cell lines, however has not impaired growth of the normal

cells, suggesting its feasibily, and low side effects for *in vivo* studies. These findings are in agreement with recently published studies on breast cancer cell lines, where especially trastuzumab resistant cells responded to NSC23766 treatment [81] and immortalized normal mammary gland cells remained vital and proliferating [105]. The proposed mechanism of action following inhibition of Rac1 activation was an induction of G1 cell cycle arrest in retinoblastoma expressing cell lines, as well as apoptosis in Rb-deficient cell lines [105]. Moreover, in accordance with the above-mentioned hypothesis in GEMMs NF-kB, but not c-Jun NH_2-terminal kinase or p38 pathways were responsible for Rac1-mediated survival signaling [105]. This hypothesis break open new interesting research directions investigating in the role of Rac1 in the survival of pancreatic cancer cells.

Following a new report that a second more effective selective inhibitor of Rac1 function was developed [110], EHT1864 was established as more effective agent in comparison to NSC23766 especially in confluent cell culture conditions, which resemble the tightly packed tumor more faithfully. A possible explanation for the observed benefit of EHT1864 is the fact that EHT1864 inhibits Rac1 activation by all GEFs through a direct binding to Rac1 and subsequent induction of nucleotide release and inhibition of nucleotide binding [110]. In contrast, NSC23766 only blocked Rac1 activation by two specific GEFs Tiam1 and TrioN, however was inactive against Vav1 [104], a very important GEF in PDAC [93].

Since, both of the available inhibitors of the Rac1 function revealed promising results in mPDAC cell lines, a pilot *in vivo* study in the proposed *CKP$^{fl/fl}$* model was of great interest. NSC23766 was shown twice to be a potent therapeutic anticancer agent in transplanted mouse models of BCR-ABL-induced chronic myelogenous leukemia (CML) and acute myeloid leukemia (AML), where it inhibited Rac1 activation and engrafting of CML-transplants as well as significantly prolonged survival of stably transplanted NOD/SCID mice [107, 108]. In addition, another study reports that NSC23766 inhibited maintenance and expansion of both normal as well as leukemic stem/progenitor cells by mediating their interaction with stromal cells [109]. EHT1864 has only been proposed as anticancer agent in *in vitro* studies [105, 110], however a good inhibition of Rac1 activity in the kidney of C57BL/6J mice through s.c. treatment with EHT1864 was recently published [166]. The small pilot *in vivo* study indicated feasibility of both inhibitors *in vivo* and revealed a possible antitumor activity of EHT1864, since partial necrosis was observed in both treated animals. However, only two animals were subjected to EHT1864 treatment. Moreover, no survival study was performed. In addition, based on the results obtained *in vitro*, especially the combinatorial therapy regiment of EHT1864 together with Gemcitabine would be of interest to test *in vivo*.

Taken together, inhibition of Rac1 activity by EHT1864 has shown promising results as detected *in vitro* and *in vivo*. However, due to the limited study size, further studies need to be planned and conducted in order to predict and thoroughly investigate the efficacy of Rac1 inhibition of the treatment of murine PDAC.

4.3 Qualitative and quantitative characterization of murine endogenous pancreatic cancer using MRI- and PET- based imaging platform

Given the high failure rate of the new, preclinically successful drugs in subsequent clinical trials [167, 168], the scientific world is constantly searching for better, more predictive platforms for testing of new therapeutics [169]. In mPDAC, *Kras^{G12D}*-based GEMMs are widely used not only to answer basic research questions such as whether or not the gene is involved into mPDAC development or maintenance [20, 70, 170], but also for cancer preventions as well as preclinical treatment testing trials [42, 43, 46, 169]. Moreover, qualitative and quantitative imaging modalities, such as high resolution

ultrasound, DCE-MRI and PET, widely established in the clinical praxis are recently becoming more and more transferred into the animal research [42, 43, 84, 164, 165, 171]. Although implicated for specific questions, neither the used endogenous models nor available imaging modalities were thoroughly characterized for their heterogeneity and applicability in the preclinical praxis. Consequently, this project aimed to comprehensively evaluate in our lab available GEMMs using MRI-based modalities and PET as a platform for preclinical studies.

4.3.1 Heterogeneity of murine pancreatic cancer and the right choice of preclinical model

Heterogeneity is an important hallmark for pancreatic cancer [12] and has to be taken into account while conducting clinical trials. Preclinically, most researchers employ a well established pancreatic cancer model based on pancreas specific endogenous over-activation of the proto-oncogen $Kras^{G12D}$ (*K*) and mutation or deletion of one allele of the tumor suppressor gene TP53 ($P^{mut/wt}$, $P^{fl/wt}$) via a *Pdx1-Cre* (C) system [43, 164, 165, 171]. All these models were described to develop poorly differentiated G3 tumors with strong desmoplastic reaction between 3-10 mounts of life. However, clinically important preneoplastic lesions like IPMNs [15] cannot be followed in these models. In addition, models for higher differentiation grade of mPDAC as well as cancer of acinar origin are needed to cover the wide spectrum of human disease [12]. In this work described models developed a broader range of murine pancreatic cancer including not only mPanIns, mIPMNs, G1-G3 differentiated mPDAC with different stroma content but also sarcomatoid, anaplastic tumors as well as acinus cell carcinomas, allowing a wider mPDAC investigation in comparison to published studies. Interestingly, the highest tumor variability was observed in TGFa-overexpressing aniimals, suggesting a strong involvement of EGFR signaling into development of heterogeneity in pancreatic cancer. Indeed, EGFR activation has ben reported to be one of the first crucial genetic events during emergence of pancreatic cancer in humans [7] and mPDAC development [172]. Although certain genotypes revealed a clear trend in the occurence of distinct lesion types, most animals presented with at least two and up to five different histological lesions within the pancreas of the same animal. Moreover, in some genotypes a likelihood of tumor composition correlated with the position of lesions. Thus, in the $CKP^{fl/fl}$ model more differentiated tumors were found in the pancreas head and tail, whereas lower grade of differentiation was observed in the neck and the body. The strong interindividual heterogeneity even within the same genetic background can possibly be explained by secondary genetic events that occur in growing cancer. In summary, two conclusions can be made using this knowledge: 1. Presented GEMMs not only faithfully recapitulate a wide spectrum of genetic alterations but also a broad range of histopathology found in human pancreatic cancer. 2. A more careful histopathological classification of the cancers developed in GEMMs is necessary for meaningful stratification of preclinical models.

Genotype-based characterization of tumor onset, latency and growth kinetics revealed an enormous heterogeneity between genotype groups as well as single individuals characterized in this study. This observation underlines the importance of model choice for preclinical therapy testing. Indeed, a GEMM used for preclinical trials should match certain criteria such as high tumor penetrance, reasonable latency as well as relatively predictable tumor onset. For one, models that have very quick developing tumors might not accurately mimic the complex interplay of cancer cells and their microenvironment seen in human situation. On the other hand, models with too long latency and wide range of tumor onset are impractical and make therapeutic assessments very difficult. In this work, two of the chosen models - $CKTP^{mut/wt}$ and *CKT* - appear to be less suitable for preclinical trials because they failed above named criteria. Although all animals with these genotypes eventually developed mPDAC, very variable tumor onset,

extremely long latency, slow tumor growth kinetics proven by volume analysis and sudden death of non-cancer related causes underline inefficiency of these models for big scale trials. In contrast, corresponding to published reports [43, 164] *CKP*$^{fl/wt}$,*CKTP*$^{fl/wt}$ and *CKP*$^{fl/fl}$ animals presented with pancreatic cancers of a reasonable latency (1 - 4 weeks) and moderate to high increase in volume (2 - 6 times) over the time until death. Similar to others, a very variable tumor onset was observed in the *CKP*$^{fl/wt}$ group, making this genotype less handy for preclinical purposes. However, *CKTP*$^{fl/wt}$ and *CKP*$^{fl/fl}$ models meet all of the criteria important for preclinic. Moreover, the differences between both models allow for more sophisticated preclinical approaches using each model for a particular study design. Thus, a quick assessment of general efficacy of a new therapeutic agent could be more easily done using the *CKP*$^{fl/fl}$ model, since it showed the most homogeneous histological appearance, the shortest time to tumor onset, and latency of 1 - 4 weeks. However, animals of this model only rarely develop metastases and do not present with mIPMNs. Thus, further studies on heterogeneous tumors using efficient agents may be performed in *CKTP*$^{fl/wt}$ animals. The unique features of this model and bigger size of the animals could be used for validation of multiple imaging modalities as surrogate therapy monitoring markers as well as the elucidation of certain mechanistic questions of the new drugs. Moreover, the possibility of performing preclinical trials on different tumor types within the same animal represents a new valid approach for the individualized therapy efficacy monitoring.

4.3.2 Anatomic and functional imaging of mPDAC using MRI and PET

Pancreatic cancer is an abdominal disease which detection is complicated by several factors [127]. Also, preclinical cancer models, which faithfully recapitulate the human situation suffer from similar problems: the tumor onset is mostly very variable, they are not easy to palpate at the early stage and animals show seldom signs of sickness prior to an very advanced phase (personal observation). Therefore, sophisticated and well-established imaging modalities are necessary for tumor detection and therapy monitoring while performing preclinical studies. High-resolution micro-ultrasound was widely used in recently published reports [43, 164, 165, 173]. However, the relatively poor special resolution of this technique does not allow distinguishing different lesions within the same tumor as well as detection of metastases. High field and therefore high-resolution 9.4T or 7T small animal MRI scanners also were reported to be applicable for tumor detection in orthotopically transplanted [174] and endogenous [43, 175] mPDAC. Yet, such special equipment is rarely accessible and very expensive in purchase and maintenance. In contrast, clinical 1.5T or 3T MRI systems are widely available in clinical praxis of several cancer centers and could be well used for *in vivo* preclinical trials in small rodents in combination with a wrist coil or dedicated small animal surface coil [176-178]. In addition, motion artifacts caused by breathing of the animal could be reduced using a MRI scanner of lower field strength and preclinical protocols could be more easily transferred into the clinic. Therefore, in this study the applicability of an MRI-based platform using clinical 1.5T MRI system was tested for abdominal mouse imaging. The established T_2-weighted turbo spin echo sequence (T2w) allowed robust identification of solid tumors mass as well as differentiation of mIPMN, predominantly preneolastic heterogeneous areas and metastases of certain cize. Although anatomicaly distinct tumor regions were clearly visible on the T2w-images, exact distinction of tumor grade was not possible within the reasonable scanning time and required more sophisticated methods (e.f. DWI, see below). However, a good signal to noise ratio and reasonable contrast of the applied sequence allowed clear tumor rim delineation that could be used for relatively exact volume calculation. Consequently, this work proves a very good applicability of 1.5T clinical MRI scanner for detection of murine endogenous pancreatic cancer and future preclinical studies.

Change in tumor volume is still one of the most recognized readout parameters for therapy monitoring according to the Response Evaluation Criteria In Solid Tumors (RECIST). Thereby it is of high importance to distinguish viable solid tumor parts from necrotic dead areas, especially in studies testing cytotoxic agents. Tumor volume of previously widely used in preclinical studies s.c. transplanted models could be monitored by caliper-based technique. Endogenously growing mPDACs require more sophisticated imaging techniques for volume analysis [169, 179]. High resolution ultrasound [43, 164, 165, 173] as well as T2w-MRI [174-176, 178] were used in several preclinical studies to determine tumor volume of mPDAC. However, none of these studies implicated a volume correction for tumor necrosis and/or possible cystic tumor parts that can be frequently developed in either of models. In this study a prominent development of necrosis and intrapancreatic cysts were observed to a different extend in all characterized phenotypes. Thus, an in-house written post-processing software was developed and successfully implemented in order to exclude/deduce cystic/necrotic partial volume effects while conducting volumetric analyses. Moreover, the use of the above-mentioned technique revealed that only one model - $CKP^{fl/fl}$ - appeared to develop tumors mostly free of necrosis, in contrast to the well established $CKP^{fl/wt}$ and new characterized $CKTP^{fl/wt}$ models. This finding is of great value for the planning of future preclinical therapy trials, since the quantification of tumor necrosis may be used as a sensitive marker for therapy response [176]. An exact quantification of the pre-treatment as well as the drug-induced necrotic part would lead to a correct judgment of therapeutic efficacy. This method would be of most use for testing new cytotoxic agents that do not reduce tumor size, however lead to a so called “cold tumor” with a large central necrosis.

Anatomical assessment of human PDAC, especially a clear delineation of tumor borders and/or adjacent mass forming pancreatitis from a healthy pancreas is still difficult using only T2w imaging. Therefore, functional MRI-based imaging techniques such as diffusion weighted (DW) and dynamic contrast-enhanced (DCE) MRI as well as [^{18}F]-FDG or [^{18}F]-FLT PET are increasingly used in daily clinical praxis of mPDAC detection and characterization [124, 127, 180].

DW-MRI has the ability to depict such important biological tumor features as cellularity, relative grade of fibrosis or stroma and vascularity, since those are all factors influencing free water movement detected by DWI. There were several attempts to use DWI as a qualitative marker for tumor characterization in human pancreatic cancer. Most studies on human PDAC patients found a significantly lower ADC value for cancer tissue compared to normal pancreas or benign lesions [181-184]. Thereby both Ichiikawa at al. as well as Kartalis at al. were able to detect solid malignant lesions with a very high specificity and sensitivity of more than 96%, using high b-value DWI. However, only very few DW-MRI studies in animal models of pancreatic cancer (orthotopically transplanted) were published [185, 186]. Although promising result of tumor detection as well as early therapy response monitoring using DW-MRI were presented in these and other studies (ortotopically transplanted rat HCC [176] and rhabdomyosarcoma model [177]), this method has not been applied for endogenous mPDAC detection. Therefore, in this work, a comprehensive DWI-MRI analysis of all five characterized endogenous models was performed.

The established single shot multi-slice DWI sequence with three b-values (b20, b200, b600) allowed a reasonable image quality acquisition. Highly cellular regions were reliably distinguished from low cellularity areas on the ADC-map. However, image distortion due to the abdominal air and berating artifacts were still present in some examinations, reflecting current animal health status. These findings are in agreement with the studies on human PDAC patients mentioned above. Moreover, a strong relationship of calculated ADC value and tumor histology was further proven by a negative correlation between ADC value and cell density as well as a positive correlation between ADC value and collagen fiber content. Interestingly, Muraoka et al. report a

negative correlation of collagenous fibers and ADC values in human PDAC pancreas [183]. This discrepancy could be explained by the fact that human PDACs analyzed by Muraoka et al. revealed similar content of nuclei and differed only in the fibrosis grade. Unfortunately, it was not possible to make this kind of analysis in our work, due to the absence of such examples. Histological classification of all murine tumors revealed a four groups pattern depending on cellular content, amount of ductal structures and stroma. Calculated ADC values of all four groups showed significant differences, further underlying high robustness of the DWI measurements. More importantly, heterogeneous regions within the same animal could be easily identified using DW-MRI. Also uncertainties, due to the overlapping of the mean value could be resolved by histogram analysis of respective regions. Thus, this work presents a very reliable, comprehensive characterization of various histological subtypes of endogenous mPDAC. An attempt of similar evaluation of human pancreatic carcinomas could further unravel specific characteristics of pancreatic abnormalities and therefore substantially help radiologists and surgeons with diagnosis and treatment of this lethal disease.

DCE-MRI with small molecular weight gadolinium chelates as contrast agents is a widely established technique for anatomical diagnostic of abdominal malignances [117, 127]. Due to the severe abnormality of the vascular structures in the tumor, contrast agents tend to accumulate in the lesions, so they appear hypo-intense compared to adjacent normal tissue [117]. In addition, depending on the method, DCE-MRI may be used as functional imaging method and provide information about tumor microvasculature and extracellular space. Recently, Bali at al. showed a significant correlation between histopathological and DCE-MRI derived quantitative parameters for malignant and non-cancerous lesions of human PDAC [117]. Thereby, malignant tumors revealed significantly lower transfer rates between vascular and interstitial space (K^{trans}) compared with benign lesions. In addition, K^{trans} was negatively correlated with the amount of fibrosis in the lesion. Similarly to this, Olive *et al.* showed that fibrotic endogenous mPDAC in $CKP^{mut/wt}$ (*KPC*) model is scarcely perfused compared to the tumor adjacent regions [43]. Although, no quantitative analysis was done in this study, the qualitativly lower perfusion rate measured by ultrasonography and DCE-MRI was correlated with dysfunctional vasculature in endogenous mPDAC. Therefore, a detailed DCE-MRI analysis of different mouse models of pancreatic cancer may allow further stratification of the tumor type, a useful feature for preclinical studies.

To analyze perfusion status in the five endogeneous mPDAC models used in this work, a previously described fast single-shot Look-Locker based radial T1 mapping technique was established in combination with the low molecular weight contrast agent Gd-DTPA [176]. Alternativly to the standard dynamic T1-wighted gradient echo sequence [187] this method has a low sensitivity towards motion and flow artifacts allowing imaging under free breathing conditions in adequate temporal resolution. However, only single slice T1 mapping could be performed, requiring exact positioning of the acquisition slice in serial imaging sessions. The acquired data was analyzed using reference region based pharmacokinetic model, in order to avoid systemic error introduced by different age and health state of the animals [149]. Corresponding to the studies on human PDAC, a lover perfusion rate was found in solid cancer regions compared to the adjacent preneoplastic areas. To our knowledge no perfusion values were published for endogenous mPDAC models. In this work, the calculated iAUC90 values revealed no significant differences between the analyzed genotypes. However, in agreement with published findings, $CKP^{fl/wt}$ animals that correspond to the $CKP^{mut/wt}$ (*KPC*) model revealed a trend to a lower perfusion in comparison to all other groups. Recent publications confirmed that mPDACs from $CKP^{mut/wt}$ mice showed a very high interstitial pressure due to the abundant stromal desmoplasia and collapsed vasculature [164, 165]. Moreover, here presented study shows that a more careful analysis of

heterogeneous tumor parts within the same animal is possible and necessary in order to characterize different mPDAC models and establish the DCE-MRI method as sensitive pharmacokinetic parameter. Thus, the example analysis of heterogeneous tumor revealed hardly any perfusion in the lesion, completely lacking any stroma. In contrast, mPDAC with strong desmoplastic reaction appeared vital and revealed a higher amount of functional vessels (data not shown, ongoing investigation). The observed very high inter-individual differences in the iAUC90 indicate that further carful analysis including *CKP*$^{mut/wt}$ tumors are clearly needed to address such important aspects of mPDAC tumor biology as correlation of perfusion parameters with cellular, fibrotic and vascular content of different histological regions of pancreatic cancer.

Finally, [^{18}F]-FDG and [^{18}F]-FLT PET tracers, routinely implicated in the clinic for diagnostic of PDAC were tested in several mPDAC models. Both tracers were repeatedly shown as highly sensitive tools for detection of human pancreatic cancer ([^{18}F]-FDG 92-96%, [^{18}F]-FLT 70%) [124, 125, 188]. Although [^{18}F]-FLT PET was less sensitive, it showed a higher selectivity (75%) than [^{18}F]-FDG PET (50%) [188]. A state of the art small animal PET system was used for imaging of [^{18}F]-FDG and [^{18}F]-FLT uptake. Due to the low soft tissue contrast of PET-CT, image fusion with T2w-MRI was routinely required for the integration of data from the individual imaging modalities. Murine PDAC revealed 100% sensitivity and specificity for [^{18}F]-FDG tracer uptake. Moreover, a cut-off of 3 for tumor-to-muscle ratio was proposed for differentiation of preneoplastic lesions such as mIPMN and mPanIN from solid neoplasia. To our knowledge this is the first time quantitative PET analysis was performed in GEMM of PDAC. A similar qualitative detection of preneoplastic lesions and mPDAC was published by Fendrich et al. in the *CKP*$^{mut/wt}$ (*KPC*) model [143]. In addition, liung and liver metastases could be reliably detected via [^{18}F]-FDG PET, presumed that they reached a certain size detectable by MRI. Interestingly, although accumulation of [^{18}F]-FDG in inflammatory regions e.g. during chronic pancreatitis is a well known limitation of its sensitivity for mPDAC detection [189], no such problems were observed in analyzed mouse mice models of pancreatic cancer. A very high inter-individual variability of T/M rations may result from intrinsic metabolic characteristics of particular tumor and/or the well-established heterogeneity of the analyzed cancers. Thus further analysis of comprehensive correlation of histology and calculated [^{18}F]-FDG values are necessary in order to confirm the applicability of this tracer for preclinical studies.

Surprisingly, no significant [^{18}F]-FLT uptake was observed in all tested models, with the exception of a sub-region of a single animal. The positive [^{18}F]-FLT region was histologically classified as a highly proliferative anaplastic mPDAC. These findings stand in contrast to previous observations made in human cancer patients [125, 188, 189], suggesting differential expression rate of the thymidine kinase-1 [190] in mPDAC is tumors compared to human cancer. Although more animals with anaplastic carcinomas were enrolled into the study, for technical reasons they have not been subjected to [^{18}F]-FLT PET. Thus, the questions why mPDAC id not sensitive to [^{18}F]-FLT uptake despite a high proliferation rate and whether [^{18}F]-FLT may be a sensitive marker for the detection of anaplastic mPDAC remain unclear and require further investigations.

Taken together, the need for preclinical PDAC tumor models of high predictive value for diagnostic and therapeutic tests was stated manifold in recent publications [127, 169]. High-resolution ultrasound was used as the main method for tumor detection and volume monitoring. The here presented data extend the spectrum of non invasive mPDAC imaging by further methods that provide not only MRI derived anatomical information but also allow comprehensive characterization of mPDAC heterogeneity and functionality. These include differentiation of tumor development and composition, perfusion and metabolic status.

4.3.3 Therapy response monitoring and future outlook.

Several steps have to be taken in order to declare an *in vivo* model or a method as predictive for response in preclinical drug testing. The first investigation leading in this direction is to validate the new methods in an established model. Therefore, therapy response parameters such as volume, $iAUC_{rel}$, and [^{18}F]-FDG PET were initially tested in s.c. transplanted and than in endogenously developed models of murine pancreatic cancer using the standard of care therapy Gemcitabine.

The data revealed, that solid tumor volume as marker for growth kinetics, detected by MRI reliably identified changes caused by therapeutic agent. Moreover, reduced growth rates were already reported for Gemcitabine treated animals with s.c. transplanted tumors [43]. Also the significant tumor growth reduction in endogenous *CKT/CKTP$^{fl/wt}$* models under the Gemcitabine treatment proves that tumor volume could be used as reliable therapy monitoring read out parameter in endogenous mPDAC. However, the low sample size and large heterogeneity in tumor growth characteristics as well as histology in these models raise a question if Gemcitabine could thruly cause this prominent change. Indeed, Gemcitabine treatment only marginal influenced mPDAC development in more homogeneous *CKP$^{fl/fl}$* model, correlating with recent studies [43, 164, 165]. Nevertheless, these studies use the same *CKP$^{mut/wt}$* model and report high interstitial pressur in the tumor to be the cause for low efficacy of Gemcitabine. Since, *CKT* tumors could grow slowlier than *CKP$^{mut/wt}$* possible differences in the tumor tissue composition and therefore interstitial pressur may explain the observed responsiveness in the present study. Therefore, comprechensive comparison analysis of tumors derived from different genotypes including established models are still necessary in order to depict tumor heterogeneity while Gemcitabine treatment.

Increasing evidence suggests, that size assessments have significant limitations as pharmacodynamic marker while therapy monitoring, especially for lesions that persist following treatment [191]. [^{18}F]-FDG PET was successfully used for the evaluation of metabolic status during therapy in several cancers [192, 193]. In this work, [^{18}F]-FDG uptake in the s.c. transplanted tumors was significantly reduced in the Gemcitabine treated cohort verifying the possible applicability of this method for the assessment of therapy response. Nevertheless, the use [^{18}F]-FDG tracer in the pilot endogeneous mPDAC study revealed no significant variances between the groups. As discussed above, high intratumoral pressure may be the cause for poor responsiveness of mPDAC to Gemcitabine. Thus, not the sensitivity of the read out method but the inability of the therapeutic agent to cause a change in the nmetabolic status of the tumor may be the reason for the observed results. Still, this study suggests at least some sensitivity of [^{18}F]-FDG uptake as a preclinical read out parameter, since none of the Gemcitabine treated tumors increased [^{18}F]-FDG uptake like the non-treated individuals. To our knowledge, no therapy trials in small animals using [^{18}F]-FDG PET were published, revealing the novelty of this observation. However, the ability of [^{18}F]-FDG to detect response in endogenous models still has to be further tested and is currently under investigation.

Dynamic contrast enhanced MRI is one other functional imaging method that could be used for therapy response assessment [194]. Studies of human pancreatic cancer revealed that DCE could detect perfusion changes following antiangiogenic combination therapy of sorafenib and Gemcitabine [195]. Also murine models of PDAC showed sensitivity to sunitinib therapy, an angiogenesis inhibitor, measured by microbubble contrast enhanced ultrasound imaging [171]. Here, DCE-MRI analysis revealed no significant change of perfusion in s.c. transplanted model of mPDAC. Therefore, DCE-MRI has not been further tested in the endogeneous GEMM of PDAC.

Interstingly, Casneuf *et al.* observed an increased perfusion in s.c. transplanted human Panc02 tumors after 7 days of Gemcitabine treatment [196]. However, this response was only transient and disappeared after 14 days of treatment correlating with our messurements after 10 days of treatment. This finding is in agreement with recent studies, where quantification of microvascular density in $CKP^{mut/wt}$ tumors under Gemcitabine therapy revealed only a slight tendency to more intact vasculature compared to the controle groupes [102, 164, 165]. Nevetheless, combinatorial studies with Gemcitabine and Shh inhibitor IPI-926 or PH20 hyaluronidase PEGPH20 in mPDAC revealed a dramatic increase in functional vascularity measured by histological analysis [196]. Unfortunatelly, no quantitative perfusion messurements were stated. These reports indicate that perfusion changes DCE-MRI could be a potent therapy monitoring parameter, assuming the therapeutic agent changes tumor vascularity.

In addition, a tird very promisisng method for the assessment of tissue compositin in preclinical and clinical studies is a diffusion weighted MRI. The feasibility of DWI-MRI for early therapy response evaluation was reported in several human studies of various cancers [194, 197]. Moreover, a recent conference report revealed the applicability of DWI for testing chemotherapies in PDAC [180]. In preclinical studies implicating rodent models DWI was shown to detect early apoptotic changes caused by Gemcitabine alone as well as in combination with TRA-8 antibody in an orthotopic mPDAC xenotransplant model, using a 9.4T small animal MRI system [186]. Here presented work has not revealed any significant changes in ADC values measured in endogeneous models following Gemcitabine treatment. On the one hand, this finding may reflect differences between xenograft and endogenous models, as published recently [43]. On the other hand, the time points of analysis differ between the study of Kim *et at.* and this study. It is possible; that Gemcitabine causes only a thansient response that can be detected on day 3 after the beginning of treatment, however desapears later as reported here (day 7-14). Indeed, timing of analysis is a major question while conductiong DWI-studies. Thus, transient (day 3) as well as permanent development of necrosis could be detected in presented here preliminary study with Rac1 activation inhibitor EHT1864. Thereby a slice based histogram analysis and not the mean ADC value revealed the most information of changes in tumor composition. Thus, ADC values could be a potentially sensitive parameter for changes of tissue composition upon treatment and identify single responders. However, it remains to be shown, whether less profound effects on tumor biology can be monitored in a similar manner in endogenous mPDAC models.

Taken together, four noninvasive MRI and PET based imaging modalities were evaluated in this study using s.c. transplanted and endogenous model on mPDAC. Although all methods were found applicable to a different extend for identification of tumor heterogeneity as well as therapy-induced changes, DW-MRI and therof calculated ADC represent the most sensitive and selective parameter for pancreatic cancer imaging. Nevetheless, due to the small number of animals especially in therapy response studies further validation using larger cohorts and more homogeneous model, e.g. $CKP^{fl/fl}$ are necessary inorder to finaly validate all the parameters as reliable tumor response monitoring biomarkers.

5. References

1. Ferlay J, Autier P, Boniol M, et al. Estimates of the cancer incidence and mortality in Europe in 2006. Ann Oncol 2007;18:581-92.
2. Jemal A, Center MM, DeSantis C, et al. Global patterns of cancer incidence and mortality rates and trends. Cancer Epidemiol Biomarkers Prev 2010;19:1893-907.
3. Jemal A, Siegel R, Xu J, et al. Cancer statistics, 2010. CA Cancer J Clin 2010;60:277-300.
4. Slack JM. Developmental biology of the pancreas. Development 1995;121:1569-80.
5. Hebrok M, Kim SK, St Jacques B, et al. Regulation of pancreas development by hedgehog signaling. Development 2000;127:4905-13.
6. Kim SK, MacDonald RJ. Signaling and transcriptional control of pancreatic organogenesis. Curr Opin Genet Dev 2002;12:540-7.
7. Bardeesy N, DePinho RA. Pancreatic cancer biology and genetics. Nat Rev Cancer 2002;2:897-909.
8. Edlund H. Pancreatic organogenesis--developmental mechanisms and implications for therapy. Nat Rev Genet 2002;3:524-32.
9. Hruban RH, Adsay NV, Albores-Saavedra J, et al. Pathology of genetically engineered mouse models of pancreatic exocrine cancer: consensus report and recommendations. Cancer Res 2006;66:95-106.
10. Puri S, Hebrok M. Cellular plasticity within the pancreas--lessons learned from development. Dev Cell 2010;18:342-56.
11. Lowenfels AB, Maisonneuve P. Epidemiology and risk factors for pancreatic cancer. Best Pract Res Clin Gastroenterol 2006;20:197-209.
12. Klimstra DS, Pitman MB, Hruban RH. An algorithmic approach to the diagnosis of pancreatic neoplasms. Arch Pathol Lab Med 2009;133:454-64.
13. Hingorani SR. Location, location, location: precursors and prognoses for pancreatic cancer. Gastroenterology 2007;133:345-50.
14. Hezel AF, Kimmelman AC, Stanger BZ, et al. Genetics and biology of pancreatic ductal adenocarcinoma. Genes Dev 2006;20:1218-49.
15. Fernandez-del Castillo C, Adsay NV. Intraductal papillary mucinous neoplasms of the pancreas. Gastroenterology 2010;139:708-13, 713 e1-2.
16. Canto MI, Goggins M, Hruban RH, et al. Screening for early pancreatic neoplasia in high-risk individuals: a prospective controlled study. Clin Gastroenterol Hepatol 2006;4:766-81; quiz 665.
17. Hruban RH, Adsay NV, Albores-Saavedra J, et al. Pancreatic intraepithelial neoplasia: a new nomenclature and classification system for pancreatic duct lesions. Am J Surg Pathol 2001;25:579-86.
18. Maitra A, Hruban RH. Pancreatic cancer. Annu Rev Pathol 2008;3:157-88.
19. Hruban RH, Takaori K, Klimstra DS, et al. An illustrated consensus on the classification of pancreatic intraepithelial neoplasia and intraductal papillary mucinous neoplasms. Am J Surg Pathol 2004;28:977-87.
20. Hruban RH, Adsay NV. Molecular classification of neoplasms of the pancreas. Hum Pathol 2009;40:612-23.
21. Hingorani SR, Petricoin EF, Maitra A, et al. Preinvasive and invasive ductal pancreatic cancer and its early detection in the mouse. Cancer Cell 2003;4:437-50.
22. Siveke JT, Einwachter H, Sipos B, et al. Concomitant pancreatic activation of Kras(G12D) and Tgfa results in cystic papillary neoplasms reminiscent of human IPMN. Cancer Cell 2007;12:266-79.
23. Mazur PK, Einwachter H, Lee M, et al. Notch2 is required for progression of pancreatic intraepithelial neoplasia and development of pancreatic ductal adenocarcinoma. Proc Natl Acad Sci U S A 2010;107:13438-43.
24. Hingorani SR, Wang L, Multani AS, et al. Trp53R172H and KrasG12D cooperate to promote chromosomal instability and widely metastatic pancreatic ductal adenocarcinoma in mice. Cancer Cell 2005;7:469-83.
25. Aguirre AJ, Bardeesy N, Sinha M, et al. Activated Kras and Ink4a/Arf deficiency cooperate to produce metastatic pancreatic ductal adenocarcinoma. Genes Dev 2003;17:3112-26.
26. Izeradjene K, Combs C, Best M, et al. Kras(G12D) and Smad4/Dpc4 haploinsufficiency cooperate to induce mucinous cystic neoplasms and invasive adenocarcinoma of the pancreas. Cancer Cell 2007;11:229-43.
27. Kojima K, Vickers SM, Adsay NV, et al. Inactivation of Smad4 accelerates Kras(G12D)-mediated pancreatic neoplasia. Cancer Res 2007;67:8121-30.

28. Bardeesy N, Cheng KH, Berger JH, et al. Smad4 is dispensable for normal pancreas development yet critical in progression and tumor biology of pancreas cancer. Genes Dev 2006;20:3130-46.
29. Morris JPt, Wang SC, Hebrok M. KRAS, Hedgehog, Wnt and the twisted developmental biology of pancreatic ductal adenocarcinoma. Nat Rev Cancer 2010;10:683-95.
30. Guerra C, Collado M, Navas C, et al. Pancreatitis-induced inflammation contributes to pancreatic cancer by inhibiting oncogene-induced senescence. Cancer Cell 2011;19:728-39.
31. Guerra C, Schuhmacher AJ, Canamero M, et al. Chronic pancreatitis is essential for induction of pancreatic ductal adenocarcinoma by K-Ras oncogenes in adult mice. Cancer Cell 2007;11:291-302.
32. Gidekel Friedlander SY, Chu GC, Snyder EL, et al. Context-dependent transformation of adult pancreatic cells by oncogenic K-Ras. Cancer Cell 2009;16:379-89.
33. Carriere C, Young AL, Gunn JR, et al. Acute pancreatitis markedly accelerates pancreatic cancer progression in mice expressing oncogenic Kras. Biochem Biophys Res Commun 2009;382:561-5.
34. Carriere C, Seeley ES, Goetze T, et al. The Nestin progenitor lineage is the compartment of origin for pancreatic intraepithelial neoplasia. Proc Natl Acad Sci U S A 2007;104:4437-42.
35. Blaine SA, Ray KC, Anunobi R, et al. Adult pancreatic acinar cells give rise to ducts but not endocrine cells in response to growth factor signaling. Development 2009;137:2289-96.
36. Means AL, Meszoely IM, Suzuki K, et al. Pancreatic epithelial plasticity mediated by acinar cell transdifferentiation and generation of nestin-positive intermediates. Development 2005;132:3767-76.
37. Strobel O, Dor Y, Alsina J, et al. In vivo lineage tracing defines the role of acinar-to-ductal transdifferentiation in inflammatory ductal metaplasia. Gastroenterology 2007;133:1999-2009.
38. De La OJ, Emerson LL, Goodman JL, et al. Notch and Kras reprogram pancreatic acinar cells to ductal intraepithelial neoplasia. Proc Natl Acad Sci U S A 2008;105:18907-12.
39. Guo F, Gao Y, Wang L, et al. p19Arf-p53 tumor suppressor pathway regulates cell motility by suppression of phosphoinositide 3-kinase and Rac1 GTPase activities. J Biol Chem 2003;278:14414-9.
40. Morris JPt, Cano DA, Sekine S, et al. Beta-catenin blocks Kras-dependent reprogramming of acini into pancreatic cancer precursor lesions in mice. J Clin Invest 2010;120:508-20.
41. Siveke JT, Lubeseder-Martellato C, Lee M, et al. Notch signaling is required for exocrine regeneration after acute pancreatitis. Gastroenterology 2008;134:544-55.
42. Singh M, Lima A, Molina R, et al. Assessing therapeutic responses in Kras mutant cancers using genetically engineered mouse models. Nat Biotechnol 2010;28:585-93.
43. Olive KP, Jacobetz MA, Davidson CJ, et al. Inhibition of Hedgehog signaling enhances delivery of chemotherapy in a mouse model of pancreatic cancer. Science 2009;324:1457-61.
44. Morton JP, Karim SA, Graham K, et al. Dasatinib inhibits the development of metastases in a mouse model of pancreatic ductal adenocarcinoma. Gastroenterology 2010;139:292-303.
45. Clark CE, Hingorani SR, Mick R, et al. Dynamics of the immune reaction to pancreatic cancer from inception to invasion. Cancer Res 2007;67:9518-27.
46. Frese KK, Tuveson DA. Maximizing mouse cancer models. Nat Rev Cancer 2007;7:645-58.
47. Nakhai H, Sel S, Favor J, et al. Ptf1a is essential for the differentiation of GABAergic and glycinergic amacrine cells and horizontal cells in the mouse retina. Development 2007;134:1151-60.
48. Wagner M, Greten FR, Weber CK, et al. A murine tumor progression model for pancreatic cancer recapitulating the genetic alterations of the human disease. Genes Dev 2001;15:286-93.
49. Wagner M, Luhrs H, Kloppel G, et al. Malignant transformation of duct-like cells originating from acini in transforming growth factor transgenic mice. Gastroenterology 1998;115:1254-62.
50. Bardeesy N, Aguirre AJ, Chu GC, et al. Both p16(Ink4a) and the p19(Arf)-p53 pathway constrain progression of pancreatic adenocarcinoma in the mouse. Proc Natl Acad Sci U S A 2006;103:5947-52.
51. Zhu L, Shi G, Schmidt CM, et al. Acinar cells contribute to the molecular heterogeneity of pancreatic intraepithelial neoplasia. Am J Pathol 2007;171:263-73.
52. Shi G, Zhu L, Sun Y, et al. Loss of the acinar-restricted transcription factor Mist1 accelerates Kras-induced pancreatic intraepithelial neoplasia. Gastroenterology 2009;136:1368-78.
53. Brembeck FH, Schreiber FS, Deramaudt TB, et al. The mutant K-ras oncogene causes pancreatic periductal lymphocytic infiltration and gastric mucous neck cell hyperplasia in transgenic mice. Cancer Res 2003;63:2005-9.
54. Habbe N, Shi G, Meguid RA, et al. Spontaneous induction of murine pancreatic intraepithelial neoplasia (mPanIN) by acinar cell targeting of oncogenic Kras in adult mice. Proc Natl Acad Sci U S A 2008;105:18913-8.
55. Erkan M, Reiser-Erkan C, Michalski CW, et al. Tumor microenvironment and progression of pancreatic cancer. Exp Oncol 2010;32:128-31.

56. Nitsche C, Simon P, Weiss FU, et al. Environmental risk factors for chronic pancreatitis and pancreatic cancer. Dig Dis 2011;29:235-42.
57. Malka D, Hammel P, Maire F, et al. Risk of pancreatic adenocarcinoma in chronic pancreatitis. Gut 2002;51:849-52.
58. Erez N, Truitt M, Olson P, et al. Cancer-Associated Fibroblasts Are Activated in Incipient Neoplasia to Orchestrate Tumor-Promoting Inflammation in an NF-kappaB-Dependent Manner. Cancer Cell 2010;17:135-47.
59. Didsbury J, Weber RF, Bokoch GM, et al. rac, a novel ras-related family of proteins that are botulinum toxin substrates. J Biol Chem 1989;264:16378-82.
60. Jaffe AB, Hall A. Rho GTPases: biochemistry and biology. Annu Rev Cell Dev Biol 2005;21:247-69.
61. Heasman SJ, Ridley AJ. Mammalian Rho GTPases: new insights into their functions from in vivo studies. Nat Rev Mol Cell Biol 2008;9:690-701.
62. Ridley AJ, Schwartz MA, Burridge K, et al. Cell migration: integrating signals from front to back. Science 2003;302:1704-9.
63. Cancelas JA, Lee AW, Prabhakar R, et al. Rac GTPases differentially integrate signals regulating hematopoietic stem cell localization. Nat Med 2005;11:886-91.
64. Gu Y, Filippi MD, Cancelas JA, et al. Hematopoietic cell regulation by Rac1 and Rac2 guanosine triphosphatases. Science 2003;302:445-9.
65. Qualmann B, Mellor H. Regulation of endocytic traffic by Rho GTPases. Biochem J 2003;371:233-41.
66. Williams JA, Chen X, Sabbatini ME. Small G proteins as key regulators of pancreatic digestive enzyme secretion. Am J Physiol Endocrinol Metab 2009;296:E405-14.
67. Bi Y, Page SL, Williams JA. Rho and Rac promote acinar morphological changes, actin reorganization, and amylase secretion. Am J Physiol Gastrointest Liver Physiol 2005;289:G561-70.
68. Greiner TU, Kesavan G, Stahlberg A, et al. Rac1 regulates pancreatic islet morphogenesis. BMC Dev Biol 2009;9:2.
69. Ellenbroek SI, Collard JG. Rho GTPases: functions and association with cancer. Clin Exp Metastasis 2007;24:657-72.
70. Hruban RH, Maitra A, Schulick R, et al. Emerging molecular biology of pancreatic cancer. Gastrointest Cancer Res 2008;2:S10-5.
71. Raptis L, Arulanandam R, Geletu M, et al. The R(h)oads to Stat3: Stat3 activation by the Rho GTPases. Exp Cell Res 2011;317:1787-95.
72. Yuan K, Qian C, Zheng R. Prognostic significance of immunohistochemical Rac1 expression in survival in early operable non-small cell lung cancer. Med Sci Monit 2009;15:BR313-9.
73. Karlsson R, Pedersen ED, Wang Z, et al. Rho GTPase function in tumorigenesis. Biochim Biophys Acta 2009;1796:91-8.
74. Kamai T, Shirataki H, Nakanishi K, et al. Increased Rac1 activity and Pak1 overexpression are associated with lymphovascular invasion and lymph node metastasis of upper urinary tract cancer. BMC Cancer 2010;10:164.
75. Crnogorac-Jurcevic T, Efthimiou E, Capelli P, et al. Gene expression profiles of pancreatic cancer and stromal desmoplasia. Oncogene 2001;20:7437-46.
76. Espina C, Cespedes MV, Garcia-Cabezas MA, et al. A critical role for Rac1 in tumor progression of human colorectal adenocarcinoma cells. Am J Pathol 2008;172:156-66.
77. Ma Q, Cavallin LE, Yan B, et al. Antitumorigenesis of antioxidants in a transgenic Rac1 model of Kaposi's sarcoma. Proc Natl Acad Sci U S A 2009;106:8683-8.
78. Malliri A, van der Kammen RA, Clark K, et al. Mice deficient in the Rac activator Tiam1 are resistant to Ras-induced skin tumours. Nature 2002;417:867-71.
79. Wang Z, Pedersen E, Basse A, et al. Rac1 is crucial for Ras-dependent skin tumor formation by controlling Pak1-Mek-Erk hyperactivation and hyperproliferation in vivo. Oncogene 2010;29:3362-73.
80. Kissil JL, Walmsley MJ, Hanlon L, et al. Requirement for Rac1 in a K-ras induced lung cancer in the mouse. Cancer Res 2007;67:8089-94.
81. Dokmanovic M, Hirsch DS, Shen Y, et al. Rac1 contributes to trastuzumab resistance of breast cancer cells: Rac1 as a potential therapeutic target for the treatment of trastuzumab-resistant breast cancer. Mol Cancer Ther 2009;8:1557-69.
82. Schnelzer A, Prechtel D, Knaus U, et al. Rac1 in human breast cancer: overexpression, mutation analysis, and characterization of a new isoform, Rac1b. Oncogene 2000;19:3013-20.
83. Bouzahzah B, Albanese C, Ahmed F, et al. Rho family GTPases regulate mammary epithelium cell growth and metastasis through distinguishable pathways. Mol Med 2001;7:816-30.
84. Olson MF, Ashworth A, Hall A. An essential role for Rho, Rac, and Cdc42 GTPases in cell cycle progression through G1. Science 1995;269:1270-2.

85. Chiariello M, Marinissen MJ, Gutkind JS. Regulation of c-myc expression by PDGF through Rho GTPases. Nat Cell Biol 2001;3:580-6.
86. Qiu RG, Chen J, Kirn D, et al. An essential role for Rac in Ras transformation. Nature 1995;374:457-9.
87. Quinlan MP. Suppression of epithelial cell transformation and induction of actin dependent differentiation by dominant negative Rac1, but not Ras, Rho or Cdc42. Cancer Biol Ther 2004;3:65-70.
88. Vivanco I, Sawyers CL. The phosphatidylinositol 3-Kinase AKT pathway in human cancer. Nat Rev Cancer 2002;2:489-501.
89. Zhou K, Wang Y, Gorski JL, et al. Guanine nucleotide exchange factors regulate specificity of downstream signaling from Rac and Cdc42. J Biol Chem 1998;273:16782-6.
90. Bauer B, Mirey G, Vetter IR, et al. Effector recognition by the small GTP-binding proteins Ras and Ral. J Biol Chem 1999;274:17763-70.
91. Matos P, Jordan P. Rac1, but not Rac1B, stimulates RelB-mediated gene transcription in colorectal cancer cells. J Biol Chem 2006;281:13724-32.
92. Matos P, Jordan P. Expression of Rac1b stimulates NF-kappaB-mediated cell survival and G1/S progression. Exp Cell Res 2005;305:292-9.
93. Fernandez-Zapico ME, Gonzalez-Paz NC, Weiss E, et al. Ectopic expression of VAV1 reveals an unexpected role in pancreatic cancer tumorigenesis. Cancer Cell 2005;7:39-49.
94. Williams LM, Lali F, Willetts K, et al. Rac mediates TNF-induced cytokine production via modulation of NF-kappaB. Mol Immunol 2008;45:2446-54.
95. Fukuda A, Wang SC, Morris JPt, et al. Stat3 and MMP7 contribute to pancreatic ductal adenocarcinoma initiation and progression. Cancer Cell 2011;19:441-55.
96. Lesina M, Kurkowski MU, Ludes K, et al. Stat3/Socs3 activation by IL-6 transsignaling promotes progression of pancreatic intraepithelial neoplasia and development of pancreatic cancer. Cancer Cell 2011;19:456-69.
97. Masui T, Hosotani R, Doi R, et al. Expression of IL-6 receptor in pancreatic cancer: involvement in VEGF induction. Anticancer Res 2002;22:4093-100.
98. Thiery JP, Sleeman JP. Complex networks orchestrate epithelial-mesenchymal transitions. Nat Rev Mol Cell Biol 2006;7:131-42.
99. Arulanandam R, Geletu M, Feracci H, et al. Activated Rac1 requires gp130 for Stat3 activation, cell proliferation and migration. Exp Cell Res 2010;316:875-86.
100. Arulanandam R, Vultur A, Cao J, et al. Cadherin-cadherin engagement promotes cell survival via Rac1/Cdc42 and signal transducer and activator of transcription-3. Mol Cancer Res 2009;7:1310-27.
101. Teng TS, Lin B, Manser E, et al. Stat3 promotes directional cell migration by regulating Rac1 activity via its activator betaPIX. J Cell Sci 2009;122:4150-9.
102. Singh A, Karnoub AE, Palmby TR, et al. Rac1b, a tumor associated, constitutively active Rac1 splice variant, promotes cellular transformation. Oncogene 2004;23:9369-80.
103. Binker MG, Binker-Cosen AA, Richards D, et al. EGF promotes invasion by PANC-1 cells through Rac1/ROS-dependent secretion and activation of MMP-2. Biochem Biophys Res Commun 2009;379:445-50.
104. Gao Y, Dickerson JB, Guo F, et al. Rational design and characterization of a Rac GTPase-specific small molecule inhibitor. Proc Natl Acad Sci U S A 2004;101:7618-23.
105. Yoshida T, Zhang Y, Rivera Rosado LA, et al. Blockade of Rac1 activity induces G1 cell cycle arrest or apoptosis in breast cancer cells through downregulation of cyclin D1, survivin, and X-linked inhibitor of apoptosis protein. Mol Cancer Ther 2010;9:1657-68.
106. Binker MG, Binker-Cosen AA, Gaisano HY, et al. Inhibition of Rac1 decreases the severity of pancreatitis and pancreatitis-associated lung injury in mice. Exp Physiol 2008;93:1091-103.
107. Muller LU, Schore RJ, Zheng Y, et al. Rac guanosine triphosphatases represent a potential target in AML. Leukemia 2008;22:1803-6.
108. Thomas EK, Cancelas JA, Chae HD, et al. Rac guanosine triphosphatases represent integrating molecular therapeutic targets for BCR-ABL-induced myeloproliferative disease. Cancer Cell 2007;12:467-78.
109. Rozenveld-Geugien M, Baas IO, van Gosliga D, et al. Expansion of normal and leukemic human hematopoietic stem/progenitor cells requires rac-mediated interaction with stromal cells. Exp Hematol 2007;35:782-92.
110. Shutes A, Onesto C, Picard V, et al. Specificity and mechanism of action of EHT 1864, a novel small molecule inhibitor of Rac family small GTPases. J Biol Chem 2007;282:35666-78.
111. Bhanot H, Young AM, Overmeyer JH, et al. Induction of nonapoptotic cell death by activated Ras requires inverse regulation of Rac1 and Arf6. Mol Cancer Res 2010;8:1358-74.

112. Desire L, Bourdin J, Loiseau N, et al. RAC1 inhibition targets amyloid precursor protein processing by gamma-secretase and decreases Abeta production in vitro and in vivo. J Biol Chem 2005;280:37516-25.
113. Greenhalf W, Neoptolemos JP. Increasing survival rates of patients with pancreatic cancer by earlier identification. Nat Clin Pract Oncol 2006;3:346-7.
114. Brunner TB, Scott-Brown M. The role of radiotherapy in multimodal treatment of pancreatic carcinoma. Radiat Oncol 2010;5:64.
115. McNulty NJ, Francis IR, Platt JF, et al. Multi--detector row helical CT of the pancreas: effect of contrast-enhanced multiphasic imaging on enhancement of the pancreas, peripancreatic vasculature, and pancreatic adenocarcinoma. Radiology 2001;220:97-102.
116. Dewitt J, Devereaux BM, Lehman GA, et al. Comparison of endoscopic ultrasound and computed tomography for the preoperative evaluation of pancreatic cancer: a systematic review. Clin Gastroenterol Hepatol 2006;4:717-25; quiz 664.
117. Bali MA, Metens T, Denolin V, et al. Tumoral and Nontumoral Pancreas: Correlation between Quantitative Dynamic Contrast-enhanced MR Imaging and Histopathologic Parameters. Radiology 2011;261:456-66.
118. Matos C, Cappeliez O, Winant C, et al. MR imaging of the pancreas: a pictorial tour. Radiographics 2002;22:e2.
119. Balci NC, Perman WH, Saglam S, et al. Diffusion-weighted magnetic resonance imaging of the pancreas. Top Magn Reson Imaging 2009;20:43-7.
120. Kitano M, Sakamoto H, Komaki T, et al. New techniques and future perspective of EUS for the differential diagnosis of pancreatic malignancies: contrast harmonic imaging. Dig Endosc 2011;23 Suppl 1:46-50.
121. Nguyen VX, Nguyen CC, Nguyen BD. (1)F-FDG PET/CT imaging of the pancreas: spectrum of diseases. Jop 2011;12:557-66.
122. de Jong K, Bruno MJ, Fockens P. Epidemiology, diagnosis, and management of cystic lesions of the pancreas. Gastroenterol Res Pract 2012;2012:147465.
123. Barwick T, Bencherif B, Mountz JM, et al. Molecular PET and PET/CT imaging of tumour cell proliferation using F-18 fluoro-L-thymidine: a comprehensive evaluation. Nucl Med Commun 2009;30:908-17.
124. Serrano OK, Chaudhry MA, Leach SD. The role of PET scanning in pancreatic cancer. Adv Surg 2010;44:313-25.
125. Herrmann K, Eckel F, Schmidt S, et al. In vivo characterization of proliferation for discriminating cancer from pancreatic pseudotumors. J Nucl Med 2008;49:1437-44.
126. Lin JL, Barthel JS, Keshishian J, et al. Negative predictive value of positron emission tomography/computed tomography in patients with a clinical suspicion of pancreatic cancer. Pancreas 2011;40:653-6.
127. Van Laethem JL, Verslype C, Iovanna JL, et al. New strategies and designs in pancreatic cancer research: consensus guidelines report from a European expert panel. Ann Oncol 2012;23:570-6.
128. Pierantoni C, Pagliacci A, Scartozzi M, et al. Pancreatic cancer: progress in cancer therapy. Crit Rev Oncol Hematol 2008;67:27-38.
129. Palta M, Willett C, Czito B. Role of radiation therapy in patients with resectable pancreatic cancer. Oncology (Williston Park) 2011;25:715-21, 727.
130. Oettle H, Post S, Neuhaus P, et al. Adjuvant chemotherapy with Gemcitabine vs observation in patients undergoing curative-intent resection of pancreatic cancer: a randomized controlled trial. Jama 2007;297:267-77.
131. Trouilloud I, Dubreuil O, Boussaha T, et al. Medical treatment of pancreatic cancer: new hopes after 10 years of Gemcitabine. Clin Res Hepatol Gastroenterol 2011;35:364-74.
132. Conroy T, Gavoille C, Adenis A. Metastatic pancreatic cancer: old drugs, new paradigms. Curr Opin Oncol 2011;23:390-5.
133. Burris HA, 3rd, Moore MJ, Andersen J, et al. Improvements in survival and clinical benefit with Gemcitabine as first-line therapy for patients with advanced pancreas cancer: a randomized trial. J Clin Oncol 1997;15:2403-13.
134. Burris H, Storniolo AM. Assessing clinical benefit in the treatment of pancreas cancer: Gemcitabine compared to 5-fluorouracil. Eur J Cancer 1997;33 Suppl 1:S18-22.
135. Longo R, Cacciamani F, Naso G, et al. Pancreatic cancer: from molecular signature to target therapy. Crit Rev Oncol Hematol 2008;68:197-211.
136. Moore MJ. The treatment of advanced pancreatic cancer: current evidence and future challenges. Ann Oncol 2008;19 Suppl 7:vii304-8.
137. Conroy T, Desseigne F, Ychou M, et al. FOLFIRINOX versus Gemcitabine for metastatic pancreatic cancer. N Engl J Med 2011;364:1817-25.

138. Garrido-Laguna I, Uson M, Rajeshkumar NV, et al. Tumor engraftment in nude mice and enrichment in stroma- related gene pathways predict poor survival and resistance to Gemcitabine in patients with pancreatic cancer. Clin Cancer Res 2011;17:5793-800.
139. Hidalgo M. Pancreatic cancer. N Engl J Med 2010;362:1605-17.
140. Hidalgo M, Bruckheimer E, Rajeshkumar NV, et al. A pilot clinical study of treatment guided by personalized tumorgrafts in patients with advanced cancer. Mol Cancer Ther 2011;10:1311-6.
141. Plentz R, Park JS, Rhim AD, et al. Inhibition of gamma-secretase activity inhibits tumor progression in a mouse model of pancreatic ductal adenocarcinoma. Gastroenterology 2009;136:1741-9 e6.
142. Abasolo I, Pujal J, Rabanal RM, et al. FDG PET imaging of Ela1-myc mice reveals major biological differences between pancreatic acinar and ductal tumours. Eur J Nucl Med Mol Imaging 2009;36:1156-66.
143. Fendrich V, Schneider R, Maitra A, et al. Detection of precursor lesions of pancreatic adenocarcinoma in PET-CT in a genetically engineered mouse model of pancreatic cancer. Neoplasia 2011;13:180-6.
144. Eser S, Messer M, Eser P, et al. In vivo diagnosis of murine pancreatic intraepithelial neoplasia and early-stage pancreatic cancer by molecular imaging. Proc Natl Acad Sci U S A 2011;108:9945-50.
145. Mohammed A, Janakiram NB, Li Q, et al. The epidermal growth factor receptor inhibitor gefitinib prevents the progression of pancreatic lesions to carcinoma in a conditional LSL-KrasG12D/+ transgenic mouse model. Cancer Prev Res (Phila) 2010;3:1417-26.
146. Logsdon CD, Abbruzzese JL. Chemoprevention of pancreatic cancer: ready for the clinic? Cancer Prev Res (Phila) 2010;3:1375-8.
147. Glogauer M, Marchal CC, Zhu F, et al. Rac1 deletion in mouse neutrophils has selective effects on neutrophil functions. J Immunol 2003;170:5652-7.
148. Soriano P. Generalized lacZ expression with the ROSA26 Cre reporter strain. Nat Genet 1999;21:70-1.
149. Steingoetter A, Svensson J, Kosanke Y, et al. Reference region-based pharmacokinetic modeling in quantitative dynamic contract-enhanced MRI allows robust treatment monitoring in a rat liver tumor model despite cardiovascular changes. Magn Reson Med 2011;65:229-38.
150. Winkelmann S, Schaeffter T, Koehler T, et al. An optimal radial profile order based on the Golden Ratio for time-resolved MRI. IEEE Trans Med Imaging 2007;26:68-76.
151. Schreiber FS, Deramaudt TB, Brunner TB, et al. Successful growth and characterization of mouse pancreatic ductal cells: functional properties of the Ki-RAS(G12V) oncogene. Gastroenterology 2004;127:250-60.
152. Heid I, Lubeseder-Martellato C, Sipos B, et al. Early requirement of Rac1 in a mouse model of pancreatic cancer. Gastroenterology 2011;141:719-30, 730 e1-7.
153. Sphyris N, Logsdon CD, Harrison DJ. Improved retention of zymogen granules in cultured murine pancreatic acinar cells and induction of acinar-ductal transdifferentiation in vitro. Pancreas 2005;30:148-57.
154. Kelsen DP, Portenoy RK, Thaler HT, et al. Pain and depression in patients with newly diagnosed pancreas cancer. J Clin Oncol 1995;13:748-55.
155. Kowluru A. Friendly, and not so friendly, roles of Rac1 in islet beta-cell function: lessons learnt from pharmacological and molecular biological approaches. Biochem Pharmacol 2011;81:965-75.
156. Torgerson RR, McNiven MA. Agonist-induced changes in cell shape during regulated secretion in rat pancreatic acini. J Cell Physiol 2000;182:438-47.
157. Erkan M, Hausmann S, Michalski CW, et al. The role of stroma in pancreatic cancer: diagnostic and therapeutic implications. Nat Rev Gastroenterol Hepatol 2012;9:454-67.
158. Kalluri R, Zeisberg M. Fibroblasts in cancer. Nat Rev Cancer 2006;6:392-401.
159. Choi SS, Witek RP, Yang L, et al. Activation of Rac1 promotes hedgehog-mediated acquisition of the myofibroblastic phenotype in rat and human hepatic stellate cells. Hepatology 2010;52:278-90.
160. Mantovani A. Molecular pathways linking inflammation and cancer. Curr Mol Med 2010;10:369-73.
161. Gastonguay A, Berg T, Hauser AD, et al. The role of Rac1 in the regulation of NF-kappaB activity, cell proliferation, and cell migration in non-small cell lung carcinoma. Cancer Biol Ther 2012;13:647-56.
162. Treiber M, Neuhofer P, Anetsberger E, et al. Myeloid, but not pancreatic, RelA/p65 is required for fibrosis in a mouse model of chronic pancreatitis. Gastroenterology 2011;141:1473-85, 1485 e1-7.
163. Neuhofer P, Liang S, Einwachter H, et al. Deletion of IkappaBalpha Activates RelA to Reduce Acute Pancreatitis in Mice through Upregulation of Spi2A. Gastroenterology 2012.
164. Jacobetz MA, Chan DS, Neesse A, et al. Hyaluronan impairs vascular function and drug delivery in a mouse model of pancreatic cancer. Gut 2012.
165. Provenzano PP, Cuevas C, Chang AE, et al. Enzymatic targeting of the stroma ablates physical barriers to treatment of pancreatic ductal adenocarcinoma. Cancer Cell 2012;21:418-29.

166. Kawarazaki W, Nagase M, Yoshida S, et al. Angiotensin II- and salt-induced kidney injury through Rac1-mediated mineralocorticoid receptor activation. J Am Soc Nephrol 2012;23:997-1007.
167. Johnson JI, Decker S, Zaharevitz D, et al. Relationships between drug activity in NCI preclinical in vitro and in vivo models and early clinical trials. Br J Cancer 2001;84:1424-31.
168. Roberts TG, Jr., Goulart BH, Squitieri L, et al. Trends in the risks and benefits to patients with cancer participating in phase 1 clinical trials. Jama 2004;292:2130-40.
169. Cook N, Jodrell DI, Tuveson DA. Predictive in vivo animal models and translation to clinical trials. Drug Discov Today 2012;17:253-60.
170. Perez-Mancera PA, Guerra C, Barbacid M, et al. What we have learned about pancreatic cancer from mouse models. Gastroenterology 2012;142:1079-92.
171. Olson P, Chu GC, Perry SR, et al. Imaging guided trials of the angiogenesis inhibitor sunitinib in mouse models predict efficacy in pancreatic neuroendocrine but not ductal carcinoma. Proc Natl Acad Sci U S A 2011;108:E1275-84.
172. Ardito CM, Gruner BM, Takeuchi KK, et al. EGF Receptor Is Required for KRAS-Induced Pancreatic Tumorigenesis. Cancer Cell 2012;22:304-17.
173. Olson ES, Whitney MA, Friedman B, et al. In vivo fluorescence imaging of atherosclerotic plaques with activatable cell-penetrating peptides targeting thrombin activity. Integr Biol (Camb) 2012;4:595-605.
174. Partecke IL, Kaeding A, Sendler M, et al. In vivo imaging of pancreatic tumours and liver metastases using 7 Tesla MRI in a murine orthotopic pancreatic cancer model and a liver metastases model. BMC Cancer 2011;11:40.
175. Collins MA, Bednar F, Zhang Y, et al. Oncogenic Kras is required for both the initiation and maintenance of pancreatic cancer in mice. J Clin Invest 2012;122:639-53.
176. Braren R, Altomonte J, Settles M, et al. Validation of preclinical multiparametric imaging for prediction of necrosis in hepatocellular carcinoma after embolization. J Hepatol 2011;55:1034-40.
177. Chen F, De Keyzer F, Wang H, et al. Diffusion weighted imaging in small rodents using clinical MRI scanners. Methods 2007;43:12-20.
178. Samkoe KS, Chen A, Rizvi I, et al. Imaging tumor variation in response to photodynamic therapy in pancreatic cancer xenograft models. Int J Radiat Oncol Biol Phys 2010;76:251-9.
179. Willmann JK, van Bruggen N, Dinkelborg LM, et al. Molecular imaging in drug development. Nat Rev Drug Discov 2008;7:591-607.
180. Grunberg K, Grenacher L, Klauss M. [Diffusion-weighted imaging of the pancreas]. Radiologe 2011;51:186-94.
181. Ichikawa T, Erturk SM, Motosugi U, et al. High-b value diffusion-weighted MRI for detecting pancreatic adenocarcinoma: preliminary results. AJR Am J Roentgenol 2007;188:409-14.
182. Kartalis N, Lindholm TL, Aspelin P, et al. Diffusion-weighted magnetic resonance imaging of pancreas tumours. Eur Radiol 2009;19:1981-90.
183. Muraoka N, Uematsu H, Kimura H, et al. Apparent diffusion coefficient in pancreatic cancer: characterization and histopathological correlations. J Magn Reson Imaging 2008;27:1302-8.
184. Takeuchi M, Matsuzaki K, Kubo H, et al. High-b-value diffusion-weighted magnetic resonance imaging of pancreatic cancer and mass-forming chronic pancreatitis: preliminary results. Acta Radiol 2008;49:383-6.
185. Lewandowski RJ, Eifler AC, Bentrem DJ, et al. Functional magnetic resonance imaging in an animal model of pancreatic cancer. World J Gastroenterol 2010;16:3292-8.
186. Kim H, Morgan DE, Buchsbaum DJ, et al. Early therapy evaluation of combined anti-death receptor 5 antibody and Gemcitabine in orthotopic pancreatic tumor xenografts by diffusion-weighted magnetic resonance imaging. Cancer Res 2008;68:8369-76.
187. Aref M, Chaudhari AR, Bailey KL, et al. Comparison of tumor histology to dynamic contrast enhanced magnetic resonance imaging-based physiological estimates. Magn Reson Imaging 2008;26:1279-93.
188. Hermann J, Fry A, Reising M, et al. Rabies vaccine standards: Comparison of the 5th and 6th WHO international reference standards to the USDA veterinary reference standard. Vaccine 2012.
189. Buck AC, Schirrmeister HH, Guhlmann CA, et al. Ki-67 immunostaining in pancreatic cancer and chronic active pancreatitis: does in vivo FDG uptake correlate with proliferative activity? J Nucl Med 2001;42:721-5.
190. Rasey JS, Grierson JR, Wiens LW, et al. Validation of FLT uptake as a measure of thymidine kinase-1 activity in A549 carcinoma cells. J Nucl Med 2002;43:1210-7.
191. Husband JE, Schwartz LH, Spencer J, et al. Evaluation of the response to treatment of solid tumours - a consensus statement of the International Cancer Imaging Society. Br J Cancer 2004;90:2256-60.
192. Tomasi G, Rosso L. PET imaging: implications for the future of therapy monitoring with PET/CT in oncology. Curr Opin Pharmacol 2012.

193. Tomasi G, Turkheimer F, Aboagye E. Importance of quantification for the analysis of PET data in oncology: review of current methods and trends for the future. Mol Imaging Biol 2012;14:131-46.
194. Li SP, Padhani AR. Tumor response assessments with diffusion and perfusion MRI. J Magn Reson Imaging 2012;35:745-63.
195. Akisik MF, Sandrasegaran K, Bu G, et al. Pancreatic cancer: utility of dynamic contrast-enhanced MR imaging in assessment of antiangiogenic therapy. Radiology 2010;256:441-9.
196. Casneuf VF, Delrue L, Van Damme N, et al. Noninvasive monitoring of therapy-induced microvascular changes in a pancreatic cancer model using dynamic contrast-enhanced magnetic resonance imaging with P846, a new low-diffusible gadolinium-based contrast agent. Radiat Res 2011;175:10-20.
197. Koh DM, Scurr E, Collins D, et al. Predicting response of colorectal hepatic metastasis: value of pretreatment apparent diffusion coefficients. AJR Am J Roentgenol 2007;188:1001-8.

6. Acknowledgements

I would like to express my greatest gratitude to the following people who have helped and supported me throughout my project:

My doctorate supervisor **Prof. Dr. Michael Schemann** and co-supervisor **Prof. Dr. Roland M. Schmid** for taking me on as a PhD student in the beginning and supporting me through the studies.

My co-supervisor and my **main scientific advisor PD Dr. Jens T. Siveke**, for your immense knowledge of the scientific field, your generosity and positive attitude towards me. I have particularly cherished your independent and free way of work, your trust in my abilities and your opened ear for new suggestions. I am grateful for letting me be a part of your team, your wisdom, and patience and for your never exceeding encouragement.

A very special thanks of mine goes to my current supervisor **Dr. Rickmer Braren** and my dearest co-worker **Dr. Marija Trajkovic-Arsic**. Particularly over the last two years, closely working on that very hard project, you have been truly inspiring, always been there and enormously encouraging at any time. Your trust, your help and our scientific discussions deeply moved me and allowed to make gigantic scientific and personal progress.

My former co-worker **Dr. Pawel Mazur** and **Dr. Hassan Nakhai** for your vast enthusiasm on science, support and practical guidance in the early time of my study. Without you this thesis might not be written. I really miss our late evening talks and debates that helped me to gain the necessary confidence and critical attitude.

Graduiertenzentrum Weihenstephan und die TUM Graduate School and the coordination office for taking chances on me and for continuous support and great opportunities you gave me over the years.

Whole Siveke's lab: **Barbara, Clara, Marcel, Roxanne, Vicky, Nicole, Alex, Florian and Mathilde**, all of you for your sunny spirit and for never exhausting will to help out. Thanks for all the good times!

Whole Braren's lab and Department of Radiology: **Manuela, Yvonne, Iryna, Marcus, David, Claudia and Prof. Dr. Ernst J. Rummeny**, for their help, support and know how.

I am particularly grateful for the assistance provided by **Juliane and Tamara** in the dark night hours on the scanner.

All my friends: **Petra, Franziska, Daniela, Eva, Veronika und Angela**, you moral support has been invaluable. Thank you for always believing in me!

My family: Mama, Papa and Tatjana, you give me strength and motivation. I am truly grateful for your immense support and never-ending love.

Alexej, my husband, my friend and my bastion of calm!

Appendix 1: List of abbreviations

[^{18}F]-FDG	2-[^{18}F]-fluoro-2-deoxy-D-glucose
[^{18}F]-FLT	[^{18}F]-fluoro-3'-deoxy-3'-L-fluorothymidine
ACC	acinar cell carcinomas
ADC	apparent diffusion coefficient
ADM	acino-ductal metaplasia
BRCA2	Breast Cancer 2, early-onset
CAFs	cancer associated activated fibroblasts
CCK	cholecytokinin
CK19	cytokeratine 19
CT	computed tomography
DCE-MRI	dynamic contrast enhanced MRI
DMBA	7,12-Dimethylbenz(a)anthracene
DW-MRI	diffusion-weighted MRI
EGF	epidermal growth factor
EGFR	epidermal growth factor receptor
EMT	epithelial to mesenchymal transition
ERCP	endoscopic retrograde cholangio pancreatography
EUS	endoscopic ultrasound
FNA	fine needle aspiration
GAPs	GTPase-activating proteins
Gd-DTPA	Gadulinium-DTPA
GDIs	guanine nucleotide dissociation inhibitors
GEFs	guanine nucleotide exchange factors
GEMM	genetically engineered mouse models
GPCR	G-coupled protein receptors
GTT	glucose tolerance test
H&E	hematoxylin and eosin stain
i.p.	intraperitonealy
iAUC90rel	relative area under the curve
IL-6	interleukin-6
IPMN	intraductal papillary mucinous neoplasm
m	murine
MCN	mucinous cystic neoplasm
MMP	matrix metalloprotease
MRCP	magnetic resonance cholangio pancreatography

MRI	magnetic resonance Imaging
MTT	tetrazolium salt
Nf-kB	nuclear factor-kappa B
Pak1	serine/threonine-protein kinase PAK 1
PanIN	pancreatic intraepithelial neoplasia
PDAC	pancreatic ductal adenocarcimoma
Pdx1	pancreatic duodenum homeobox 1
PET	postiton emission tomography
PI3K	phosphoinositide 3-kinase
PP-cells	pancreatic polypeptide-producing cells
Ptf1a	pancreas transcription factor 1 subunit alpha
Rac1	RAS-related C3 botulinum substrate 1
ROS	reactive oxygen species
s.c.	subcutaneously
SAST-3	signal transducer and activator of transcription 3
T	Tesla
T/M	tumor-to-muscle ratio
T_2w	T_2-weighted
TF	transcription factor
TP53	tumor suppressor protein 53
US	ultrasound

Appendix 2: List of tables and figures

A2.1: Tables.

A2.2: Figures.